

POLITECNICO DI TORINO

---

Master Degree Course in Aerospace Engineering

Master Degree Thesis

**Validation of a Numerical Procedure  
to Extract the Aerodynamic  
Derivatives of Re-entry Vehicles**



**Supervisor**  
prof. Domenic D'Ambrosio

**Candidate**  
Roberto D'Angelo

**Internship Tutor**  
ing. Cosimo Chiarelli  
ing. Vincenzo Mareschi

---

Marzo 2019



# Sommario

Sin dai primi voli spaziali fu chiaro che la fase di rientro richieda particolari attenzioni al fine di assicurare sia l'incolumità del personale di bordo che l'integrità di strumentazione e campioni.

In questo lavoro viene analizzato uno dei fattori critici di questa fase molto complessa: la stabilità aerodinamica. Nello specifico, avvalendosi della tecnica numerica, si è validata una procedura in grado di estrapolare le derivate aerodinamiche che qualificano la stabilità aerodinamica di un velivolo spaziale in fase di rientro.

Per estrarre le derivate aerodinamiche di interesse è stato utilizzato il metodo delle oscillazioni forzate. Si è imposto una determinata legge oscillatoria al dominio di calcolo comprendente il corpo in esame e mantenuto fisso il vettore velocità della corrente indisturbata. Da ciò consegue un'alterazione temporale dell'angolo di attacco e dei coefficienti aerodinamici. Tenendo traccia della variazione di questi coefficienti, a posteriori, si sono estratti i parametri di interesse.

Per lo studio ci si è avvalsi di due codici CFD commerciali: Ansys Fluent e Metacomp CFD++. Una casistica semplice è stata inizialmente oggetto di studio, andando ad analizzare il comportamento della capsula di rientro Hayabusa in condizioni di volo subsonico. Ottenuti i primi risultati, lo studio è stato condotto sul velivolo Space Rider.

I risultati numerici confermano la bontà dell'approccio scelto e identificano in CFD++ il codice numerico più performante per questo tipo di simulazione.



# Summary

Since the first space flights it was clear that the re-entry phase requires particular attention in order to ensure both the safety of the personnel on board and the integrity of instrumentation and samples.

In this paper, one of the critical factors of this very complex phase is analysed: aerodynamic stability. Specifically, using the numerical technique, it was possible to validate a procedure that can extrapolate the aerodynamic derivatives which qualify the aerodynamic stability of a spacecraft during re-entry phase.

The forced oscillations method was used to extract the aerodynamic derivatives of interest. A certain oscillatory law has been imposed on the computational domain which includes the body in question, while the velocity vector of the undisturbed flow is kept fixed. This led to a temporal alteration of the angle of attack and of the aerodynamic coefficients. Keeping track about the variation of these coefficients the parameters of interest were extracted a posteriori.

This study was carried out using two commercial CFD codes: Ansys Fluent and Metacomp CFD++. A simple case was initially studied, analysing the behaviour of the Hayabusa return capsule in subsonic flight conditions. After first results had been achieved, the study was conducted on the Space Rider vehicle.

Numerical results confirm the accuracy of the chosen approach and identify CFD++ as the most performing numerical code for this type of simulation.



# Contents

List of Figures	IX
List of Tables	XIII
Nomenclature	XV
<b>1 Introduction</b>	<b>1</b>
1.1 Re-entry from Orbit	1
1.2 Re-entry Vehicle Design	3
1.3 Ballistic and Lifting Re-Entry	4
1.4 Instability for Blunt-Body Shape	5
1.4.1 Physics of the phenomenon	6
1.5 Numerical investigation	8
1.6 Scope and Overview of the present dissertation	9
<b>2 Mission analysis</b>	<b>11</b>
2.1 Musec-C Mission	11
2.1.1 Hayabusa Capsule	12
2.1.2 Reference System and CAD Model	13
2.1.3 Aerodynamic Database	14
2.2 Space Rider Program	16
2.2.1 Space Rider Vehicle	17
2.2.2 Reference System and CAD Model	19
2.2.3 Aerodynamic Database	20
<b>3 Background theory: aerodynamic stability</b>	<b>21</b>
3.1 Stability Derivatives	22
3.2 Stability and Stability Derivatives	23
3.3 Forced Oscillation Technique	25
<b>4 Numerical Techniques</b>	<b>29</b>
4.1 Arbitrary Lagrangian Eulerian Approach	29
4.2 Chimera Technique	32
4.2.1 Fluent: Overset Mesh	32
4.3 Numerical set-up	35
4.3.1 Boundary conditions	35

4.3.2	Gas Model . . . . .	35
4.3.3	Turbulence Models . . . . .	36
4.3.4	Resolution Scheme . . . . .	39
<b>5</b>	<b>Hayabusa: Numerical Analysis</b>	<b>41</b>
5.1	Pre-Processing . . . . .	41
5.1.1	Basic Assumptions . . . . .	41
5.1.2	Mesh Generation . . . . .	42
5.1.3	Mesh Convergence Study . . . . .	44
5.2	Numerical Set-up . . . . .	47
5.3	Fluent Simulations . . . . .	48
5.3.1	Steady State Tests . . . . .	48
5.3.2	Transient Tests . . . . .	48
5.3.3	Post-Processing . . . . .	52
5.4	CFD++ Simulations . . . . .	53
5.4.1	Steady State Tests . . . . .	53
5.4.2	Transient Tests . . . . .	54
5.4.3	Post-Processing . . . . .	55
5.5	Comparison . . . . .	56
<b>6</b>	<b>Space Rider: Numerical Simulations</b>	<b>59</b>
6.1	Pre-processing . . . . .	59
6.1.1	Basic Assumption . . . . .	59
6.1.2	Mesh Generation . . . . .	60
6.2	Numerical Set-Up . . . . .	62
6.3	Fluent Simulations . . . . .	63
6.3.1	Steady State Test . . . . .	65
6.3.2	Transient Tests with Time-step of 6e-3 s . . . . .	65
6.3.3	Transient Tests with Time-step of 1e-3 s . . . . .	66
6.3.4	Post-Processing . . . . .	67
6.4	CFD++ Simulations . . . . .	68
6.4.1	Steady State Test . . . . .	68
6.4.2	Transient Tests . . . . .	69
6.4.3	Post-Processing . . . . .	70
6.5	Comparison . . . . .	70
<b>7</b>	<b>Conclusions</b>	<b>75</b>
<b>A</b>	<b>CFD Figures</b>	<b>77</b>
	<b>Bibliography</b>	<b>87</b>

# List of Figures

1.1	Stagnation-point flow regimes for re-entry vehicle (Viviani and Pezzella 2015).	2
1.2	Influence of L/D for different configuration and landing region on Earth (Viviani and Pezzella 2015).	4
1.3	The effect of L/D on the reference heating-rate history (Viviani and Pezzella 2015).	5
1.4	Apollo and Huygens shape.	6
1.5	Pressure variation with pitching motion (Teramoto, Kouju Hiraki, and Fujii 2001).	7
1.6	Corresponding hysteresis in pitching moment (Teramoto, Kouju Hiraki, and Fujii 2001).	8
2.1	Hayabusa ( <i>Hayabusa: A technology Demonstrator 2005</i> ).	11
2.2	Hayabusa: sample collecting mechanism ( <i>Asteroid Explorer Hayabusa 2005</i> ).	12
2.3	Hayabusa reproduction (on the left) and size (on the right) (Ishii and Koju Hiraki 2003).	13
2.4	Technologies aboard the Hayabusa ( <i>Asteroid Explorer Hayabusa 2005</i> ).	13
2.5	Forces and moments convention.	14
2.6	Hayabusa: CAD model.	14
2.7	Axial force coefficient as function of Mach number and angle of attach (Ishii and Koju Hiraki 2003).	15
2.8	Normal force coefficient as function of Mach number and angle of attach (Ishii and Koju Hiraki 2003).	15
2.9	Pitching moment coefficient as function of Mach number and angle of attach (Ishii and Koju Hiraki 2003).	16
2.10	Dynamic damping coefficient as function of Mach number and angle of attach (Ishii and Koju Hiraki 2003).	16
2.11	Space Rider with service module.	17
2.12	Space-Rider concept of operations (Marini et al. 2017).	18
2.13	Aerodynamic convention (Marini et al. 2017).	19
2.14	Space Rider CAD model.	20
3.1	In order: stable, unstable and neutral equilibrium.	21
3.2	Dynamic behaviour: neutral, stable and unstable.	22
3.3	Velocity distribution along the chord due to a rotation around the pitch axis.	24
3.4	Velocity distribution along the chord due to a translation along the z-axis.	24

3.5	Angle of attack due to $\dot{z}$ velocity. . . . .	27
4.1	One-dimensional example of Lagrangian, Eulerian and ALE mesh and particle motion (Hirt, Amsden, and Cook 1974). . . . .	30
4.2	Lagrangian versus ALE descriptions: (a) initial FE mesh; (b) ALE mesh at $t = 1$ ms; (c) Lagrangian mesh at $t = 1$ ms; (d) details of interface in Lagrangian description (Hirt, Amsden, and Cook 1974). . . . .	31
4.3	Overset case set-up ( <i>Ansys Fluent User and Theory's Guide</i> 2018). . . . .	33
4.4	Overset mesh before and after hole cutting ( <i>Ansys Fluent User and Theory's Guide</i> 2018). . . . .	34
4.5	Figure shows the cylinder case after the overlap minimization step ( <i>Ansys Fluent User and Theory's Guide</i> 2018). . . . .	34
4.6	Flowchart illustrating solver algorithms (Franklyn 2008). . . . .	40
5.1	Size and shape of the fixed domain. . . . .	42
5.2	Size and shape of the moving domain. . . . .	43
5.3	View of the domain and capsule mesh. . . . .	43
5.4	On the left the cells affected by the overset are highlighted, while on the right we can see the region where the continuity residual is high. . . . .	44
5.5	On the left an image of the prism layers at the wall and on the right the values of $y^+$ on the capsule. . . . .	45
5.6	Graph of the residuals as a function of the number of iterations for each of the convergence tests. . . . .	46
5.7	Boundary groups. . . . .	47
5.8	Hayabusa: plunging oscillation, AoA= $0^\circ$ . . . . .	50
5.9	Hayabusa: pitching oscillation, AoA= $0^\circ$ . . . . .	50
5.10	Hayabusa: plunging oscillation, AoA= $10^\circ$ . . . . .	51
5.11	Hayabusa: pitching oscillation, AoA= $10^\circ$ . . . . .	51
5.12	Hayabusa: plunging oscillation, AoA= $20^\circ$ . . . . .	51
5.13	Hayabusa: pitching oscillation, AoA= $20^\circ$ . . . . .	52
5.14	Hayabusa: oscillation reconstruction, AoA= $0^\circ$ . . . . .	52
5.15	Hayabusa: oscillation reconstruction, AoA= $10^\circ$ . . . . .	53
5.16	Hayabusa: oscillation reconstruction, AoA= $20^\circ$ . . . . .	53
5.17	Hayabusa: plunging oscillation, AoA= $0^\circ$ . . . . .	54
5.18	Hayabusa: pitching oscillation, AoA= $10^\circ$ . . . . .	55
5.19	Hayabusa: oscillation reconstruction, AoA= $10^\circ$ . . . . .	55
5.20	Hayabusa: CFD++ results compared with Fluent results for plunging oscillation, AoA= $10^\circ$ . . . . .	57
5.21	Hayabusa: CFD++ results compared with Fluent results for pitching oscillation, AoA= $10^\circ$ . . . . .	57
6.1	Size and shape of the fixed domain. . . . .	60
6.2	Size and shape of the moving domain. . . . .	61
6.3	On the left an image of the prism layers at the wall and on the right the values of $y^+$ on the capsule. . . . .	61
6.4	View of the domain and Space Rider mesh. . . . .	62

6.5	On the left the cells affected by the overset are highlighted, while on the right we can see the region where the continuity residual is high. . . . .	62
6.6	Boundary groups. . . . .	63
6.7	Space Rider: plunging oscillation, AoA=65°. . . . .	66
6.8	Space Rider: pitching oscillation, AoA=65°. . . . .	66
6.9	Space Rider: plunging oscillation, AoA=65°. . . . .	67
6.10	Space Rider: pitching oscillation, AoA=65°. . . . .	67
6.11	Space Rider: oscillation reconstruction, AoA=65°. . . . .	68
6.12	Space Rider: plunging oscillation, AoA=65°. . . . .	69
6.13	Space Rider: pitching oscillation, AoA=65°. . . . .	69
6.14	Space Rider: oscillation reconstruction, AoA=65°. . . . .	70
6.15	Space Rider: Fluent results with time step=6·10 <sup>-3</sup> s compared with database results. . . . .	71
6.16	Space Rider: Fluent results with time step=6·10 <sup>-3</sup> s compared with database results. . . . .	71
6.17	Space Rider: Fluent results with time step=1·10 <sup>-3</sup> s compared with database curve. . . . .	72
6.18	Space Rider: Fluent results with time step=1·10 <sup>-3</sup> s and time step=6·10 <sup>-3</sup> s. . . . .	72
6.19	Space Rider: CFD++ results with Time Step=6·10 <sup>-3</sup> s compared with database. . . . .	73
6.20	Space Rider: CFD++ results with Time Step=6·10 <sup>-3</sup> s compared with database. . . . .	73
A.1	Hayabusa: steady state result at 10° of AoA. Stream-lines and Mach number contour. . . . .	77
A.2	Hayabusa: Mach number distribution in symmetry plane for 4 times-times over one period (Plunging motion) . . . . .	78
A.3	Hayabusa: pressure distribution in symmetry plane for 4 times-times over one period (Plunging motion) . . . . .	79
A.4	Hayabusa: Mach number distribution in symmetry plane for 4 times-times over one period (Pitching motion). . . . .	80
A.5	Hayabusa: pressure distribution in symmetry plane for 4 times-times over one period (Pitching motion) . . . . .	81
A.6	Space Rider: steady state result at 10° of AoA. Stream-lines and Mach number contour. . . . .	82
A.7	Space Rider: Mach number distribution in symmetry plane for 4 times-times over one period (Plunging motion) . . . . .	83
A.8	Space Rider: pressure distribution in symmetry plane for 4 times-times over one period (Plunging motion) . . . . .	84
A.9	Space Rider: Mach number distribution in symmetry plane for 4 times-times over one period (Pitching motion) . . . . .	85
A.10	Space Rider:pressure distribution in symmetry plane for 4 times-times over one period (Pitching motion) . . . . .	86



# List of Tables

2.1	Aerodynamic coefficients from database with uncertain values at $3\sigma$ . . . . .	20
2.2	Aerodynamic derivatives from database. . . . .	20
4.1	Summarizing table for each boundary type. . . . .	36
5.1	Results of the convergence test with various numbers of cells. . . . .	45
5.2	Parameters set for each boundary. . . . .	47
5.4	Fluent steady state tests results. . . . .	48
5.3	Models and algorithms set. . . . .	49
5.5	Motion and transient test parameters for Fluent simulation. . . . .	50
5.6	Hayabusa: aerodynamic derivatives from Fluent simulations. . . . .	52
5.7	CFD++ steady state test results. . . . .	54
5.8	Motion and transient test parameters. . . . .	54
5.9	Hayabusa: aerodynamic derivatives from CFD++ simulations. . . . .	55
5.10	Hayabusa: aerodynamic derivatives from CFD++ simulations. . . . .	58
6.1	Parameters set for each boundary. . . . .	63
6.2	Models and algorithms set. . . . .	64
6.3	Fluent steady state tests results. . . . .	65
6.4	Motion and transient test parameters. . . . .	65
6.5	Motion and transient test parameters. . . . .	66
6.6	Space Rider: aerodynamic derivatives from Fluent simulations. . . . .	67
6.7	CFD++ steady state test results. . . . .	68
6.8	Motion and transient test parameters. . . . .	69
6.9	Space Rider: aerodynamic derivatives from CFD++ simulations. . . . .	70



# Nomenclature

$\alpha$	Angle of attack
$\alpha_0$	Initial angle of attack
$\gamma$	Flight-path angle
$\lambda$	Free molecular path
$\omega$	Specific turbulence dissipation rate
$\omega$	Oscillation frequency
$\rho$	Density
$\rho_\infty$	Free-stream mass density
$\sigma$	Collision diameter
$\tau_{wall}$	Wall shear Stress
$\theta$	Pitch angle
$\varepsilon$	Turbulent dissipation rate
$A$	Sinusoid amplitude
$C_A$	Axial force coefficient
$C_D$	Drag coefficient
$C_f$	Skin friction coefficient
$C_L$	Lift coefficient
$C_l$	Roll moment coefficient
$C_m$	Pitching moment coefficient
$C_N$	Normal force coefficient
$C_n$	Yaw moment coefficient
$C_Y$	Side force coefficient

$C_{m\alpha}$	Slope of pitching moment respect to angle of attack
$C_{m\dot{\alpha}}$	Slope of pitching moment respect to angle of attack
$C_{m\dot{q}}$	Slope of pitching moment respect rate of change pitch of attack
$C_{mq}$	Slope of pitching moment respect rate of change pitch of attack
$C_{m_{1c}}$	Out-phase component
$C_{m_{1s}}$	In-phase component
$cg$	Center of gravity
$f$	Frequency
$k$	Turbulent kinetic energy
$K_n$	Knudsen number
$L_{ref}$	Reference length
$n$	Molecular number oer volume unit
$n_c$	Number of sinusoidal cycles
$q$	Time rate of change pitch of attack
$q_\infty$	Dynamic pressure
$Re$	Reynolds number
$S_{ref}$	Reference surface
$T$	Sinusoidal period
$t$	Time
$u_\tau$	Friction velocity
$V_\infty$	Freestream velocity
$y^+$	Dimensionless wall distance





# Chapter 1

## Introduction

In the second part of the twentieth century the ideological struggle between the United States and the Soviet Union gave impetus to spatial exploration in order to demonstrate their technological and intellectual superiority to the world. Today the Cold War is over but the space exploration continues and new countries have brought their flag into space in the name of research and progress.

Planetary exploration is focused on the analysis of the soil composition and the atmosphere of celestial bodies. This type of mission is performed by carrying out analyses in situ, using probes with appropriate instruments, or collecting samples and sending them to the Earth (sample return mission). Moreover, there are missions, such as the Apollo, in which men have set foot on the moon soil and return on Earth. The future space missions profile foresees also to bring a payload into orbit and conduct experiments in microgravity and return to Earth without human crew.

The common element of these missions is the atmospheric re-entry phase. This phase is the most dangerous one, in which a spacecraft enters from the outer space into a planet atmosphere. In Earth re-entry the initial phase is characterized by orbital velocities up to  $12 \text{ km/s}$  and the recorded flight Mach numbers can be as high as 30 and more. The dissipation of kinetic energy via interaction with the gaseous atmosphere is the only way to decelerate in order to allow safe landing without spending fuel. In fact the amount of rocket fuel required to slow the vehicle would be nearly equal to the amount used to accelerate it initially, so due to weight constrain the use of retro rockets is usually highly impractical for the entire re-entry procedure.

### 1.1 Re-entry from Orbit

Since the atmospheric composition and vehicle velocity change during the descent phase, a re-entry space-craft deals with variable flow regimes and the aerodynamic performances, together with aerothermal loading conditions, change accordingly.

A typical re-entry path of a space craft returning from low Earth orbit (LEO) is close to those reported in figure 1.1. At the beginning of the atmospheric re-entry, the space vehicle has a velocity of close to  $8 \text{ km/s}$  and it encounters the free molecular flow at about  $120 \text{ km}$  altitude. Then the vehicle flies through transitional flow regime and it reaches continuum

flow conditions at about 70 km altitude, where spacecraft velocity ranges from 7 to about 5 km/s.

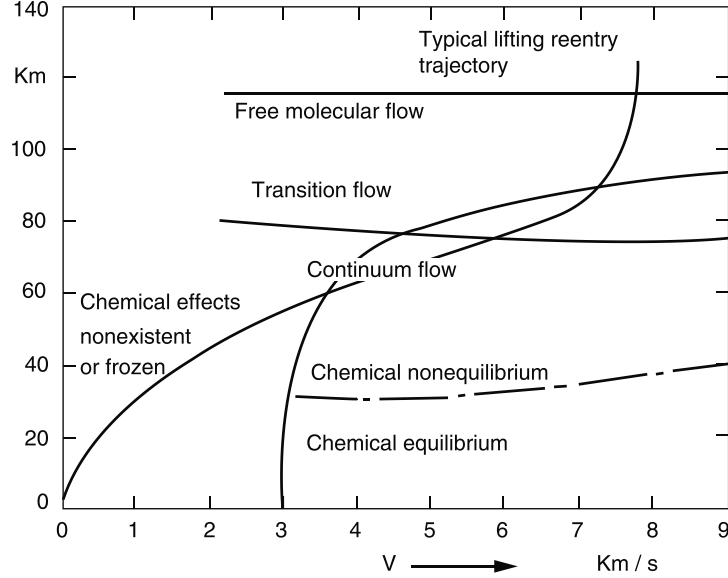


Figure 1.1: Stagnation-point flow regimes for re-entry vehicle (Viviani and Pezzella 2015).

Free molecular flow occurs when the flow is constituted by a rarefied gas. The distance that the molecules travel between consecutive collisions is called mean free path ( $\lambda$ ) and in rarefied gases it becomes comparable with the characteristic dimension of the flowfield. In this case the continuum hypothesis is not respected, and it is not possible to treat a gas using the macroscopic properties.

Conversely, for a gas with a high particles density, the intermolecular collision frequency is high. The *mean free path* becomes small compared to the characteristic dimension of the flowfield and the macroscopic properties vary continuously, thus the gas can be treated as a continuum.

An expression of *free molecular path* can be found from kinetic theory of gases:

$$\lambda = \frac{1}{\sqrt{2}\pi\sigma^2n} \tag{1.1}$$

where  $n$  is the molecules number per volume unit and  $\sigma$  [m] is the collision diameter.

Each flow regime is defined by comparing the *mean free path* to a characteristic dimension of the flow field, so it is possible to introduce an important non dimensional parameter named Knudsen number, defined as:

$$Kn = \frac{\lambda}{L_{ref}} \tag{1.2}$$

Three flow regimes can be individuated by mean of these parameters:

- 1. Free molecular flow  $Kn \gg 1$

- 2. Transitional flow
- 3. Continuum flow  $Kn \ll 0,01$

The characteristic length could be a dimension of a flowfield characteristic or of the body, for example the base radius for a blunt cone or the mean aerodynamic chord for a wing. The Knudsen number highlights that not only  $\lambda$  is important, but also  $L_{ref}$  which depends on the case studied. Indeed free molecular flow occurs at high altitudes where density is low,  $\lambda \gg L_{ref}$ . Nevertheless, the Knudsen number can be high also when the characteristic dimension is small, for example in cas of a flow through a shock wave where the characteristic dimension would be the thickness of the shock wave itself.

## 1.2 Re-entry Vehicle Design

The design of a entry space-craft is the result of choices aimed to fulfilling the missions requirements. In (Viviani and Pezzella 2015) the authors have identified some major mission drivers in:

- Manned or unmanned
- Reusable or disposable
- Large or small payload
- Atmospheric environment
- GN&C maneuverability (L/D)
- Entry speed range

The first one is the decision regarding manned or unmanned flight. Obviously a manned flight requires stricter constraints on deceleration (g) accordingly to human body, minimal duration, and higher factors of safety.

The re-usability pays particular attention on thermal protection. In case of a non-reusable space-craft, ablative materials are used. This kind of materials discharge heat loads. from their own erosion and vapour. For a vehicle that is designed for multiple use and long life cycle non-ablative, reflective heat shields will be used.

Guidance, navigation, and control (GN&C) is directly connected to L/D parameter. A design that required aeromaneuverability lead to a Vehicles with high L/D. High-drag bluff vehicles, such as capsules, with low L/D are necessary when maximum deceleration is required for direct entry aerobraking or aerocapture manoeuvrers.

The L/D, in turn, determines the flight angle of incidence which, determines wake impingement angle.

Direct entry capsules utilizing ballistic entry trajectories require very little GN&C control and hence can be designed to maximize drag characteristics. Aerobraking or aerocapture, on the other hand, will require somewhat more control, and a variety of considerations must be balanced to define an optimal configuration.

Thus two types of entry vehicle design are envisaged, those which are purely ballistic with no means to control the course of the trajectory save changes in drag and those which have a lifting capability where an on-board control system is required to shape the trajectory.

### 1.3 Ballistic and Lifting Re-Entry

In the entry phase the most important parameters for a vehicle are (Viviani and Pezzella 2015):

- Lifting parameter,  $\frac{m}{C_L S_{ref}}$
- Ballistic coefficient,  $\frac{m}{C_D S_{ref}}$
- Lift-to-drag ratio,  $\frac{L}{D}$

The effect of lifting parameter and ballistic coefficient on the vehicle re-entry trajectory is shown in figure 1.2. The vehicles with larger values penetrate deeper into the atmosphere before slowing.

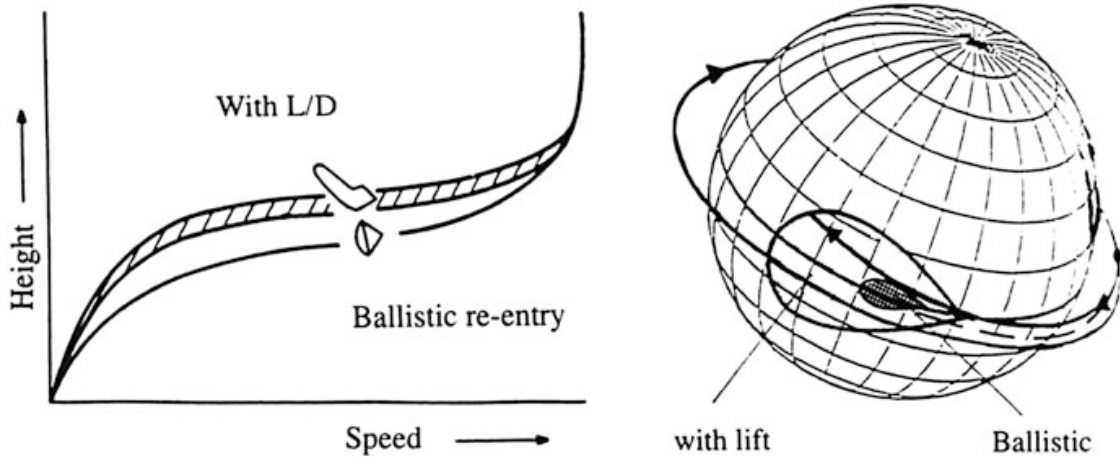


Figure 1.2: Influence of L/D for different configuration and landing region on Earth (Viviani and Pezzella 2015).

The increase of complexity and mass is compensated by a more flexibility on entry path thanks to moving surfaces. The lifting force allows to increase the margin of error in re-entry velocity or angle and “stretch” the size of the entry corridor. Controlling lift also improves accuracy over an aerocapture manoeuvre. Configurations with rather high aerodynamic efficiency, as opposed to ballistic vehicles where the lift is zero, have the advantage to control the lift vector, reducing level of deceleration and giving a manoeuvring capability. This allows to increase the landing region on Earth, as shown in figure 1.2 and to guide the vehicle directly to the desired landing area.

Moreover, the  $L/D$  affects the stagnation-point heat-transfer rate as is shown in figure 1.3. Lift allows the configuration to decelerate at higher altitudes when the value of the free-stream density is lower and consequently the aerodynamic heating will be lower at a given velocity. However, despite the decrease in heat flux, the heat load could increase due to the increase in flight time. The accurate prediction of peak and time-integrated heat fluxes is important for the selection and sizing of the thermal protection system (TPS) material.

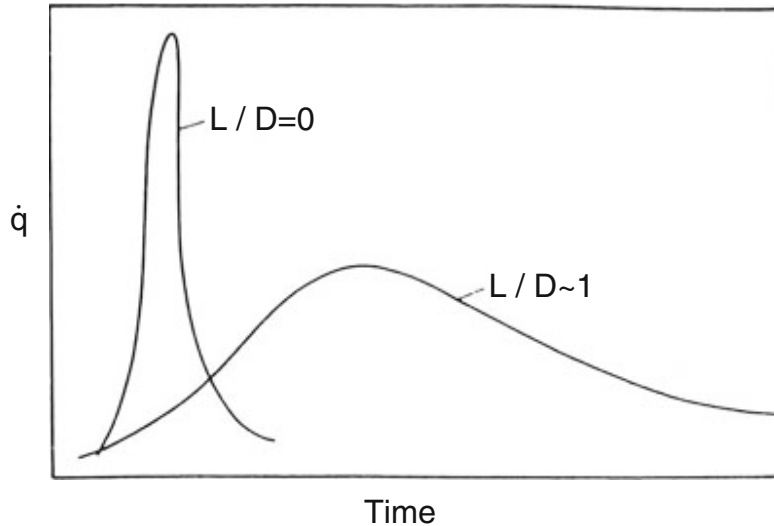


Figure 1.3: The effect of  $L/D$  on the reference heating-rate history (Viviani and Pezzella 2015).

Generally, in case of exploration missions, design philosophy is to provide, as much as possible, a minimum cost solution. Consequently, the adoption of a simple sphere cone with large half cone angle is the natural choice.

For a ballistic entry, the vehicle shape is chosen in order to ensure a high deceleration at the highest possible altitude. In this case a vehicle with a low ballistic coefficient accomplishes a direct entry and aims to lose sufficient kinetic energy in the upper atmosphere to achieve the desired velocity and altitude conditions for the later mission phases. To achieve a low ballistic coefficient, large area, high drag coefficient, low mass vehicle are required, therefore no guidance or control are installed. It is thus necessary to take into account a margin of dispersion. The aerobraking concept is, therefore, less costly than the aerocapture equivalent but places emphasis on the design of an acceptably low ballistic coefficient stable aeroshell. On the other hand, a large drag coefficient leads to a loss of stability, and since mass and cost budgets can not provide an onboard stability and control system, the geometric configuration has to be sufficiently stable in free flight.

## 1.4 Instability for Blunt-Body Shape

As cited in paragraph 1.3 sphere-cone and spherical section fore-bodies have been proven to be efficient designs for decelerating payloads from very large entry speeds, minimizing the peak heating to which the structure has to resist. This body shape is generally called

a *blunt body* and some examples are visible in figure 1.4, for example the Apollo Module Command and the planetary probe Huygens.

However, a dangerous aerodynamic property is associated with blunt vehicles. This is the dynamic instability that tends to begin near Mach 3.5 and increases with decreasing Mach number. This instability causes oscillations of the attitude around the equilibrium angle. If it is not damped it grows so much that affects landing trajectory or even a safe parachute deployment. Therefore, the suppression of such unstable movement is one of the key design points for a re-entry capsule (Schoenenberger and Queen 2008).

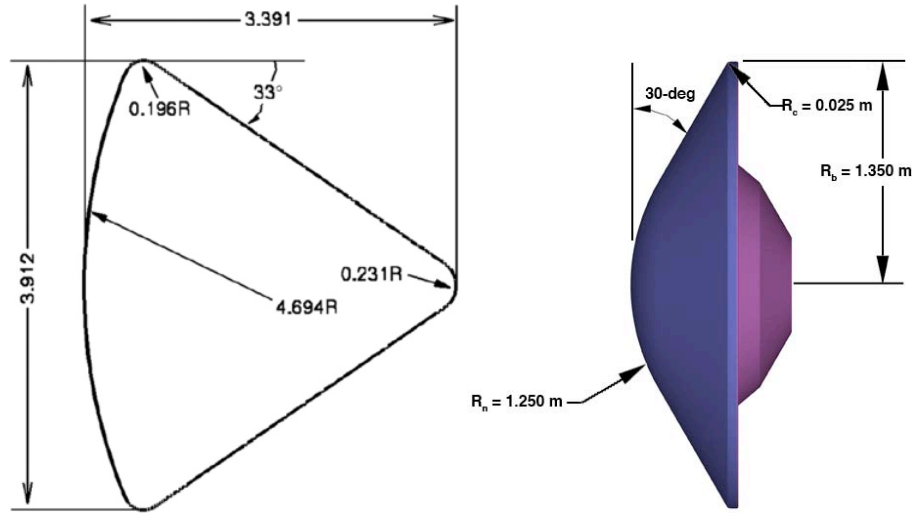


Figure 1.4: Apollo and Huygens shape.

Packaging and mass requirements tend to drive the back-shell shape, which varies according to the type of mission it has to face. The backshell geometry is thought to be the main factor affecting how the wake structure interacts with the body and consequently the level of vehicle dynamic stability.

### 1.4.1 Physics of the phenomenon

The first investigations about the dynamic stability of blunt bodies began in the 1950s when the development of space exploration and ballistic missile technology gained strength. At that time, engineers knew the phenomena of dynamic instability because even the aircraft dynamics suffered the same problem. However, due to the really different operating environments and geometries of atmospheric entry vehicles, engineers lacked an understanding of the problem in the early stages.

There is an extensive bibliography about the studies carried out at the time on this phenomenon: the analytical work of Allen (J. H. Allen 1957), Tobak (Tobak and H. J. Allen 1958) and the experimental investigations realized by Bird (Bird and Reese Jr 1958), Fletcher (Fletcher 1959), Short and Sommer (Short and Sommer 1959). These studies highlighted the unpredictable nature of the phenomenon, its sensitivity to shape and operational variables and the difficulties linked to analytical, numerical and experimental tests. However, the detailed mechanism remains largely unknown (Kazemba et al. 2012).

Recent studies, thanks to the achievements of CFD, have deepened the subject reaching a better understanding about the nature and the mechanism of this phenomenon, identifying two triggering causes: pitching moment hysteresis and flow separation and reattachment.

The first observation suggested the existence of a non-linear pitching moment slope caused by a finite temporal delay existing between the change of the attitude angle and the consequent variation of the pressure field around the body, showing the phenomenon of the hysteresis.

In this regard, experimental (Hiraki K. 1998) and numerical (Teramoto, Kouju Hiraki, and Fujii 2001) tests were carried out on Hayabusa capsule, which demonstrated this delay between aft-body fields and fore-body pressure. Teramoto data from his paper (Teramoto, Kouju Hiraki, and Fujii 2001) are presented in figures 1.5 and 1.6. This definitively proved that the dynamic stability of the capsule depends mainly on the behaviour of the base pressure and that the capsule is dynamically unstable when the change in the pitch-down moment induced by the base pressure distribution at positive pitch angle is delayed with respect to the change in the pitch angle. This time lag causes the phase delay of the base pressure. The base pressure distribution and delay are closely related to the vortices behaviour that develop downstream of the body.

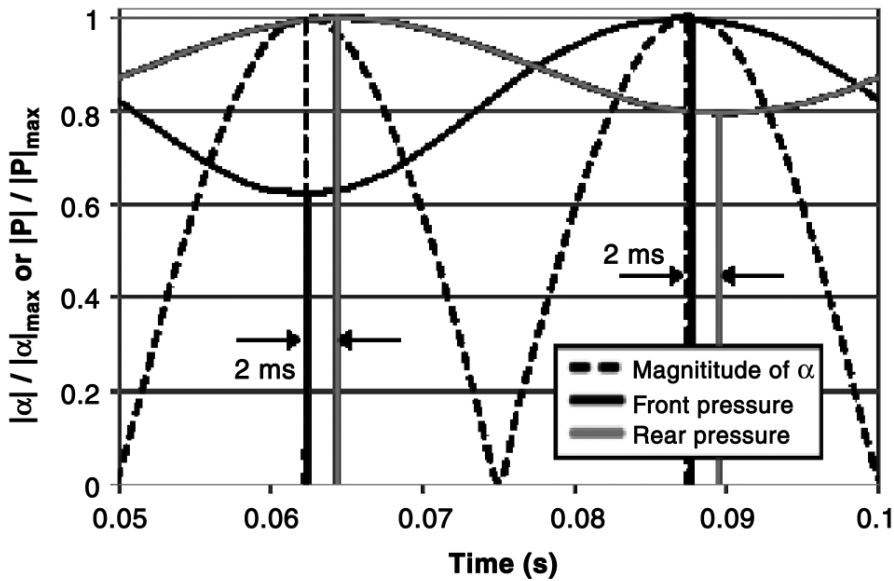


Figure 1.5: Pressure variation with pitching motion (Teramoto, Kouju Hiraki, and Fujii 2001).

This is not the only way in which the flow structure could generate unsteady dynamic forces. The second cause, as said previously, is flow separation and reattachment. Baillion (Baillion 1997) cited harmful effects of flow reattachment on a vehicle after flow separation. Just as the near-wake, the reattaching flow creates a zone of unsteady pressure forces that act on the rear portion of the vehicle and generate unsteady pitching moment. A theory was developed in Ericsson and Reding 1971 in order to predict the induced forces that act on the vehicle and cause instabilities. The application of this method to slender cylindrical

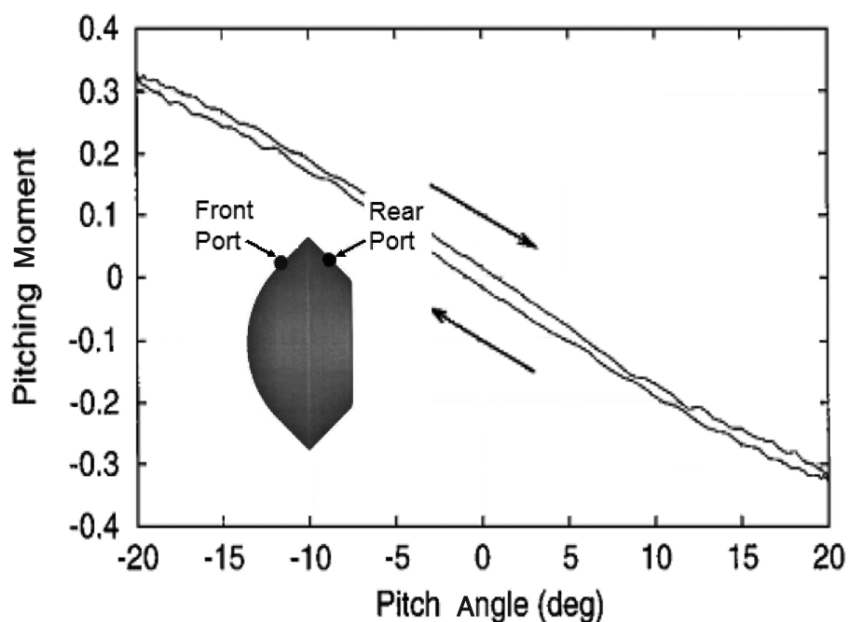


Figure 1.6: Corresponding hysteresis in pitching moment (Teramoto, Kouju Hiraki, and Fujii 2001).

bodies produced moderate success in damping determination, although a more descriptive picture about these process and its governing principles is still required.

## 1.5 Numerical investigation

Wind tunnel experiments, free flight experiments and numerical investigations are the main techniques to examine the dynamic behaviour of aerospace vehicles. In the wind tunnel free and forced oscillations are the most common measuring of dynamic behaviour.

Wind tunnel testing has traditionally been used to extract derivatives for aircraft based on scale models. The physical realism of wind tunnel data is well known, but it can be limited by blockage, scaling, Reynolds-number effects and support interference issues that prevents the proper modelling of the full-scale vehicle behaviour.

On the other hand, wind tunnel and free flight experiments are costly, hence today the numerical simulations are widely used, especially during the preliminary phases of the project, for dynamical investigation analysis, thanks to the low cost and high speed and accuracy achieved.

Some existing prediction methods are based on semi-empirical formulas for individual vehicle components. This is the DATCOM-type approach. Results obtained with these methods are rather rough and they often fail to display the critical behaviour of a particular configuration. Other methods are based upon linearised potential equation and they use oscillating boundary formulations for the unsteady effects. These methods provide accurate results as long as the aerodynamics is governed by irrotational flow and small perturbation.

Many of the existing theoretical methods are restricted to particular geometries such as slender bodies, delta wings, etc (Korfanty and Longo 2008).

At the end of the 90's CFD numerical methods for dynamic derivatives prediction, based on unsteady Navier-Stokes calculations, have been successfully applied. Navier-Stokes CFD solvers have reached a level of robustness and maturity to support routine use on relatively inexpensive computer clusters. A key functionality of CFD solvers is the ability to move the mesh accordingly to body motion. Rigid body motions can be treated by moving the mesh rigidly (Arbitrary Lagrangian-Eulerian formulation) in response to the applied sinusoidal motion. The mesh is deformed once per real time step during the unsteady calculation.

## 1.6 Scope and Overview of the present dissertation

In this thesis the dynamic stability of two re-entry vehicles, the Hayabusa capsule and the Space Rider, have been investigated numerically using forced oscillations technique in order to validate a numerical model that allows to calculate the dynamic derivatives of these two vehicles. The numerical method developed in “Evaluation of dynamic derivatives using computational fluid dynamics” has been reproduced using two commercial CFD codes. The validated procedure could reduce costs and time required by experimental tests, making the design phase faster.

First of all, the work done in Ravera and D'Ambrosio 2018 was resumed, analysing Hayabusa capsule and reaching useful informations about numerical approach. Afterwards, the Space Rider vehicle has been analysed with same procedure comparing the results with those present in database.

In both cases the setup is based on continuum hypothesis ( $Kn \ll 0.01$ ) and subsonic flow regime ( $0.3 < M < 0.7$ ). The fulfilment of the first hypothesis allows to use the Navier-Stokes equations while the second one imposed a compressible flowfield. The capsule was tested at various angle of attack of 0, 10 and 20 degrees, while Space Rider was only tested at an angle of attack of 65 degrees.

The 3D simulations were performed using two commercial solvers, ANSYS FLUENT, developed by ANSYS, and CFD++ by Metacomp. The capsule geometry was designed with ANSYS SPACE CLAIM, while the aeroshape of Space Rider was provided by TAS-I. Both bodies were meshed using ANSYS MESHING.

The first part of this thesis introduces some informations about the space-crafts missions and explains the methodology applied and numerical technique used to carry out the analyses. In the second part, results of 3D simulations are presented and discussed. Finally, conclusions and proposals for further analyses are reported in the last chapter.



## Chapter 2

# Mission analysis

The choice to start from Hayabusa is linked to its simple geometry that can be easily modelled and studied as a first approach. Moreover the presence of a database in literature, allowed to do comparisons concerning numerical results.

After the procedure developed had been validated, Space Rider shape was analysed. About this one a complete database and numerical results are available that allowed to reach a definitive validation of the procedure presented here.

Before talking about the numerical methods a summary about the two bodies and their mission is reported.

### 2.1 Musec-C Mission



Figure 2.1: Hayabusa (*Hayabusa: A technology Demonstrator 2005*).

The Hayabusa capsule was adopted by Institute of Space and Astronautics Science (ISAS) for MUSES-C mission. The main mission purpose was to verify some technologies developed to achieve a full-scale "sample return mission". These are: a highly fuel efficient ion engine,

an automatic navigation system to approach far-away asteroids by spacecraft self-control, sampling under microgravity and a re-entry capsule designed to be heat-resistant in order to return its captured samples to Earth.

The probe was launched in May 2003 and arrived at Itokawa asteroid, on September 12 2005. After remote scientific observations and terrain measurement, in November 2005 it conducted three descent operations and two touchdowns on Itokawa's surface. After its landing, the one-meter long sampler horn was extended from the bottom of "HAYABUSA" until to touch the Itokawa surface. A bullet was launched to crush the monolith and raise a curl of sand gravel, which went through the internal path of the horn. Fragments that reached "HAYABUSA" were then sampled.

In April 2007, Hayabusa started orbit transfer for returning to the Earth and then re-entered the atmosphere in June 2010 after overcoming many troubles. At an altitude of about 200 kilometres the return capsule was separated from probe and began descent path. Then the fore-body and aft heat shields of the capsule were separated at an altitude around 10 kilometres and the sampler container descended with a parachute until the touchdown at Woomera, Australia.

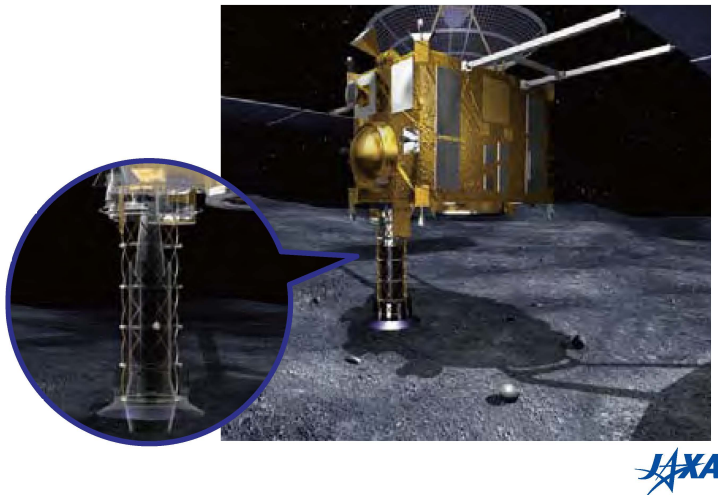


Figure 2.2: Hayabusa: sample collecting mechanism (*Asteroid Explorer Hayabusa 2005*).

### 2.1.1 Hayabusa Capsule

In figure 2.3 the shape of the re-entry capsule is represented. This was determined to respect the weight and dimension constraints, and to maximize the inside volume for installing the sample canister, parachute, pyrotechnic devices and electronics. The capsule weights 17 Kg and is constituted by a hemispherical nose with 202 mm in radius and a conical side body with 45 degrees in half cone angle. Maximum diameter is 404 mm, and the centre of gravity position is approximately 120 mm from the nose (Ishii and Koju Hiraki 2003).

One of the most peculiar features of the Muses-C mission was the re-entry velocity of the sample return capsule. It re-entered directly into the Earth's atmosphere, at about  $12 \text{ km/s}$ , and was exposed to a much higher temperature than the Space Shuttle's atmospheric

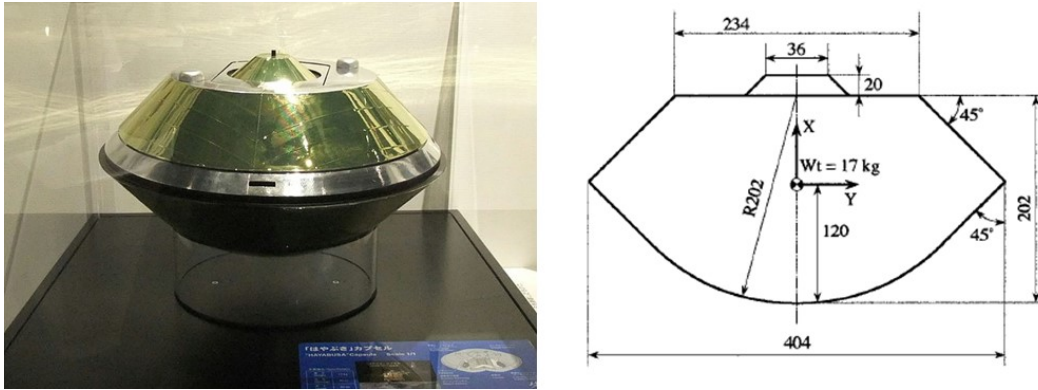


Figure 2.3: Hayabusa reproduction (on the left) and size (on the right) (Ishii and Koju Hiraki 2003).

re-entry. Its cooling system employed ablation cooling in which the heat-resistance material itself decreased while releasing heat, for this purpose a carbon phenolic resin was employed. Due to weight constraint, capsule had no active equipment for attitude control, therefore passive aerodynamic stability was ensured over the entire re-entry flight.

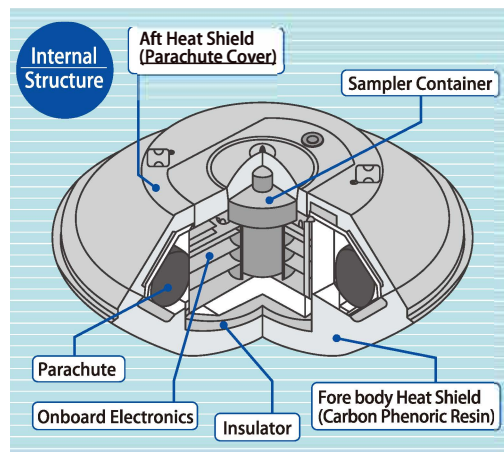


Figure 2.4: Technologies aboard the Hayabusa (*Asteroid Explorer Hayabusa* 2005).

### 2.1.2 Reference System and CAD Model

It is mandatory to establish a unique reference system. As shown in figure 2.5 the centre of gravity is fixed and located on the  $x$  axis at  $0.12\text{ m}$  behind the capsule apex. Referencing to Schoenenberger, Kutty, et al. 2014, the axis are organized in the following way:

- $x$  axis is placed along with revolution axis and the positive direction is towards the nose;
- $y$  axis is chosen in order to measure a positive pitch moment for positive angle of attack;

- $z$  axis is set in order to respect the right hand rule.

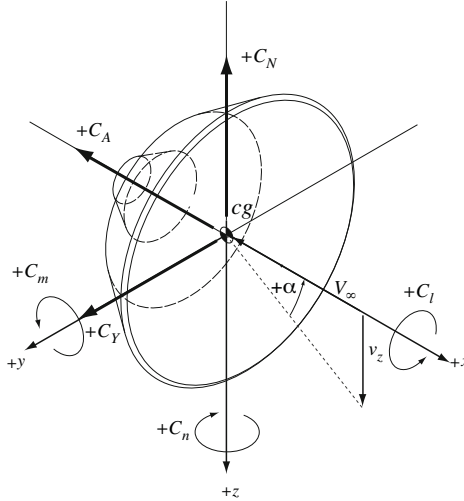


Figure 2.5: Forces and moments convention.

The reference length is  $L_{ref} = 0.404 \text{ m}$ , the reference surface is  $S_{ref} = 0.1282 \text{ m}^2$ , while the moment reference centre (MRC) is located in the centre of gravity.

Following the measures reported in figure 2.3 and the reference system shown in figure 2.5, a CAD model is realized on Ansys Space Claim.

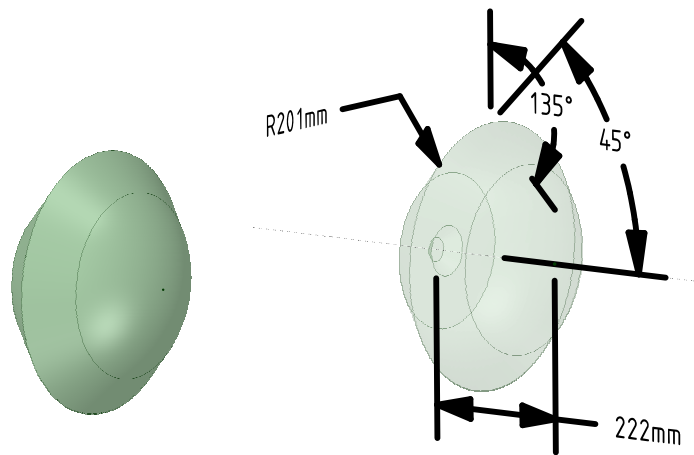


Figure 2.6: Hayabusa: CAD model.

### 2.1.3 Aerodynamic Database

In Ishii and Koju Hiraki 2003 is available a database of the capsule aerodynamic coefficients. The aerodynamic properties are function of Mach number and angle of attack and they are based on the wind tunnel data from the subsonic to supersonic regime, while in hypersonic

regime the data are based on numerical analyses. Moreover, using balloon drop tests the wind tunnel results in transonic regime are revised.

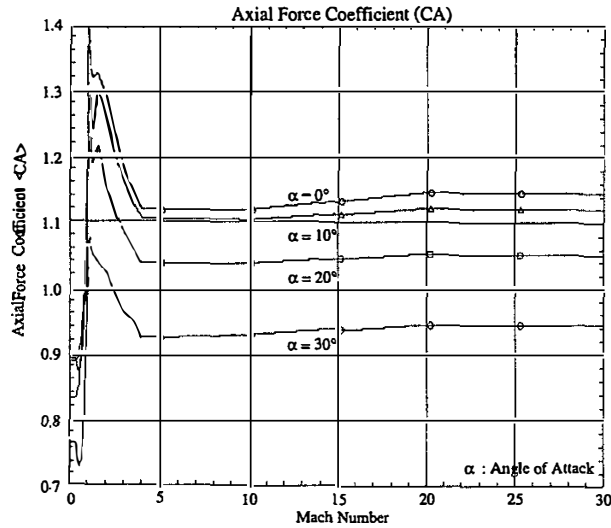


Figure 2.7: Axial force coefficient as function of Mach number and angle of attack (Ishii and Koju Hiraki 2003).

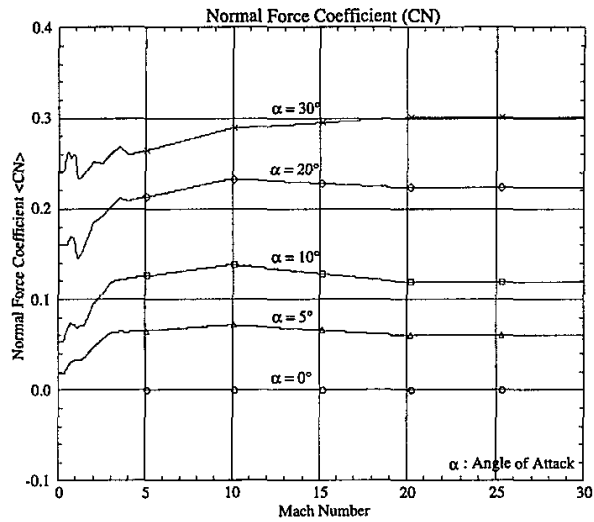


Figure 2.8: Normal force coefficient as function of Mach number and angle of attach (Ishii and Koju Hiraki 2003).

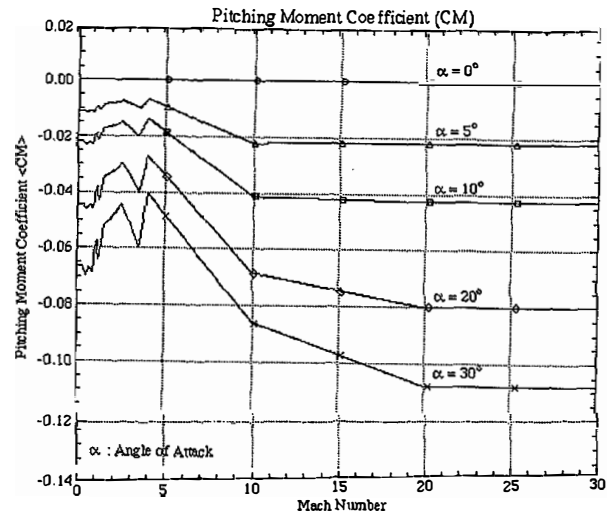


Figure 2.9: Pitching moment coefficient as function of Mach number and angle of attach (Ishii and Koju Hiraki 2003).

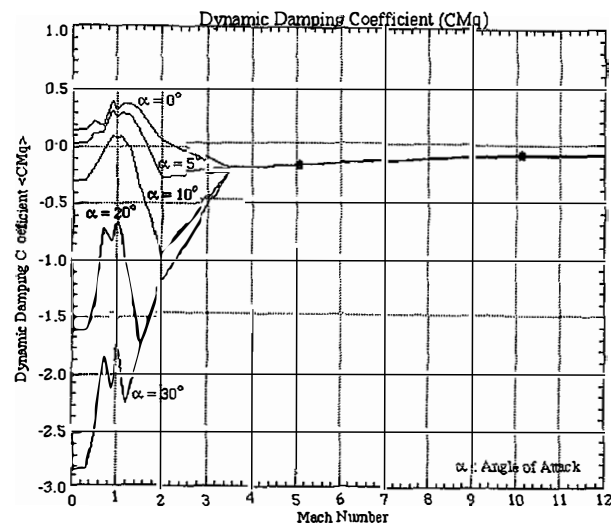


Figure 2.10: Dynamic damping coefficient as function of Mach number and angle of attach (Ishii and Koju Hiraki 2003).

## 2.2 Space Rider Program

In the framework of the Future Launchers Preparatory Programme (FLPP), the ESA aimed to provide a development plan for the design and test for a technology platform capable to perform a manoeuvred re-entry flight. The vehicle was also intended to serve as a test bed for in-flight qualification of vehicle subsystems and systems and to provide another source of data on fundamental hypersonic aero-thermodynamic phenomena for validation of tools,

databases, and design processes (Viviani and Pezzella 2015).

In this context the Italian Space Agency presented their own Programme for Reusable In-orbit Demonstrator in Europe (PRIME program) called Intermediate eXperimental Vehicle (IXV).

The IXV mission was successfully performed on the 11th of February 2015, completing a parabolic flight and returning intact in the Pacific Ocean. All flight hardware and all flight data were successfully recovered, and through the telemetry of the flight segment, acquisition of the ground segment and on-board registration, it was confirmed that the flight was completed with success.

### 2.2.1 Space Rider Vehicle

The Space Rider program is the successor of the IXV experience and it applies all design, development and flight experiences for the first European reusable space transportation system. This platform provides European routine access and return from orbit, with the purpose to perform operation and experimentation in low Earth orbit and also a safely return on Earth, allowing payload recovery and rapid vehicle re-utilization for successive missions (Balossino et al. 2017).

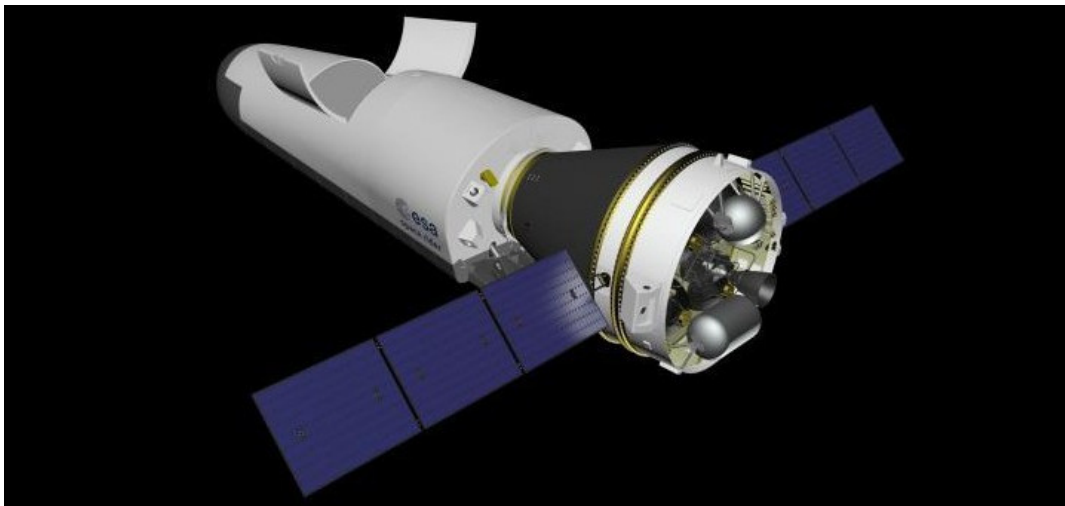


Figure 2.11: Space Rider with service module.

The baseline system architecture is a combination of a modified version of the AVUM (Vega C fourth stage Space Rider that allows to to operate in orbit for about two months) as disposable de-orbit module and an IXV derived lifting-body as re-entry reusable module. The re-entry module can host payloads in the Multi-purpose Cargo Bay.

The re-entry module is a lifting body based on the IXV 1:1 scale vehicle, which had already demonstrated space entry and hypersonic/supersonic flight capabilities. Respect to the IXV mission, the Space Rider will have the capability of landing on ground and re-usability, thus an appropriate recovery approach has been defined based on adoption of a Descent and Landing system. For the descent phase an exploiting parachutes will be used, while a Landing Gears will allow the aircraft to be laid down (Marini et al. 2017).

Survival to atmospheric re-entry environment will be guaranteed by a thermal protection system based on ceramic and ablative materials and by a control system with aerodynamic control surfaces and reaction control rockets. After the hot re-entry phase the vehicle will tackle the descent phase aided by a guided parafoil that will bring the spacecraft up to a soft landing either on a runway or on an open field (*Space Rider PRIDE 2017*).

The reference mission for the spacecraft design foresees a rendezvous with the International Space Station that will release scientific payloads to be captured by the vehicle robotic arm, stored in the cargo bay and brought on ground. Space-Rider will be capable to (*Space Rider homepage 2017*):

- free-flying applications such as experiments in microgravity;
- in-orbit technology demonstration and validation for applications for:
  - exploration, such as robotics;
  - Earth observation, such as instrumentation;
  - others, such as Earth science, telecommunication;
- surveillance applications such as Earth disaster monitoring, satellites inspection.



Figure 2.12: Space-Rider concept of operations (Marini et al. 2017).

Space Rider will be launched on Vega-C from Europe’s Spaceport in Kourou, French Guiana, with up to 800 kg of cargo and remain in space in a low-drag altitude orbit for about two months. It is designed to operate at different orbital inclinations, from equatorial to high-latitude. For orbits with inclination more than  $37^\circ$ , landings will be performed at the Portuguese Santa Maria Island in the Azores archipelago. The Azores archipelago is a suitable European landing location for missions that require high-latitude inclinations because it allows Space Rider to return at the same latitude as its operational orbit, requiring fewer de-orbiting manoeuvres (*Space Rider homepage 2017*). For lower

inclination missions, French Guiana and Dutch Curaçao are being considered (*Space Rider Esa Multimedia 2018*).

As far as the descent phase is concerned, since lifting body vehicle stability decays at high angles of attack and low airspeeds, a combination of parachutes and para-foil has been investigated. The Descent System will be triggered at subsonic speed, below Mach 0.8, a first phase of deceleration guaranteed by drogue parachute(s) at about 15 km altitude, then from a Mach number of 0.22 and 0,18 parafoil will be deployed. Then the controlled descent phase will begin with a vertical speed lower than 0.3 m/s and with 35 m/s horizontal speed. This solution will allow to land safely, reducing operating costs as well as recovery and refurbishment time of the vehicle (Balossino et al. 2017).

### 2.2.2 Reference System and CAD Model

The reference length is  $L_{ref} = 4.4 \text{ m}$ , the reference surface is  $S_{ref} = 7.26 \text{ m}^2$ , while the moment reference centre (MRC) is located in the plane of symmetry at 58% of the reference length from the nose.

- **x** axis is placed along with revolution axis and the positive direction is towards the nose;
- **y** axis is chosen in order to measure a positive pitch moment for positive angle of attack;
- **z** axis is set in order to respect the right hand rule.

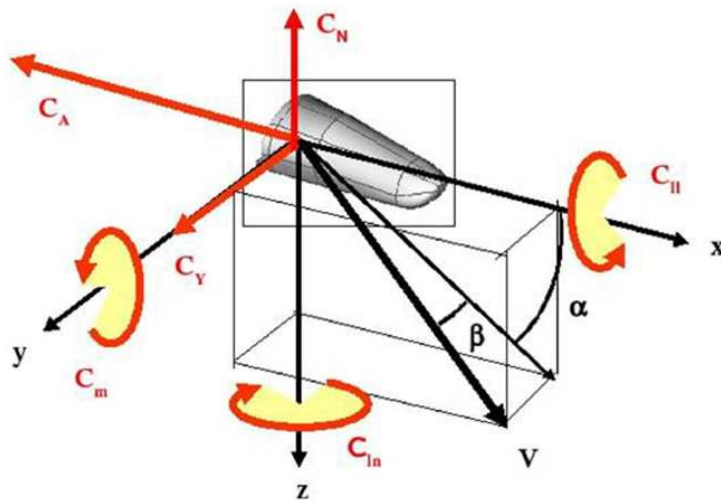


Figure 2.13: Aerodynamic convention (Marini et al. 2017).

In figure 2.14 it is reported the Space Rider CAD provided from TAS-I.

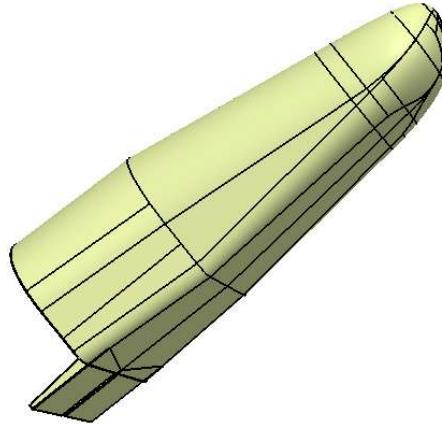


Figure 2.14: Space Rider CAD model.

### 2.2.3 Aerodynamic Database

The values of the coefficients and aerodynamic derivatives for Space Rider were extracted from an aerodynamic database provided by TAS-I. Specifically to the static coefficients, they refer to tests carried out in the wind tunnel for the IXV aero-shape which for what concerns the aerodynamic part is the same as the Space Rider aircraft. Instead the aerodynamic derivatives are proper to Space Rider and refer to numerical tests.

AoA [deg]	Database		
	$C_A$	$C_N$	$C_m$
$3\sigma$	0.0115	1.1305	0.0409
<b>65</b>	<b>0.0260</b>	<b>1.0255</b>	<b>0.0199</b>
$3\sigma$	-0.0635	0.9205	-0.0011

Table 2.1: Aerodynamic coefficients from database with uncertain values at  $3\sigma$ .

AoA [deg]	Data Sheet			
	$C_{m\alpha}$	$C_{m\dot{\alpha}}$	$C_{mq}$	$C_{m\dot{q}}$
65	-0.211	1.336	-0.06	-

Table 2.2: Aerodynamic derivatives from database.

## Chapter 3

# Background theory: aerodynamic stability

Stability is an equilibrium property of physic systems and describes the its behaviour in the near of equilibrium point. In this acceptance there are three types of equilibrium. Neutral equilibrium is when for each little perturbation a system assumes a new stable position. A system is in stable equilibrium when even it is disturbed with a little perturbation it returns to its initial state. Conversely, an unstable system lost its equilibrium state when it is perturbed.

Now, imagine to leave a ball on a semi-spherical surface. The equilibrium point is in the lower point of the surface. When the ball is released it tends to the equilibrium point but due to its kinetic energy he passes that point and reach a new height. The ball oscillates around the equilibrium point with gradually smaller amplitude until to stop at the lowest point of the surface. In this scenario it is possible to distinguish two aspects: the tendency to return to equilibrium point and oscillations behaviour over time. The first feature falls into static stability acceptance meanwhile the second falls into dynamic stability acceptance. Intuitively static instability implies dynamic instability, but static stability does not generally guarantee dynamic stability.

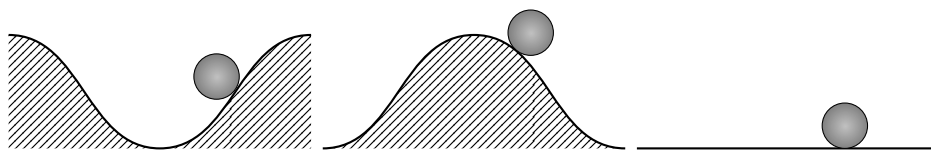


Figure 3.1: In order: stable, unstable and neutral equilibrium.

With reference to a vehicle, the design can be done in such a way that the stability is ensured without a particular control system. This type of stability is called *inherent* aerodynamic stability, but for particular design this is not possible so a *de-facto* stability is implemented, in which stability requirements are met with moving surfaces and the aid of a control system augmented with sensors and feedback. Generally, for a re-entry capsule, due to restrictive weight requirements it is preferable to ensure an inherent stability, avoiding to install active attitude control systems.

In this chapter the link between aerodynamic forces/moments and stability is discussed in the first part, then the forced oscillation method is shown in order to extract the aerodynamic derivatives.

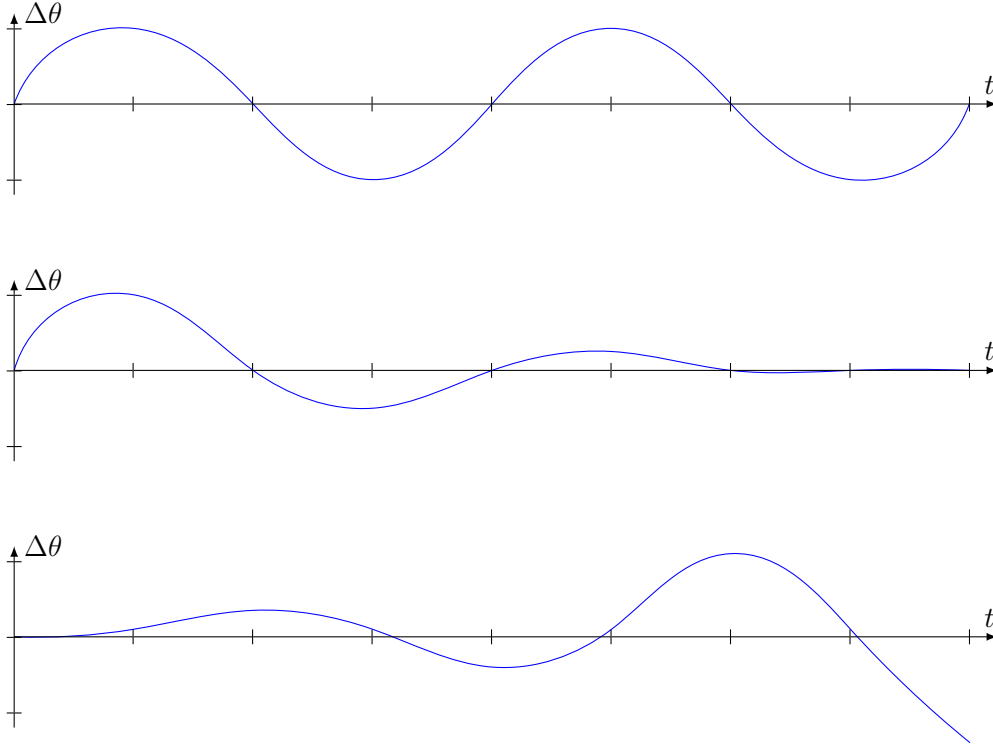


Figure 3.2: Dynamic behaviour: neutral, stable and unstable.

### 3.1 Stability Derivatives

Stability is usually associated with the response trajectory following the application of a disturbance on a physical system at static equilibrium position. These disturbances could be internal such as changes in the system configuration, changes in centre of gravity locations, or changes in the control surface deflections, but also external, i.g. turbulence or wind gusts. For the specific case, all of these changes have effects on the aerodynamic forces and moments on the vehicle.

In fluid dynamics dimensionless parameters are largely used, such as Mach number, Reynolds number, and Knudsen number and also dimensionless force and moment coefficients. An aerodynamic force coefficient is defined as:

$$\text{Force coefficient} = \frac{\text{Force}}{q_{\infty} S_{ref}} \tag{3.1}$$

while moment coefficient is defined as:

$$\text{Moment coefficient} = \frac{\text{Moment}}{q_{\infty} S_{ref} L_{ref}} \tag{3.2}$$

where:

$$q_\infty = \text{Dynamic pressure} = 1/2\rho_\infty V_\infty^2 \quad (3.3)$$

$$\rho_\infty = \text{Free-stream mass density of fluid} \quad (3.4)$$

$$V_\infty = \text{Free-stream fluid velocity} \quad (3.5)$$

About the body axes there are axial, normal, and lateral force coefficients ( $C_A$ ,  $C_Y$ ,  $C_N$ ), roll, pitch, and yaw moment coefficients ( $C_l$ ,  $C_m$ ,  $C_n$ ). These coefficients are function solely of the flight conditions and vehicle configuration,  $C_j = C_j(\alpha, \beta, M_\infty, h, \delta_i, p, q, r, \dot{\alpha}, \dot{\beta})$ , where  $j$  represents each of the individual force and moment coefficients,  $h$  is the altitude,  $\delta_i$  represents any other configuration such as control surface settings, and  $p, q$ , and  $r$  are the rotation rates about the body axes.

Bryan was the first on 1911 to introduce a representation of aerodynamic force and moment coefficients by means stability and control coefficients (Bryan 1911). The technique proposed by Bryan assumes that the aerodynamic forces and moments can be expressed in terms of perturbation variables. Perturbation variables are the instantaneous changes from the reference conditions for the translational velocities, angular velocities, control deflections, and their temporal derivatives. With these assumption, the aerodynamic forces and moments can be expressed by means of a Taylor series expansion. For example:

$$\Delta C_M(\alpha, \beta, M_\infty, h, \delta_i, p, q, r, \dot{\alpha}, \dot{\beta}) = \frac{\partial C_{M\alpha}}{\partial \alpha} \Delta \alpha + \frac{\partial C_{MM_\infty}}{\partial M_\infty} \Delta M_\infty + \dots + H.O.T. \quad (3.6)$$

The contribution to  $C_M$  due to the change in incidence  $\alpha$  is just  $\frac{\partial C_{M\alpha}}{\partial \alpha} \Delta \alpha$ . The term  $\frac{\partial C_{M\alpha}}{\partial \alpha}$  is called stability derivative and is evaluated at the reference flight condition. The same discuss is possible to apply it to the other terms.

## 3.2 Stability and Stability Derivatives

For thesis aim, the hypothesis of decoupling between lateral directional dynamics ( $C_N$ ,  $C_l$ ,  $C_n$ ) and longitudinal one ( $C_A$ ,  $C_Y$ ,  $C_m$ ) is made. In particular, attention has been paid to characterisation of longitudinal stability in symmetric fly at a specific velocity, altitude and angle of attack. Furthermore, the free body can rotate only around pitching axis. Thus, pitching moment coefficient can be expressed as:

$$C_M = C_{M0} + C_{M\alpha} \alpha + C_{M\dot{\alpha}} \dot{\alpha} \left( \frac{L_{ref}}{V_\infty} \right) + C_{Mq} q \left( \frac{L_{ref}}{V_\infty} \right) + C_{M\dot{q}} \dot{q} \left( \frac{L_{ref}}{V_\infty} \right)^2 \quad (3.7)$$

Static stability associated with a vehicle longitudinal axis normally is addressed by the sign of  $C_{M\alpha}$ . To obtain a stabilizing response this derivative must be negative, in this way when the angle of attack increases due to a perturbation a negative moment develops and restore the flight trim configuration.

The  $\dot{\alpha}$  and  $q$  derivatives owe their existence to the fact that the pressure distribution around the body does not adjust itself instantaneously to its equilibrium value when the

angle of attack and the pitch angle are suddenly changed. It is necessary to treat the two terms distinctly because they induce different longitudinal distribution of the normal velocity. In fact considering a free-flying aircraft, the distribution due to the angle of pitch variation (i.e. due to the pitching velocity  $q$ ) varies along chord and intersects zero at the axis of rotation (figure 3.3), while the distribution due to the angle of attack variation is constant along the chord (figure 3.4). Although they are two different concepts, in a rotation around the pitch axis their effects overlap.

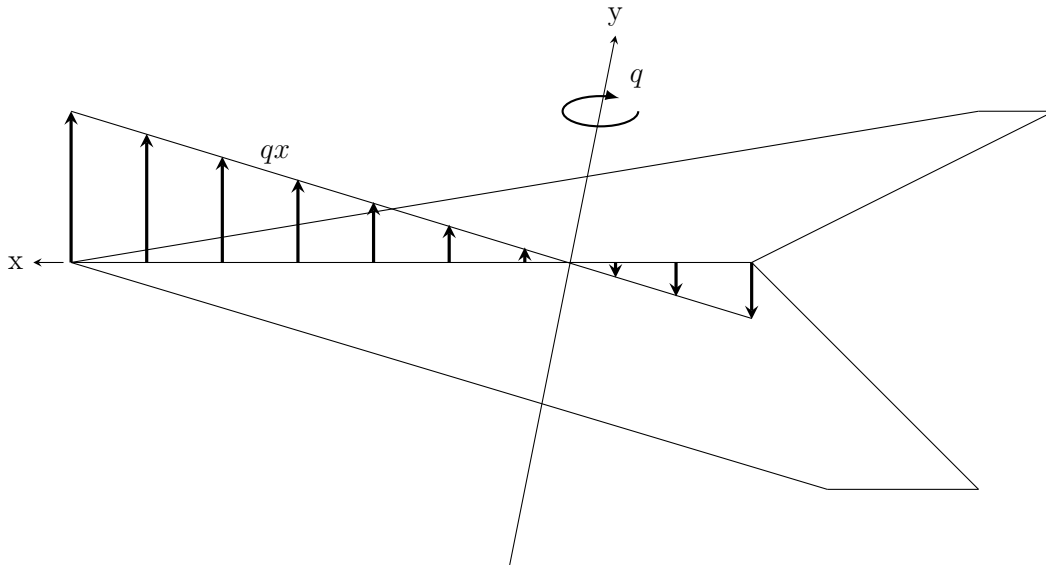


Figure 3.3: Velocity distribution along the chord due to a rotation around the pitch axis.

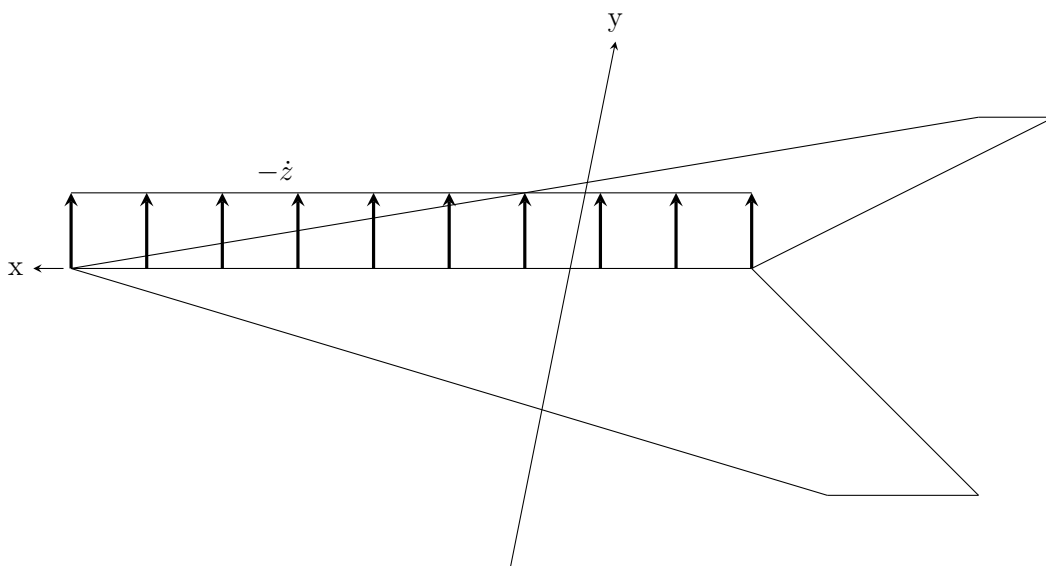


Figure 3.4: Velocity distribution along the chord due to a translation along the z-axis.

In unsteady oscillatory motion, static terms are not enough to express forces and moments. They are no longer in phase with motion and the non-stationary terms take on more weight; thus they depend also on the rate of change of the aircraft motion.

The  $C_{mq}$  is called *damping derivative*. While  $C_{m\dot{\alpha}}$  derivative is labelled *acceleration derivatives* since, from the aerodynamic point of view, the effects due to a vertical acceleration are equivalent to those due to a time rate of change in the angle of attack. This information is used to separate the purely-rotary derivatives  $C_{mq}$  from fixed-axis oscillatory counterparts  $C_{mq} + C_{m\dot{\alpha}}$  (Orlik-Rückemann 1981).

The sum of the two terms,  $C_{mq} + C_{m\dot{\alpha}}$ , takes the name of *damping sum* and for a vehicle dynamically stable it is negative. The negative sign induce a moment that dampens the oscillations of motion.

### 3.3 Forced Oscillation Technique

There are four main experimental methods for determining the dynamic stability of a body that involve the use of a wind-tunnel. Two of these make use of a support, called sting, to hold back the body: free oscillations and forced oscillations technique. In the first the body is exposed to the flow and is free to oscillates, while for the second support impose a specific motion to the body. Another technique is free-flight wind-tunnel test in which a scaled body is monitoring while drop down eliminating the intrusive effect of the sting. Vehicle observations are made in test section of the wind tunnel with Schlieren photography and high-speed video to capture the pitching behaviour and wake structure. Similar to the free-flight wind-tunnel methods, ballistic range testing offers free-flight dynamic behaviour without the constraints imposed by supports. A scale model is fired from a gun and travels through measuring stations where position, speed and orientation are recorded together with the current time step. Ballistic range testing is generally chosen over free-flight wind-tunnel testing because it offers more pitch cycle observations, and reducing uncertainty (Kazemba et al. 2012).

The forced oscillations technique is the best to be implemented in a CFD analyse, and it is the method chosen in this work to extract the aerodynamic derivative. In this chapter an overview on this technique and the consequence data reduction is shown.

With the forced oscillations technique, a specific periodic motion is imposed to the body. In particular, for the aerodynamic derivative relative to pitching moment a sinusoidal variation around pitching axes is imposed to the angle of attack.

$$\alpha(t) = \alpha_0 + \Delta\alpha(t) = \alpha_0 + A \sin(\omega t) \quad (3.8)$$

Where  $\omega = 2\pi f$ ,  $f$  is the frequency and  $A$  is the amplitude of oscillation. Angle of attack and pitch angle are related by this kinematic relation:

$$\theta = \alpha + \gamma \quad (3.9)$$

Where  $\gamma$  is the ramp angle. The pitch angle variation law is the following:

$$\theta(t) = \alpha_0 + \gamma + A \sin(\omega t) \quad (3.10)$$

With these relations it is possible to obtain the time rate of change in the angle of attack and pitching rate:

$$\frac{\partial \alpha}{\partial t} = \dot{\alpha} = \omega A \cos(\omega t) = \frac{\partial \theta}{\partial t} = q \quad (3.11)$$

$$\frac{\partial q}{\partial t} = \dot{q} = -\omega^2 A \sin \omega t \quad (3.12)$$

All these relations can be substituted in the linear relation of  $C_M$  :

$$C_M = C_{M0} + C_{M\alpha} \alpha + C_{M\dot{\alpha}} \dot{\alpha} \left( \frac{L_{ref}}{V_\infty} \right) + C_{Mq} q \left( \frac{L_{ref}}{V_\infty} \right) + C_{M\dot{q}} \dot{q} \left( \frac{L_{ref}}{V_\infty} \right)^2 \quad (3.13)$$

To obtain:

$$\begin{aligned} C_M = C_{M0} + C_{M\alpha} \alpha_0 + C_{M\alpha} A \sin(\omega t) + C_{M\dot{\alpha}} \omega A \cos(\omega t) \left( \frac{L_{ref}}{V_\infty} \right) + \\ + C_{Mq} \omega A \cos(\omega t) \left( \frac{L_{ref}}{V_\infty} \right) - C_{M\dot{q}} \omega^2 A \sin(\omega t) \left( \frac{L_{ref}}{V_\infty} \right)^2 \end{aligned} \quad (3.14)$$

Gathering the constant terms in  $C_0$  and the terms dependent by sine and cosine, it is possible write the following expression:

$$C_M = C_0 + \underbrace{A\omega (C_{M\dot{\alpha}} + C_{Mq}) \left( \frac{L_{ref}}{V_\infty} \right)}_{out-phase\ component} \cos(\omega t) + A \underbrace{\left[ C_{M\alpha} - C_{M\dot{q}} \left( \frac{\omega d}{V_\infty} \right)^2 \right]}_{in-phase\ component} \sin(\omega t) \quad (3.15)$$

The form obtained can be associated to the 1<sup>st</sup> Fourier coefficients:

$$C_M = C_0 + C_{M_{1c}} \cos(\omega t) + C_{M_{1s}} \sin(\omega t) \quad (3.16)$$

The procedure shown produces two terms that take the name of out-of-phase and in-phase coefficients (Thompson, Frink, and Murphy 2010), respectively:

$$C_{M_{1c}} = A\omega (C_{M\dot{\alpha}} + C_{Mq}) \left( \frac{L_{ref}}{V_\infty} \right) \quad (3.17)$$

$$C_{M_{1s}} = A \left[ C_{M\alpha} - C_{M\dot{q}} \left( \frac{\omega L_{ref}}{V_\infty} \right)^2 \right] \quad (3.18)$$

Considering only the time-dependent terms (contribution at  $C_M$  due to oscillations ) the two components can be calculated as shown in Da Ronch et al. 2012:

$$C_{M_{1c}} = \frac{1}{n_c T} \int_0^{n_c T} \Delta C_M \cos(\omega t) dt \quad (3.19)$$

$$C_{M_{1s}} = \frac{1}{n_c T} \int_0^{n_c T} \Delta C_M \sin(\omega t) dt \quad (3.20)$$

As reported in the section 3.2 the rotation around pitching axis produces two different effects that are superimposed. In fact from  $C_{M_{1c}}$  it can not possible to extract the single aerodynamic derivatives. To do that it is necessary to impose a new oscillation motion. In particular to extract  $C_{M\dot{\alpha}}$  and  $C_{M\alpha}$ , a variation law of the angle of attack, with pitch angle constant and equal to, zero has to be imposed. This is possible with a periodic motion along  $z$  axis:

$$z = z_0 \sin(\omega t) \quad \Rightarrow \quad \frac{\partial z}{\partial t} = \dot{z} = \omega z_0 \cos(\omega t) \quad (3.21)$$

The body animated by  $\dot{z}$  motion sees a variation of angle of attack, but its body axis remains aligned to local horizontal axis, so pitch angle is zero and constant. With reasonable error, for  $\dot{z}/V_\infty \ll 1$  it is possible to calculate angle of attack variation approximating the arctangent to its argument:

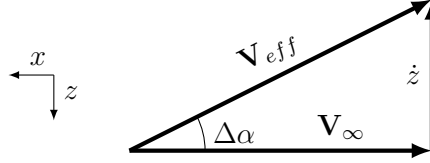


Figure 3.5: Angle of attack due to  $\dot{z}$  velocity.

$$\Delta\alpha = \arctan\left(\frac{\dot{z}}{V_\infty}\right) \approx \frac{\dot{z}}{V_\infty} = \frac{\omega z_0 \cos(\omega t)}{V_\infty} \quad (3.22)$$

Referring to the convention shown above, if the body moves along  $z$  axis, the flow field from body viewpoint is similar to see a free stream with a velocity component in opposite direction. Combining the two component the resulting angle of attack is positive. The complete angle of attack's law is:

$$\alpha(t) = \alpha_0 + \Delta\alpha(t) \approx \alpha_0 + \frac{\omega z_0 \cos(\omega t)}{V_\infty} \quad (3.23)$$

and its time rate of change:

$$\frac{\partial \alpha}{\partial t} = \dot{\alpha} = -\frac{\omega^2 z_0 \sin(\omega t)}{V_\infty} \quad (3.24)$$

Remembering that:

$$\theta = 0 \quad \Rightarrow \quad \frac{\partial \theta}{\partial t} = q = 0 \quad (3.25)$$

The  $C_M$  expression 3.7 will be:

$$C_M = C_{M0} + C_{M\alpha} \alpha + C_{M\dot{\alpha}} \dot{\alpha} \left(\frac{L_{ref}}{V_\infty}\right) \quad (3.26)$$

So, substituting all the expression found:

$$C_M = C_{M0} + C_{M\alpha} \alpha_0 + C_{M\alpha} \frac{\omega z_0 \cos(\omega t)}{V_\infty} - C_{M\dot{\alpha}} \frac{\omega^2 z_0 \sin(\omega t)}{V_\infty} \left( \frac{L_{ref}}{V_\infty} \right) \quad (3.27)$$

Doing the same steps executed upon, it is possible to recognize the out-phase and in-phase component:

$$C_M = C_0 + \underbrace{C_{M\alpha} \frac{\omega z_0}{V_\infty}}_{out-phase\ component} \cos(\omega t) - \underbrace{C_{M\dot{\alpha}} \frac{\omega^2 z_0}{V_\infty} \left( \frac{L_{ref}}{V_\infty} \right)}_{in-phase\ component} \sin(\omega t) \quad (3.28)$$

Again, the form obtained can be associated to the 1<sup>st</sup> harmonic Fourier's coefficients:

$$C_M = C_0 + C_{M_{1c}} \cos(\omega t) + C_{M_{1s}} \sin(\omega t) \quad (3.29)$$

And the *out-phase component* and *in-phase component* are in the following form:

$$C_{M_{1c}} = C_{M\alpha} \frac{\omega z_0}{V_\infty} \quad (3.30)$$

$$C_{M_{1s}} = -C_{M\dot{\alpha}} \frac{\omega^2 z_0}{V_\infty} \left( \frac{L_{ref}}{V_\infty} \right) \quad (3.31)$$

These two component can be calculated as shown previously:

$$C_{M_{1c}} = \frac{1}{n_c T} \int_0^{n_c T} \Delta C_M \cos(\omega t) dt \quad (3.32)$$

$$C_{M_{1s}} = \frac{1}{n_c T} \int_0^{n_c T} \Delta C_M \sin(\omega t) dt \quad (3.33)$$

and then extracting the terms  $C_{M\alpha}$  and  $C_{M\dot{\alpha}}$  it is possible to calculate  $C_{M_q}$  and  $C_{M\dot{q}}$  using the expressions 3.17 and 3.18.

# Chapter 4

## Numerical Techniques

The build-up of test required the adoption of particular numerical techniques. Over the years, a particular procedure has been established for the calculation of aerodynamic derivatives using the forced oscillations method, called the ALE approach. This numerical method uses a mobile grid whose law is completely independent from the flow. This method is implemented in both Fluent and CFD++, however tests have proved numerical errors spread in Fluent. Thus, Chimera technique has been adopted using a moving and a fixed domain. This chapter presents two sections concerning the discussion of the two methods and a section in which models and algorithms used are shown.

### 4.1 Arbitrary Lagrangian Eulerian Approach

The fluid mechanics equations are classically written in two kinematic descriptions: Lagrangian and Eulerian. In Lagrangian algorithms, the computational cells move along with local fluid velocity and allows to track free surfaces and interfaces between different materials. However, this capability may lead to a large computational grid distortion and recourse to frequent re-meshing. In Eulerian algorithms the computational nodes are fixed while the flow evolves; they are more robust and widely used in fluid dynamics. The weakness reveals in simulations involving interactions of multi-materials, where extra numerical procedures are required to identify the interfaces, generating numerical errors. Moreover, in complex flow, accuracy and details are wasted due to lacking resolution.

To cope with each algorithm defects, a new technique has been developed, capable to maintaining the best features of Lagrangian and Eulerian approaches (Donea et al. 2004). Because of this flexibility the method is referred as Arbitrary Lagrangian–Eulerian (ALE) technique and it was proposed in Hirt, Amsden, and Cook 1974 to solve fluid dynamics in a moving and deforming grid. In fact, in ALE formulations, the grids for the computational domain can move arbitrarily and independently from fluid motions, which makes the code more robust in moving boundary simulations. Thanks to this freedom, the approach can handled greater mesh distortions than a purely Lagrangian method and with more resolution than that afforded by a purely Eulerian approach.

It is important to note that the influence of an ALE formulation in flow problems is on the convective terms that have to be rewritten to account mesh motion, while all

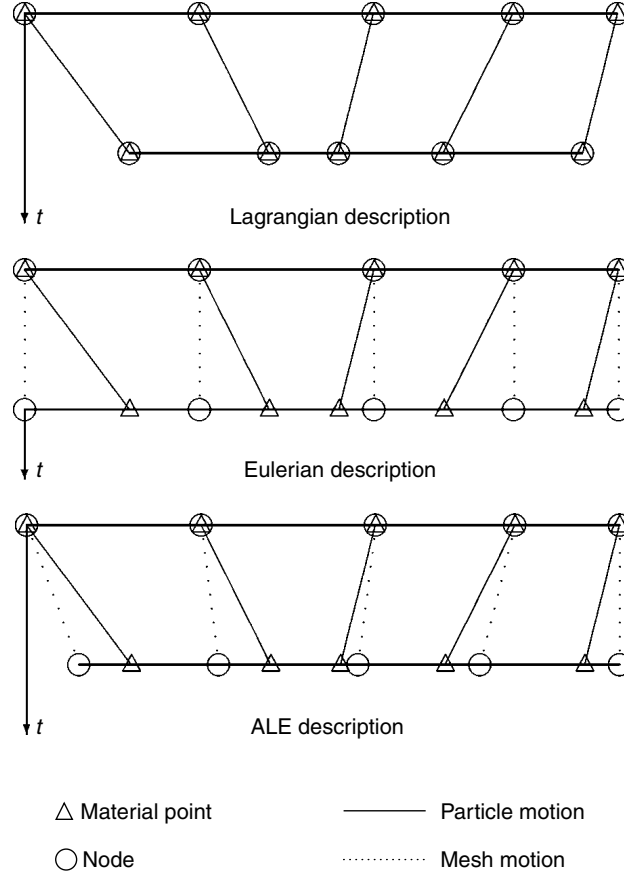


Figure 4.1: One-dimensional example of Lagrangian, Eulerian and ALE mesh and particle motion (Hirt, Amsden, and Cook 1974).

spatial gradients are computed in respect to the stationary frame. The convective velocity  $\mathbf{v} - \mathbf{u}_g$ , where  $\mathbf{u}_g$  represents mesh velocity, replaces the flow velocity  $\mathbf{v}$ , which appears in the convective term of Eulerian formulations (Donea et al. 2004).

$$\frac{\partial}{\partial t} \int_{\Omega} \rho d\Omega + \int_S \rho (\mathbf{v} - \mathbf{u}_g) \cdot \mathbf{n} dS = 0 \quad (4.1)$$

$$\frac{\partial}{\partial t} \int_{\Omega} \rho \mathbf{v} d\Omega + \int_S \rho (\mathbf{v} - \mathbf{u}_g) \mathbf{v} \cdot \mathbf{n} dS + \int_S p \bar{\mathbf{I}} \cdot \mathbf{n} dS - \int_S \bar{\tau}_\nu \cdot \mathbf{n} dS = \int_{\Omega} \rho \mathbf{f}_b d\Omega \quad (4.2)$$

$$\frac{\partial}{\partial t} \int_{\Omega} E d\Omega + \int_S (E + p) (\mathbf{v} - \mathbf{u}_g) \cdot \mathbf{n} dS - \int_S (\bar{\tau}_\nu \cdot \mathbf{v}) \cdot \mathbf{n} dS + \int_S \dot{\mathbf{q}} \cdot \mathbf{n} dS = \int_{\Omega} \rho (\mathbf{f}_b \cdot \mathbf{v} + \dot{\xi}) d\Omega \quad (4.3)$$

In the foregoing equations,  $\Omega$  and  $S$  are the volume and boundary surfaces of a moving control volume, respectively. It is very important to note that the integral form for the Lagrangian and Eulerian mesh descriptions are contained in the above ALE forms. In

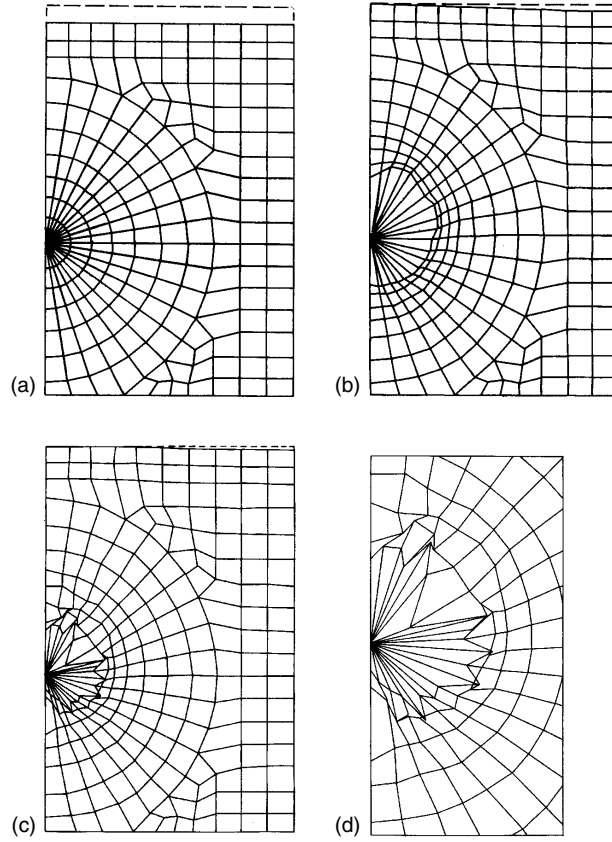


Figure 4.2: Lagrangian versus ALE descriptions: (a) initial FE mesh; (b) ALE mesh at  $t = 1$  ms; (c) Lagrangian mesh at  $t = 1$  ms; (d) details of interface in Lagrangian description (Hirt, Amsden, and Cook 1974).

fact, for  $u_g = 0$  the equations are written in Eulerian description, while the Lagrangian description corresponds to selecting  $\mathbf{u}_g = \mathbf{v}$ . For a mesh rigid motion, volume and surfaces of each cells are constant in time, but for deforming grid,  $\Omega = \Omega(t)$ , volume is determined using the geometric conservation law:

$$\frac{dV}{dt} = \int_S \mathbf{u}_g \cdot d\mathbf{S} \quad (4.4)$$

It is possible to identify three levels of ALE:

- Steady ALE - used to simulate flows on non-moving grids, for example in a rotating frame.
- Moving grids - this approach is typically used for the calculation of the aerodynamic derivatives. It is used to simulate a flow on moving grids but grid deformation does not take place,  $dV/dt = 0$ .
- Deforming grids - cells are deformed and adapted to the physical system. It is indicated for simulate fluid-structural interactions.

In CFD codes this technique requires further procedures to take into account the temporal movement/deformation of the grid. For further details refer to Hirt, Amsden, and Cook 1974.

## 4.2 Chimera Technique

The Chimera method was developed by Benek et al. 1986 as a meshing simplification in alternative to unstructured grids. The main idea is to decompose a complex geometrical domain into simpler and overlapping subdomains. Each of these is generated independently and then coupled by means a coupling strategy in order to obtain a global solution and provide a natural level of parallelism for execution on massively parallel computers (Tang, Jones, and Sotiropoulos 2003).

Summarizing the technique allows to (Houzeaux et al. 2014):

- simplify mesh generation - handle complex geometries, generating different meshes around the components of the computational domain in an independent way.
- execute local refinement - when more accuracy is required in some specific computational domain parts, local refinement can be achieved by putting a refined patch mesh into the original mesh.
- handle moving components - treat problems where components are moving without having to re-mesh the whole computational domain. The independent meshes are moved as rigid bodies and the solution is recoupled when suited.

Generally the mesh is divided into a background mesh, which covers all the computational domain, and patch meshes attached to the different components which are located upon the background mesh. The governing equations are solved independently in each subdomain and to obtain continuous solution the informations are transferred from one subdomain to another via interfaces.

The implementation of boundary conditions for all flow variables at interfaces (especially in complex, unsteady flows) is the weak point of overset grid algorithms (Tang, Jones, and Sotiropoulos 2003). In complex, unsteady flow simulations such boundary conditions should ensure that vortical structures generated in one subdomain can cross interfaces and interact with the flow in adjacent subdomains without distortions. The original Chimera technique developed by Benek, accomplishes this exchange using a linear-interpolation of all primitive variables. This approach, however, does not guarantee that the obtained numerical solution will be globally conservative. The term globally conservative implies that the fluxes of conserved quantities (mass, momentum and energy) integrated over the boundary of the composite domain add up to zero. Lack of global conservation could be detrimental to the accuracy and smoothness of the computed solution, especially in incompressible flow simulations where global mass conservation is a necessary condition for the existence and uniqueness of a smooth pressure field.

### 4.2.1 Fluent: Overset Mesh

In Fluent code this technique is called overset mesh and it is useful to report how the chimera technique is implemented to highlight also the requirements to be met in the

generation of the mesh (*Ansys Fluent User and Theory's Guide 2018*). Figure 4.3 shows a simplified mesh for a flow over a cylinder in a duct. The mesh consists of two parts: a *background mesh* representing the duct and a separate component mesh around the cylinder. The case is set up specifying the outer boundary of the cylinder mesh as *overset boundary*, and creating an *overset interface*.

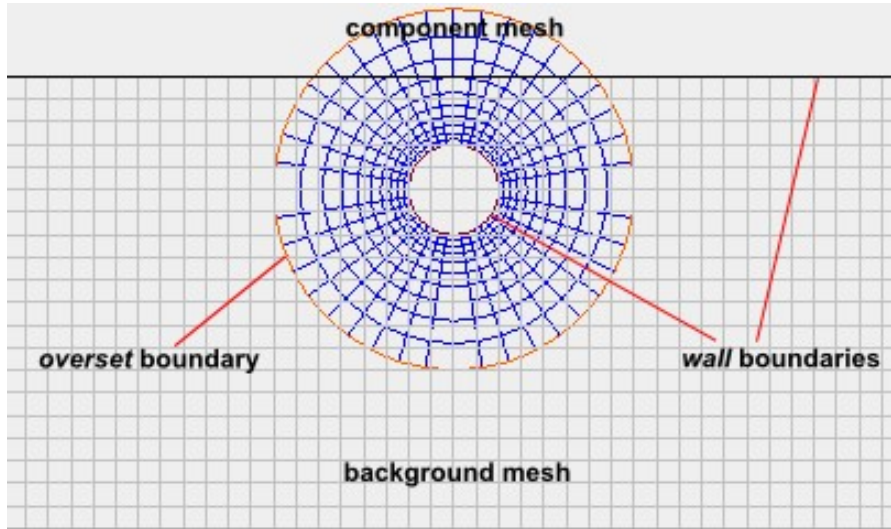


Figure 4.3: Overset case set-up (*Ansys Fluent User and Theory's Guide 2018*).

Thus Fluent automatically establishes the necessary connectivity between the meshes. In this process the cells are classified as *dead cells* those that fall outside the domain and *solve cells* those where the flow equations are solved. To these are added two other types of cells: *receptor cells* and *donor cells*. Receptor cells receive data interpolated from another mesh, while the donor cells are those from which the first ones get their data. When an overset interface is initialized, there are three main steps that Fluent completes to establish connectivity between the participating zones:

- hole cutting;
- overlap minimization;
- donor search;

Hole cutting is the process by which cells lying outside of the flow region are marked as *dead cells*. This is achieved by marking all the cells that are cut by physical boundary zones (wall, inlet, outlet, symmetry, and so on). The result of this operation is a valid overset mesh with maximum mesh overlap.

The maximum overlap mesh shown in figure 4.4 is a valid overset mesh, however, it may not be ideal. A large overlap between component and background meshes is computationally inefficient since the equations are solved in more cells than are necessary. Additionally, the cell sizes of the overlapping meshes may vary greatly, this affects the data interpolation and is detrimental to solution quality. Ideally meshes should transition in regions of similar resolution.

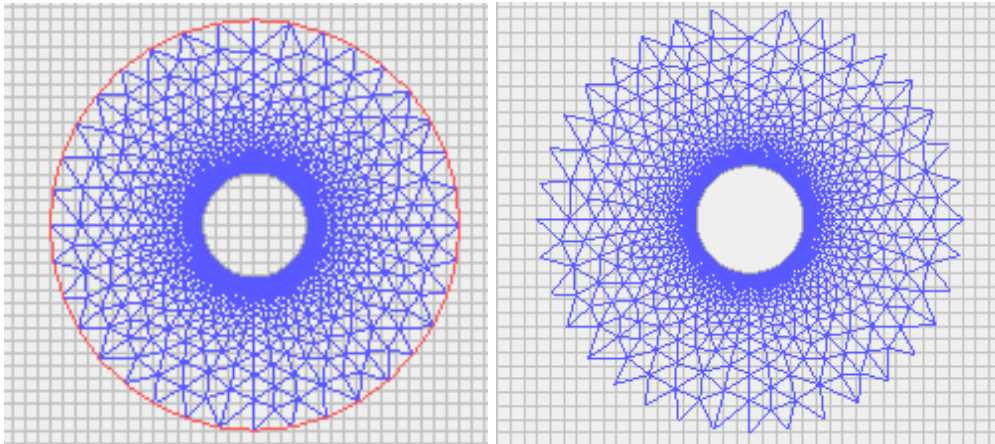


Figure 4.4: Overset mesh before and after hole cutting (*Ansys Fluent User and Theory's Guide 2018*).

Here comes into play overlap minimization. It is used to minimize mesh overlap among different component and background meshes by converting additional solve cells into receptor cells and turning unnecessary receptors into dead cells. During this process, a solve cell is turned into a receptor cell if the cell can find a suitable donor cell with higher donor priority. In mesh overlap areas, without additional user input, the solver attempts to obtain the solution on the finest local mesh. The resulting mesh interface moves to an area where the meshes are more comparable in cell size, leading to better solution quality.

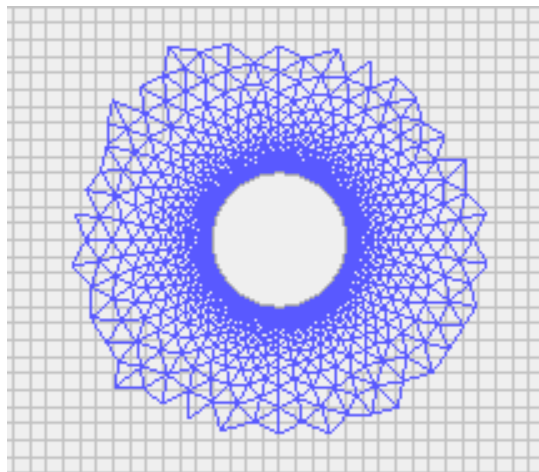


Figure 4.5: Figure shows the cylinder case after the overlap minimization step (*Ansys Fluent User and Theory's Guide 2018*).

Also note that with overlap minimization, data interpolation between cell zones does not necessarily occur at the overset boundaries. The purpose of specifying an overset boundary is primarily to specify that overset mesh coupling should happen, and not where it should occur.

The donor search is the final step in establishing the domain connectivity. Fluent searches other meshes for valid solve cells for each receptor. The solve cell containing the cell centroid of the receptor cell, along with its connected solve cells, are used as donor candidates for a given receptor. Each receptor must have at least one valid donor cell. There must be four or more cells in the overlap of both meshes to ensure a successful donor search. The receptor cells, which form the fringe layer of a mesh zone, must overlap sufficiently with the opposite mesh, such that they find valid solve cells as donors. For an example of valid mesh overlap.

## 4.3 Numerical set-up

In general partial differential equations such as Navier-Stokes equations requires the definition of initial conditions and all specific conditions on the boundaries of the domain. In this way the problem is defined well-posed and the algorithm is able to start iteration. Moreover, to set-up a calculation using finite element method for Navier-Stokes equations gas behaviour, turbulence model, resolution scheme and discretization order have to be set.

### 4.3.1 Boundary conditions

Although the sequence of setting is different between one software and another, the boundary conditions are the same. In cases under study, three boundary conditions are utilized and they are symmetry, wall and far-field conditions:

- symmetry boundary conditions are used when the physical geometry of interest, and the expected pattern of the flow/thermal solution, have mirror symmetry. In every case, the symmetry plane is recognized as an inviscid tangency (Slip Wall), where the normal velocity in the ghost cells is a reflection of the velocity in the interior cell.
- solid wall boundary conditions are used to bound fluid and solid regions. It imposes the tangency condition to the flow.
- far-field conditions are used to model a free-stream condition at infinity. it uses characteristic information (Riemann invariants) to determine the flow variables at the boundaries. To set correctly this boundary condition the following information are necessary: static pressure, Mach number, temperature, flow direction, turbulence parameters.

The table 4.1 shows what parameters are assigned for each boundary type.

### 4.3.2 Gas Model

Ideal gas law has been used to connect pressure, density and temperature of the air. For compressible flows, the it is written in the following form:

$$\rho = \frac{p_{op} + p}{\frac{R}{M_w} T} \quad (4.5)$$

<b>Body's Wall</b> {Wall}	
Wall Motion	-
Thermal Conditions	-
<b>Free-Stream</b> {Pressure far-field}	
Static Pressure (Pa)	-
Free-Stream Mach number	-
x-component of flow Direction	-
y-component of flow Direction	-
z-component of flow Direction	-
Temperature (K)	-
Turbulent Intensity (%)	-
Turbulent Viscosity Ratio	-
<b>Symmetry Plane</b> {Symmetry}	
-	-

Table 4.1: Summarizing table for each boundary type.

where  $p_{op}$  is the operating pressure (set to 0 Pa),  $p$  is the local static pressure relative to the operating pressure,  $R$  is the universal gas constant, and  $M_w$  is the molecular weight. The temperature,  $T$ , is computed from the energy equation.

Moreover, Sutherland law has been set to get the gas dynamic viscosity coefficient from temperature value.

$$\mu = \mu_0 \left( \frac{T}{T_0} \right)^{3/2} \frac{T_0 S}{T + S} \quad (4.6)$$

For air  $T$  is the static temperature,  $\mu_0 = 1.716 \cdot 10^{-5} \text{ Kg/m s}$ ,  $T_0 = 273.11 \text{ K}$  and  $S = 110.56 \text{ K}$ .

### 4.3.3 Turbulence Models

In this section are shown the type of N-S equations and three turbulence models used in this thesis.

The study of a turbulent flow can be conducted in two ways. The first is the direct one, in which the equations of motion are studied in all their details called direct simulations. The second is the mediated one, in which new sizes are apparently defined, simpler than the original ones, and in terms of which the new evolutionary equations are written (Germano 2010).

Since the direct study of the N-S equations requires enormous computing power, thus to resolve the flow evolution, *Reynolds Averaging Navier-Stokes (RANS)* have been used. According to Reynolds, in a stationary turbulence flow each of the instantaneous dependent variables in the N-S equations can be decomposed into a time-average and a fluctuating component:

$$f(\mathbf{x}, t) = \bar{f}(\mathbf{x}) + f'(\mathbf{x}, t) \quad (4.7)$$

$$\bar{f}(\mathbf{x}) = \frac{1}{T} \int_{t_0}^{t_0+T} f(\mathbf{x}, t) dt \quad (4.8)$$

where  $\bar{f}$  is the time-averaged component and  $f'$  is the fluctuating one. For the sake of simplicity considering the incompressible N-S equations:

$$\frac{\partial u_i}{\partial t} = 0 \quad (4.9)$$

$$\rho \frac{\partial u_i}{\partial t} + \rho u_j \frac{\partial u_i}{\partial x_j} = -\frac{\partial p}{\partial x_j} + \mu \frac{\partial^2 u_i}{\partial x_j^2} \quad (4.10)$$

Substituting into these equations the flow variables seen above and averaging over time, the Reynolds Averaged Navier-Stokes (RANS) equations are obtained:

$$\frac{\partial \bar{u}_i}{\partial t} = 0 \quad (4.11)$$

$$\rho \frac{\partial \bar{u}_i}{\partial t} + \rho u_j \frac{\partial \bar{u}_i}{\partial x_j} = -\frac{\partial p}{\partial x_j} + \mu \frac{\partial^2 \bar{u}_i}{\partial x_j^2} - \frac{\partial}{\partial x_j} \overline{\rho u'_i u'_j} \quad (4.12)$$

They have the same general form as the instantaneous Navier-Stokes equations, with the velocities and other flow variables represented in time-averaged form. The only difference is the additional called Reynolds stresses that account the effects of turbulent fluctuations on mean flow. The Reynolds stress tensor, represents the mean flux of momentum in i-direction due to turbulent fluctuations in j-direction.

The media process has left the number of equations unaltered, but has increased the number of unknowns variable. The problem of solving these equations is the so-called *problem of closure*, where for closure it means the formulation of a turbulence model that expresses Reynolds' efforts in relation to average values (Germano 2010).

A common method to write the Reynolds tensor employs the Boussinesq hypothesis that permits to relate the Reynolds stresses to the mean velocity gradients.

$$-\overline{\rho u'_i u'_j} = 2\mu_t \bar{s}_{ij} - \frac{2}{3} \partial x_k + \rho k \delta_{ij} \quad (4.13)$$

where  $\bar{s}_{ij}$  is the mean rate-of-strain tensor:

$$\bar{s}_{ij} = \frac{1}{2} \left( \frac{\partial \bar{u}_i}{\partial x_j} + \frac{\partial \bar{u}_j}{\partial x_i} - \frac{2}{3} \delta_{ij} \frac{\partial \bar{u}_k}{\partial x_k} \right) \quad (4.14)$$

This hypothesis places in analogy the turbulent agitation with the thermal one, where for analogy the speed of thermal stirring is substituted by a velocity of macro-scale, or turbulent stirring speed  $v_t$ , and the free collisional mean path by a macro-scale length, or mixing length  $l_t$ . Respect to complete Navier-Stokes the mediated equations have the same structure but the viscosity is increased by a turbulent viscosity  $\mu_t$  given by:

$$\mu_t \simeq \rho v_t l_t \quad (4.15)$$

and it is clear that the problem is now how determining  $v_t$  and  $l_t$ .

The Boussinesq hypothesis is used in the  $k - \varepsilon$  models, and the  $k - \omega$  models. The advantage of this approach is the relatively low computational cost associated with the computation of the turbulent viscosity,  $\mu_t$ . For  $k - \varepsilon$  and  $k - \omega$  models, two additional transport equations are solved and  $\mu_t$  is computed as a function of  $k$  and  $\varepsilon$  or  $k$  and  $\omega$ . The disadvantage of the Boussinesq hypothesis is that it assumes  $\mu_t$  as isotropic scalar quantity, which is not strictly true.

$k - \varepsilon$

The turbulent viscosity models use two transport equations for the determination of turbulent length and time scale from which turbulent viscosity depends. The semi-empirical standard  $k - \varepsilon$  model is based on model transport equations for the turbulence kinetic energy ( $k$ ) and its dissipation rate ( $\varepsilon$ ). The model transport equation for the turbulence kinetic energy is derived from its differential equation, while the model transport equation for turbulence dissipation rate is obtained using physical reasoning and bears little resemblance to its mathematically exact counterpart. Their resolution allow to obtain  $k$  and  $\varepsilon$ . Directly from the definition of turbulent kinetic energy is possible to extract the macro-scale velocity while thanks to the Taylor study on turbulence is possible to estimate the mixing scale by mean of turbulence dissipation  $\varepsilon$ :

$$v_t \simeq k^{1/2} \quad (4.16)$$

$$l_t \simeq \frac{k^{3/2}}{\varepsilon} \quad (4.17)$$

The turbulent viscosity,  $\mu_t$ , is computed by combining  $k$  and  $\varepsilon$  as follows:

$$\mu_t = \rho C_\mu \frac{k^2}{\varepsilon} \quad (4.18)$$

where  $C_\mu = 0.09$ .

One improved version of the standard  $k - \varepsilon$  model is known as the *realizable*  $k - \varepsilon$  model. It attempts to correct two deficiencies of standard  $k - \varepsilon$  model. First, when strain rates are large, the standard  $k - \varepsilon$  model can produce non-physical normal and shear stresses. This is addressed using a new eddy-viscosity formula involving a  $C_\mu$  variable. Second, the standard  $k - \varepsilon$  model utilizes an empirical transport equation for turbulence dissipation that is believed to be the cause of poor spreading rate predictions for laminar jets. The realizable  $k - \varepsilon$  model replaces the empirical  $\varepsilon$  equation with a modified transport equation, derived from an exact equation for the transport of the mean-square vorticity fluctuation (*Ansys Fluent User and Theory's Guide 2018*).

The realizable model have shown substantial improvements over the standard - model where the flow features include strong streamline curvature, vortices, and rotation.

One limitation of the *realizable*  $k - \varepsilon$  model is that it produces non-physical turbulent viscosities in situations where the computational domain contains both rotating and stationary fluid zones. This is due to the fact that model includes the effects of mean rotation in the definition of the turbulent viscosity. This extra rotation effect has been tested on single moving reference frame systems and showed superior behaviour over the standard model.

However, due to the nature of this modification, its application to multiple reference frame systems should be taken with some caution (*Ansys Fluent User and Theory's Guide 2018*).

$k - \omega$

The standard  $k - \omega$  model is based on the Wilcox  $k - \omega$  model, which incorporates modifications for low-Reynolds number effects, compressibility, and shear flow spreading. The standard model is an empirical model based on model transport equations for the turbulence kinetic energy ( $k$ ) and the specific dissipation rate ( $\omega$ ). Main weak of the Wilcox model is the sensitivity of the solution to the free-stream boundary condition.

The *shear stress transport* (SST) formulation combines the best of Wilcox  $k - \omega$  and  $k - \varepsilon$  turbulence model. The use of a  $k - \omega$  formulation in the inner parts of the boundary layer makes the model directly usable all the way down to the wall through the viscous sub-layer. The SST formulation switches to a  $k - \varepsilon$  behaviour in the free-stream and thereby avoids the common  $k - \omega$  problem that the model is too sensitive to the free-stream turbulence properties.

Authors who use the SST  $k - \omega$  model often merit it for its good behaviour in adverse pressure gradients and separating flow.

The proper transport behaviour is obtained by a limiter to the formulation of the eddy-viscosity:

$$\nu_t = \frac{a_1 k}{\max(\alpha_1 \omega, SF_2)} \quad (4.19)$$

where  $\Omega$  is the vorticity modulus,  $\alpha_1$  is a constant and  $F_2 = 1$  vale 1 in the inner of boundary layer and decreases moving away from the wall and In the boundary layer  $\Omega > a_1 k$  (*Ansys Fluent User and Theory's Guide 2018*).

#### 4.3.4 Resolution Scheme

The pressure-based coupled flow solver has been used to solve the N-S equations. In this resolution scheme velocity field is obtained from the momentum equations, while the pressure field is extracted by solving a pressure correction equation which is obtained by manipulating continuity and momentum equations. The pressure equation is derived in such a way that the velocity field, corrected by the pressure, satisfies the continuity (*Ansys Fluent User and Theory's Guide 2018*). This method was originally developed for incompressible flows, where strictly  $\nabla \cdot \mathbf{V} = 0$ , then and it has been extended to solve compressible flows modifying the pressure correction equation to include density effects on pressure.

Unlike the segregated algorithm, coupled algorithm solves at the same time momentum equations and the pressure-based continuity equation. The remaining scalars equations are solved in a decoupled fashion as in the segregated algorithm. Removing the approximations due to isolating, coupled approach allows to find an unique solution that respects both the continuity and momentum equation which improves significantly the rate of solution convergence.

An overview of the two pressure-based solution methods is showed in Figure 4.6.

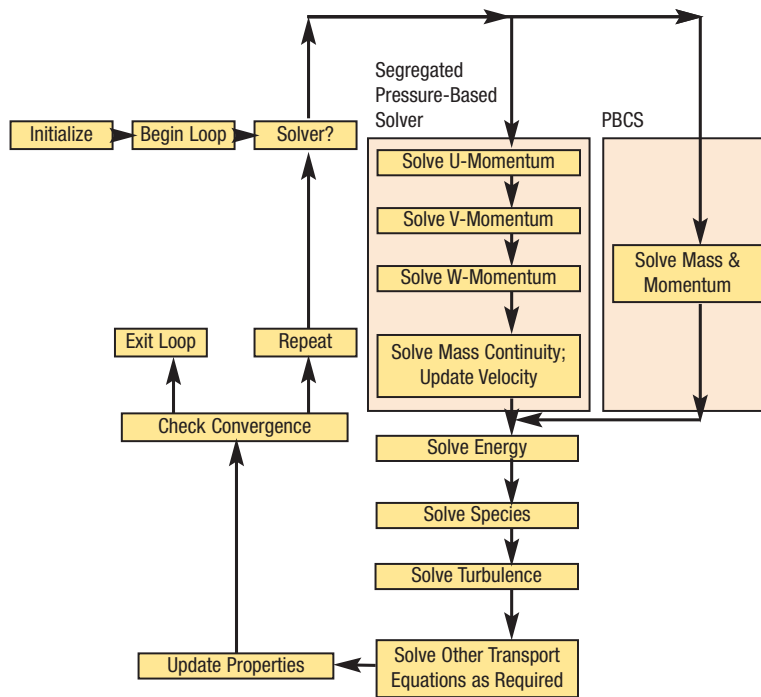


Figure 4.6: Flowchart illustrating solver algorithms (Franklyn 2008).

# Chapter 5

## Hayabusa: Numerical Analysis

This chapter discusses the procedure followed to obtain results of Hayabusa capsule using two 3D solvers, Fluent and CFD++, starting from mesh generation up to set-up simulation. Finally, the main results of the 3D calculations are presented and the two solvers solutions are compared to each other.

Simulations are performed with the use of different software in order to create capsule geometry, calculation domain and mesh generation. The first step has been the creation of the 3D geometry file for the capsule and flow domain around with the aid of Ansys SpaceClaim. The second step has been the generation of the mesh suitable for the fluid domain using Ansys Meshing and the third step has been the actual numerical simulation procedure and solution acquirement. The final step has been the post processing of the solution files.

### 5.1 Pre-Processing

Two codes require two different set-ups. As seen, a moving grid approach is recommended for aerodynamic derivatives calculation, but this implementation in Fluent produces numerical error which spread inside computational domain from boundary. This problem has been bypassed using Chimera Technique. Two fluid volumes have been created: a moving volume including body walls and one another fixed in time for the rest of fluid volume. In CFD++ this problem has not been revealed, so a unique mesh has been created.

#### 5.1.1 Basic Assumptions

It is useful to introduce some considerations to frame the type of simulations:

- centre of gravity is fixed and the aerodynamic moment is calculated respect to it;
- only pitching moment is measured, considering side-slip angle equals to  $0^\circ$ ;
- analyses have been conducted at different angles of attach [ $0^\circ, 10^\circ, 20^\circ$ ].
- taking advantage of body axial-symmetry only a half volume is taking account; in post processing all aerodynamic forces and moments have been corrected;

- flow regime is subsonic and fully turbulent;
- there is not heat-exchange between fluid and body wall;
- no gravitational effects have been considered;
- Reynolds number of  $1.04 \cdot 10^6$  has been considered;
- this work section is a continuation of Ravera Chiara's thesis (Ravera and D'Ambrosio 2018), so the same flight conditions are used in order to start from the same point. The ambient conditions are: pressure of  $19212 Pa$ , temperature of  $220K$  and a Mach number of  $0.381$ .

### 5.1.2 Mesh Generation

Ansys Meshing is a mesh-generation software which provides an easy mesh generation algorithm. Generally, the input required is the geometry of the fluid domain; this is obtained starting from a box and executing a subtract operation with capsule CAD model.

The use of Chimera technique in Fluent imposes the building of two domains. The first is a simple box which constitutes the fixed fluid domain, while the second is a semi-sphere upon which is performed the subtract operation with capsule CAD 2.6 and it constitutes the moving fluid domain. The whole CAD origin axis is placed in correspondence of Hayabusa centre of gravity. In this way the position of gravity and rotation centre can be easily localized.

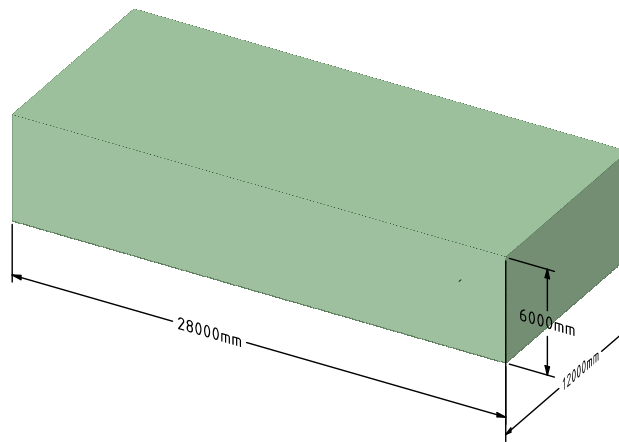


Figure 5.1: Size and shape of the fixed domain.

Maximum domain dimension has been chosen large enough for subsonic conditions to avoid pressure waves reflections on boundary which could affect the computation of aerodynamic coefficient. Instead moving volume size has been defined in order to avoid large gradient falling into overlap region.

Generated mesh is hybrid, composed by combination of different elements: tetrahedra and prism. Capsule and box surface mesh are reproduced in figures 5.3, its minimum size is a trade-off between computational cost and capacity of the mesh to reproduce correctly the body shape.

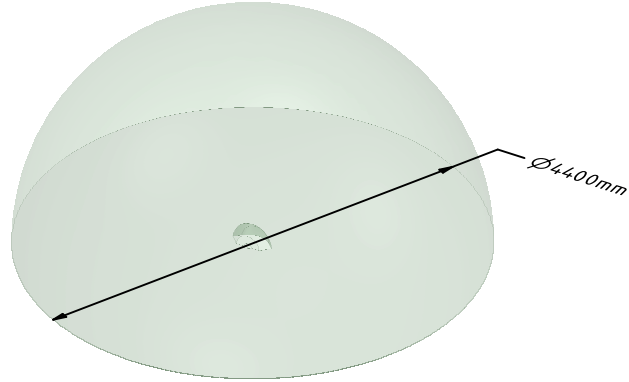


Figure 5.2: Size and shape of the moving domain.

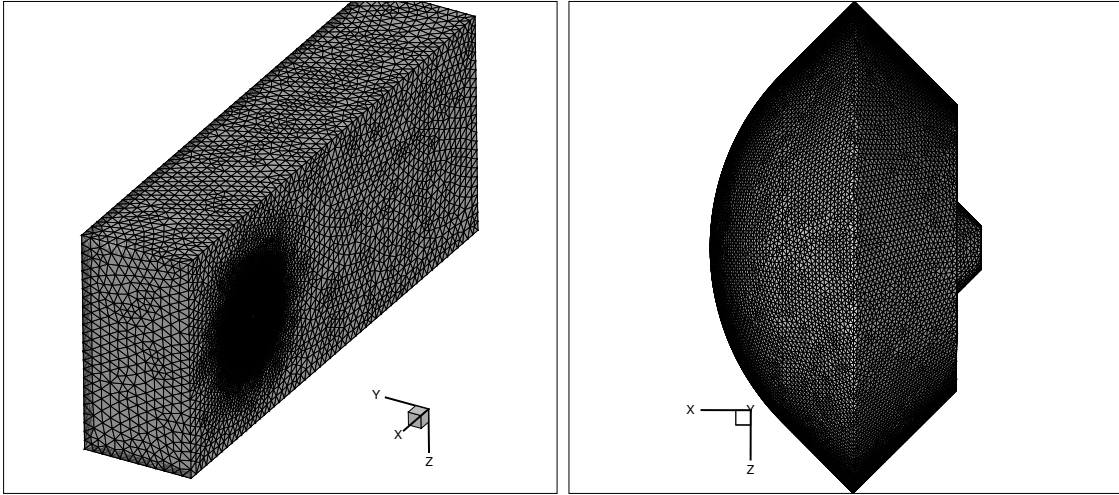


Figure 5.3: View of the domain and capsule mesh.

As shown in figure 5.4, some volume size controls are used to optimize the cells density around body and into wake region where high turbulent flow is aspected to develop. These refinement areas are important to improve domain resolution and thus solution accuracy. Moreover it is possible to notice the zone where is performed the overlap. In figures 5.4 is shown where the overset has been adopted. In the first figure notice the cells which come into play for the transmission of primitives through the two grids. In the second figure a contour scene of mass imbalance is represented and it is possible to see high values of residual concentrated close up the overset boundary due to Chimera technique.

A last look is reserved to prism layers generation. These are located around the body in order to capture the boundary layer. The first cell height requires a particular attention. It must have a precise height to capture the viscous sublayer; it can be estimated using the definition of  $y^+$  and flat-plate boundary layer theory:

$$y^+ = \frac{\rho u_\tau \Delta y}{\mu} \Rightarrow \Delta y = \frac{y^+ \mu}{\rho u_\tau} \quad (5.1)$$

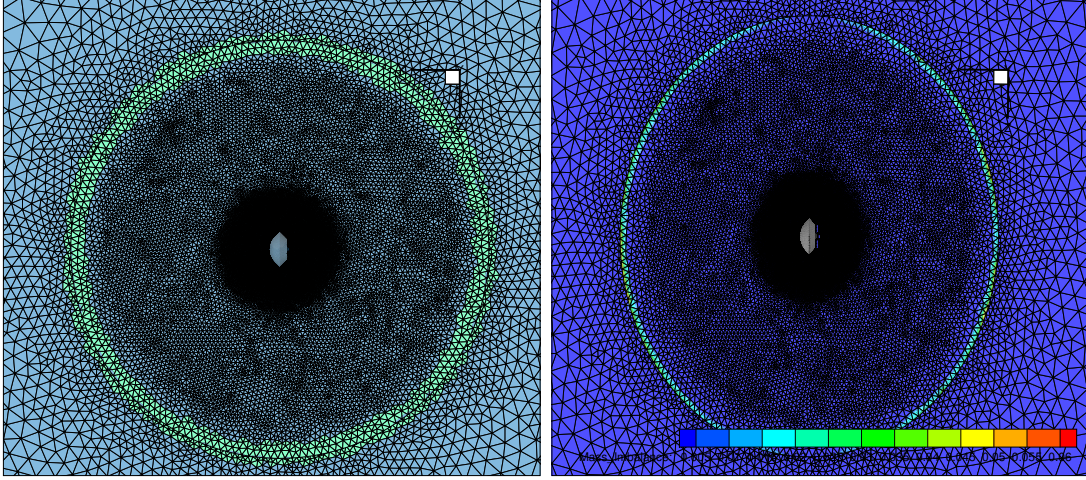


Figure 5.4: On the left the cells affected by the overset are highlighted, while on the right we can see the region where the continuity residual is high.

where  $u_\tau$  is friction velocity,  $y^+$  is the distance from the wall ( $\Delta y$ ) normalized by the viscous length-scale. The definition of friction velocity allows to correlate it with wall shear stress ( $\tau_w$ ):

$$u_\tau = \sqrt{\frac{\tau_{wall}}{\rho}} \quad (5.2)$$

$$\tau_{wall} = \frac{C_f \rho U_\infty^2}{2} \quad (5.3)$$

Utilizing the skin friction coefficient of a flat-plate in high turbulent regime flow it is possible find a correlation with Reynolds' number:

$$C_f = \frac{0.026}{Re_x^{1/7}} \quad (5.4)$$

$$Re_x = \frac{\rho U_\infty L_{ref}}{\mu} \quad (5.5)$$

Following this procedure, the first cell height of  $1 \cdot 10^{-5} m$  has been chosen to obtain a  $y^+ = 1$  near wall with the parameters in possession and as it is possible to see in figure 5.5 it has been set correctly.

Everything discussed above also applies to mesh generated for CFD++ solver, with the difference that only one volume is required.

It is not possible to know a priori which is the trade-off between resolution and accuracy, so a mesh convergence study has been performed.

### 5.1.3 Mesh Convergence Study

Mesh convergence study is based on the fundamental principle that with increase in grids fineness, the spatial discretization errors will asymptotically approach to zero and thereby

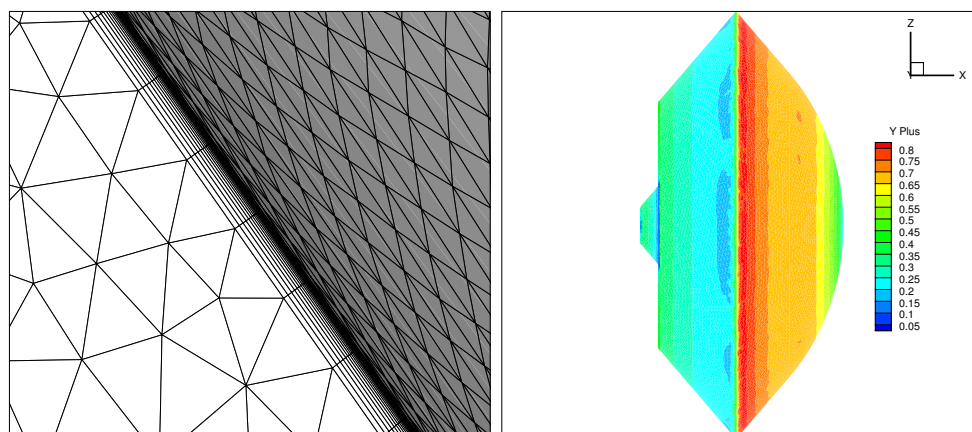


Figure 5.5: On the left an image of the prism layers at the wall and on the right the values of  $y^+$  on the capsule.

helping to achieve a solution independent from grid resolution. When this happens any further refinement does not improve the solution.

Thus convergence study is performed putting to test different grids starting from a low cells number and then increasing resolution. This procedure requires an orderly variation in spatial resolution in every corners of the domain. It is not a random refinement in the fluid domain.

This process can be monitored seeing residuals and the value of moments and forces. Taking into account a steady state simulation, a double check is necessary in order to consider convergent solution: residuals value and a problem characteristic magnitude, such as aerodynamic forces/moments, flow rate, heat exchange etc... A solution is considered convergent when the first is low and the second has a variation lower than its mean value. When two consecutive grids have convergent solution with a very small deviation the mesh with less cells number is taken.

In this specific case, axial force, normal force and pitching moment have been under examination. A zero angle of attack has been set thus normal force and pitching moment are expected to be equal to zero. In the table 5.1, results for three mesh with 5, 6 and 8 millions cells are reported.

N. of cells	Axial Force [N]	Normal Force [N]	Pitching Moment [Nm]	$\Delta$ A.F. [N]	$\Delta$ N.F. [N]	$\Delta$ P.M. [Nm]
5M	-182,40	4,760	0,6980	6,80	4,83	0,70
6M	-189,16	-0,013	0,0040	0,04	0,05	0,00
8M	-189,20	-0,068	0,0009	0,00	0,00	0,00

Table 5.1: Results of the convergence test with various numbers of cells.

The simulation with 5 millions cells mesh shows a good residuals value, but there are significant differences in forces and moments compared to 8 millions cells one. Although residuals reach a value close enough to that reached by the other two mesh, it shows that a

double number of iterations is required. Switching to the other two meshes, parameters are substantially in line, suggesting that the 6 millions cells mesh is a good compromise. Notice that the value of normal force is never equal to zero and that for more dense mesh case its value get away from zero. This is a consequence of the use of unstructured mesh since it is not perfectly symmetrical.

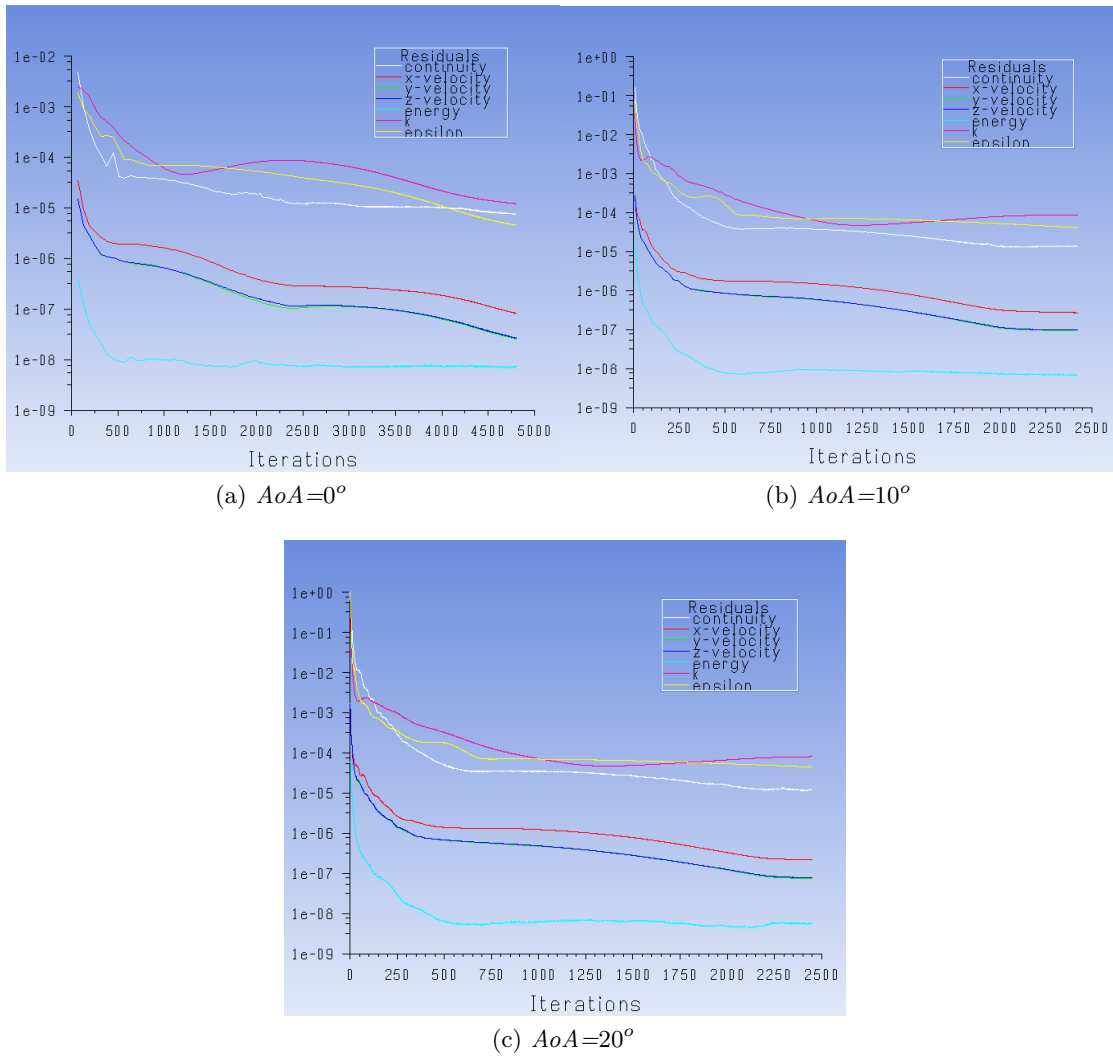


Figure 5.6: Graph of the residuals as a function of the number of iterations for each of the convergence tests.

## 5.2 Numerical Set-up

Three boundary conditions are utilized: symmetry, wall and pressure far-field conditions. As shown in figure 5.7 the walls of the domain have been divided and grouped into sub-groups on which the same boundary condition type is imposed. For each of sub-groups, a boundary condition type and characteristic parameters are reported in table 5.2.



Figure 5.7: Boundary groups.

### Capsule Wall {Wall}

Wall Motion	Stationary Wall
Thermal Conditions	adiabatic

### Pressure far-field {Pressure far-field}

Static Pressure (Pa)	19212.6
Free-Stream Mach number	0.381
x-component of flow Direction	$-\cos \alpha$
y-component of flow Direction	0
z-component of flow Direction	$-\sin \alpha$
Temperature (K)	220
Turbulent Intensity (%)	5
Turbulent Viscosity Ratio	10

### Symmetry Plane {Symmetry}

-

-

Table 5.2: Parameters set for each boundary.

Recalling what has been shown in section 4.3, the table 5.3 reports models and numerical

schemes used in the CFD simulations. A different combination of discretization scheme have been used in Fluent and CFD++. For the last a second upwind scheme has been used for spatial and temporal discretization. Instead the use of Chimera technique and moving mesh does not allow to use a second order in time for Fluent. Regarding spatial discretization upwind scheme has been used except for  $\epsilon$  equation because forcing a second order it has been seen numerical instability in the zone of high turbulent flow.

## 5.3 Fluent Simulations

In the following section, the results for the Fluent simulations are presented for three angles of attack:  $0^\circ$ ,  $10^\circ$ ,  $20^\circ$ . Dynamic analysis have to conducted in transient tests in order to calculate pitching moment coefficient time-history. Two strategies can be followed: running the entire test with a transient simulation or starting from a steady state solution. The last approach has been used in this work. It is used to reach a motion field advanced reducing significantly the physical time of the transitory phase, the time between the beginning of the oscillations and the achievement of the limit cycle.

### 5.3.1 Steady State Tests

AoA [deg]	CFD Data			Database		
	$C_A$	$C_N$	$C_m$	$C_A$	$C_N$	$C_m$
0	0.833	0.000	0.000	0.88	0.00	0.000
10	0.811	0.076	-0.024	0.88	0.06	-0.022
20	0.735	0.146	-0.050	0.83	0.16	-0.044

Table 5.4: Fluent steady state tests results.

In the table 5.4 are reported the aerodynamic coefficients calculated from Fluent solutions and the corresponding values shown on database. The result that stands out to the eye is the quite substantial error that exists between  $C_A$  values, while for  $C_N$  and  $C_m$  this error is reduced.

### 5.3.2 Transient Tests

To pursue the goal, transient simulation has been activated. As explain in section 3.2 the simple rotation implies a variation of both angle of attack and pitching, so this test type is not sufficient to derive individual aerodynamic derivatives. For this reason a second test is necessary, in which the pitching angle is kept constant and the angle of incidence varies. From this test derivatives relative to the angle of incidence are obtained and joined to the results of the previous test derivative relative to pitch angle are obtained. To implement the second approach, an oscillation along the z-axis is required, and the motion is called the *plunging*.

For each of three angles of attach, motion and transient test parameters have been set as is shown in the table 5.5:

<b>Numerical Set-Up For Fluent</b>	
Gas model	Compressible Ideal Gas
Viscous model	Sutherland Law
N-S equations	RANS
Turbulence Model	$k - \varepsilon$ standard
Resolution Algorithm	Coupled Pressure-Based
Numerical Scheme	Upwind
- Pressure	2 <sup>nd</sup> Order
- Density	2 <sup>nd</sup> Order
- Momentum	2 <sup>nd</sup> Order
- Turbulent $k$	2 <sup>nd</sup> Order
- Turbulent $\varepsilon$	1 <sup>st</sup> Order
- Energy	2 <sup>nd</sup> Order
Transient Configuration	
Numerical Scheme	1 <sup>st</sup> Implicit Order
Inner iteration	50/100
<b>Numerical Set-Up for CFD++</b>	
Gas model	Compressible Ideal Gas
Viscous model	Sutherland Law
N-S equations	RANS
Turbulence Model	$k - \varepsilon$ realizable
Resolution Algorithm	Coupled Pressure-Based
Numerical Scheme	Upwind
- Pressure	2 <sup>nd</sup> Order
- Density	2 <sup>nd</sup> Order
- Momentum	2 <sup>nd</sup> Order
- Turbulent $k$	2 <sup>nd</sup> Order
- Turbulent $\varepsilon$	2 <sup>nd</sup> Order
- Energy	2 <sup>nd</sup> Order
Transient Configuration	
Numerical Scheme	2 <sup>nd</sup> Implicit Order
Inner iteration	50

Table 5.3: Models and algorithms set.

In figures 5.8, 5.9, 5.10, 5.11, 5.12, 5.13 pitching moment variation as function of  $z/\Delta\alpha$  and time is displayed. Note that in all the tests the oscillations reach limit cycle very quickly after about a period.

Plunging motion		Pitching motion	
Motion	$z = z_o \cos(\omega t)$	Motion	$\Delta\alpha = \alpha_0 \sin(\omega t)$
Amplitude	0.01 m	Amplitude	1°
Frequency	20 Hz	Frequency	20 Hz
Time Step	$1 \cdot 10^{-3} s$	Time Step	$1 \cdot 10^{-3} s$

Table 5.5: Motion and transient test parameters for Fluent simulation.

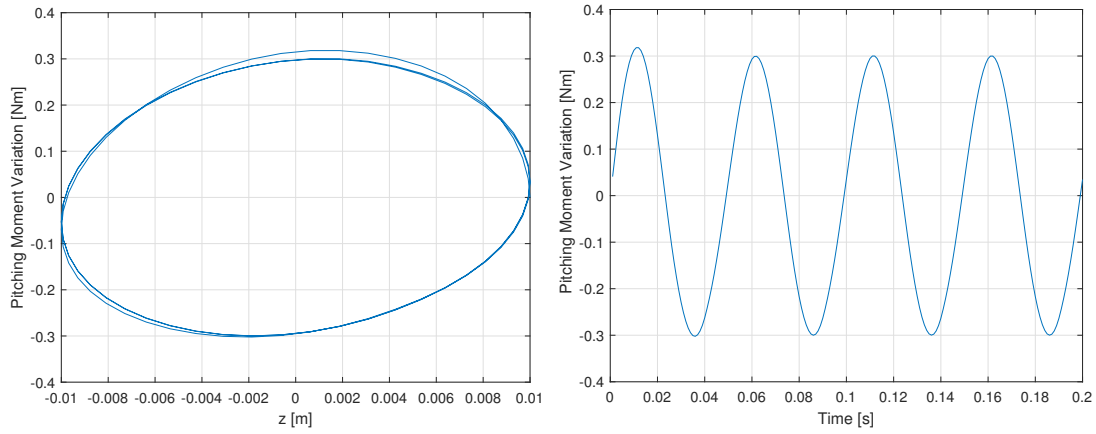


Figure 5.8: Hayabusa: plunging oscillation, AoA=0°.

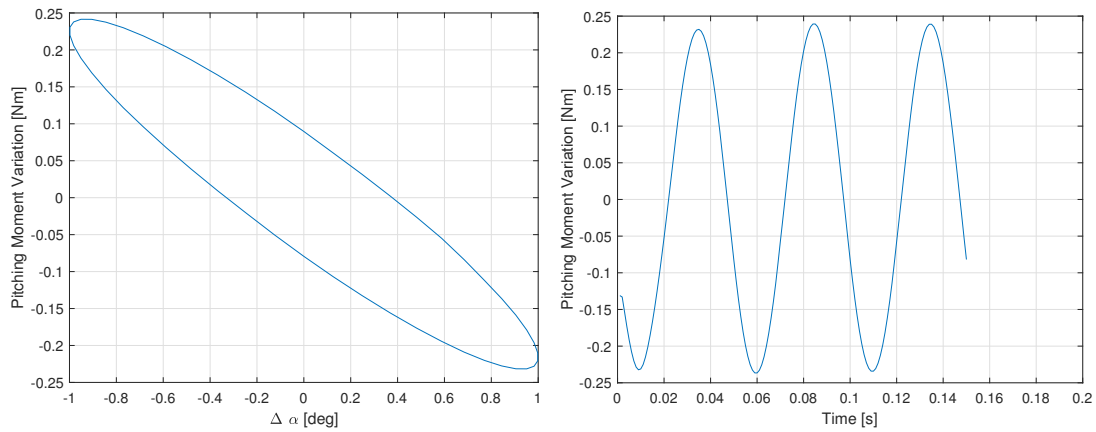


Figure 5.9: Hayabusa: pitching oscillation, AoA=0°.

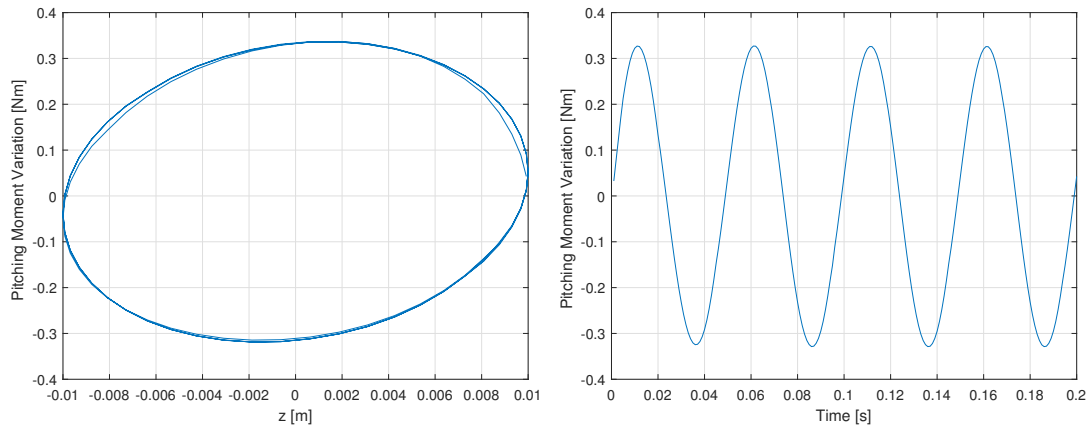


Figure 5.10: Hayabusa: plunging oscillation,  $AoA=10^\circ$ .

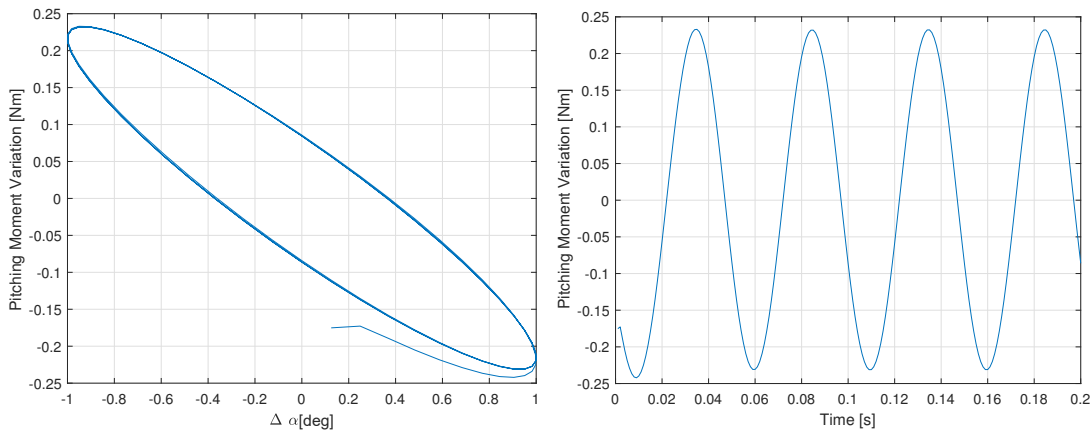


Figure 5.11: Hayabusa: pitching oscillation,  $AoA=10^\circ$ .

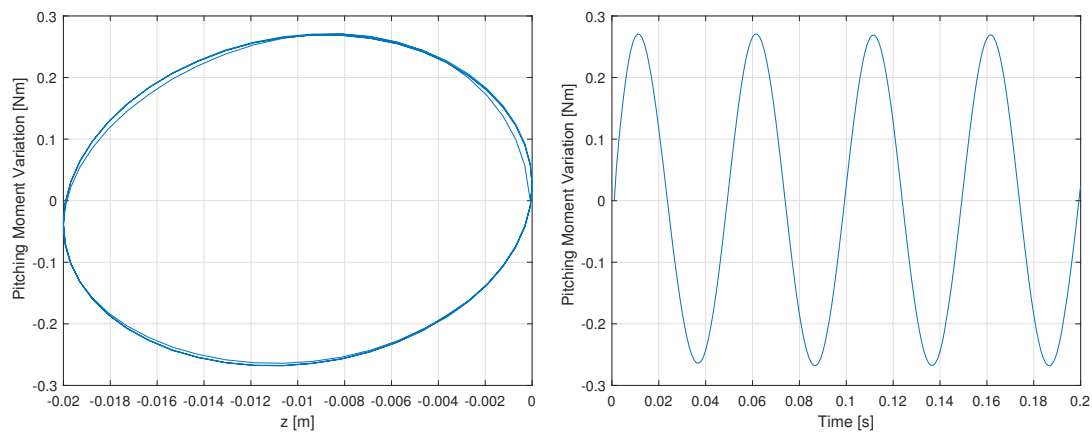


Figure 5.12: Hayabusa: plunging oscillation,  $AoA=20^\circ$ .

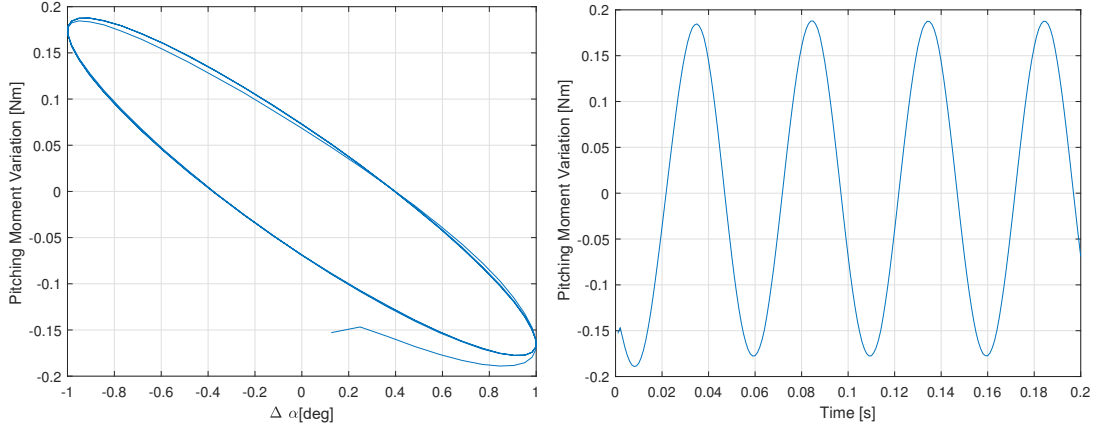


Figure 5.13: Hayabusa: pitching oscillation, AoA=20°.

### 5.3.3 Post-Processing

Utilizing a Matlab script  $C_{m\alpha}$ ,  $C_{m\dot{\alpha}}$ ,  $C_{mq}$ ,  $C_{m\dot{q}}$  have been extracted. The integrals 3.19 3.20 3.32 3.33 have been calculated considering only the variation of  $C_m$  around mean value and the last period of time history. Then using the equation 3.7 it has been tried to reproduce the  $C_m$  variation and verify that a very small mistake is made neglecting the terms of higher order of the Taylor’s series.

AoA	CFD Data				Data Sheet	
	$\alpha$	$C_{m\alpha}$	$C_{m\dot{\alpha}}$	$C_{mq}$	$C_{m\dot{q}}$	
0		-0.2629	-0.0849	-0.0187	-0.6887	0.14
10		-0.2882	-0.0890	-0.0151	-0.8310	-0.29
20		-0.2378	-0.0588	-0.0277	-0.7117	-1.61

Table 5.6: Hayabusa: aerodynamic derivatives from Fluent simulations.

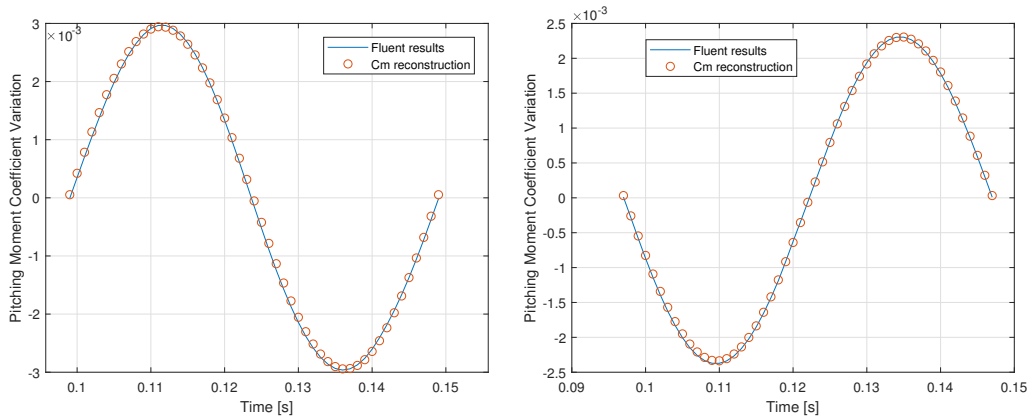


Figure 5.14: Hayabusa: oscillation reconstruction, AoA=0°.

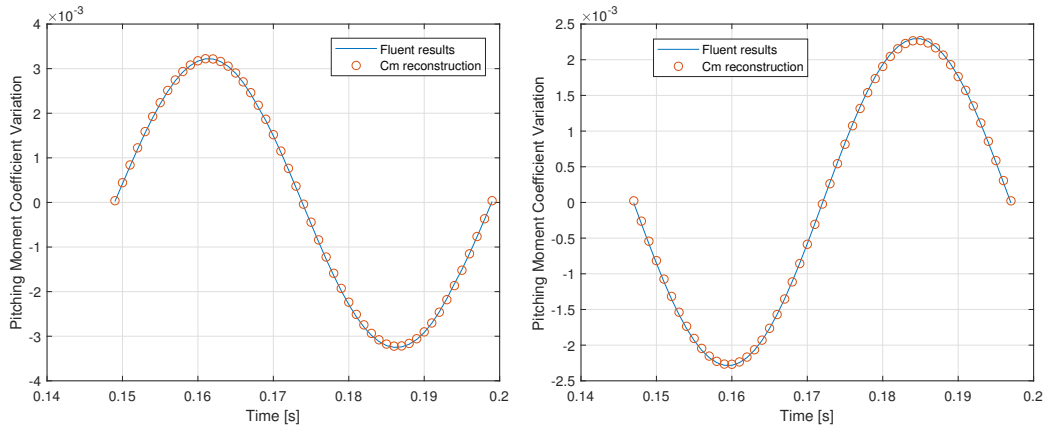


Figure 5.15: Hayabusa: oscillation reconstruction, AoA=10°.

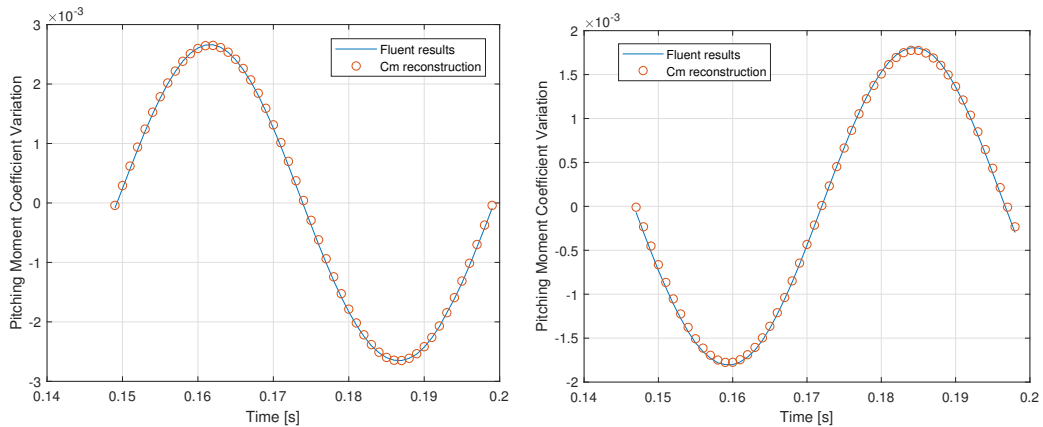


Figure 5.16: Hayabusa: oscillation reconstruction, AoA=20°.

From the figures 5.14, 5.14, 5.14 and table 5.6 two conclusions can be deduced. Matlab algorithm for the derivatives extraction has worked as shown by the perfect overlap of the  $C_m$  curve from CFD and  $C_m$  reconstruction. Despite this, the derivatives do not match absolutely, so the error lies in the numerical results.

## 5.4 CFD++ Simulations

In the following section, the results for the CFD++ simulations are presented for the angle of attack of 10°. The approach is the same as that used for Fluent simulation: a steady state solution has been used as starting point for transient simulation.

### 5.4.1 Steady State Tests

In the table 5.7 are reported the aerodynamic coefficients calculated from CFD++ solutions and the corresponding values shown on database.

AoA [deg]	CFD Data			Database		
	$C_A$	$C_N$	$C_m$	$C_A$	$C_N$	$C_m$
10	0.737	0.066	-0.022	0.88	0.06	-0.022

Table 5.7: CFD++ steady state test results.

Also in this case on the axial force a substantial error is made, while the gap is reduced in the case of the normal force and the axial moment.

### 5.4.2 Transient Tests

For plunging and pitching motion tests, amplitude and frequency parameters are reported in table 5.5. In CFD++ a sinusoidal motion is imposed for both motion.

Plunging motion		Pitching motion	
Motion	$z = z_o \sin(\omega t)$	Motion	$\alpha = \alpha_0 \sin(\omega t)$
Amplitude	0.01 m	Amplitude	1°
Frequency	20 Hz	Frequency	20 Hz
Time Step	$1 \cdot 10^{-3}$ s	Time Step	$1 \cdot 10^{-3}$ s

Table 5.8: Motion and transient test parameters.

In figures 5.17, 5.18, the variation of pitching moment in function of  $z/\Delta\alpha$  and time is displayed.

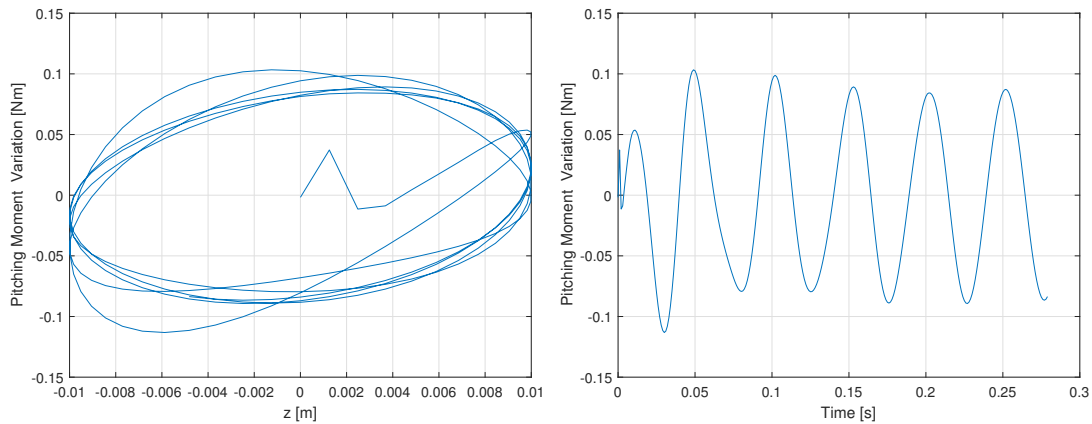


Figure 5.17: Hayabusa: plunging oscillation, AoA=0°.

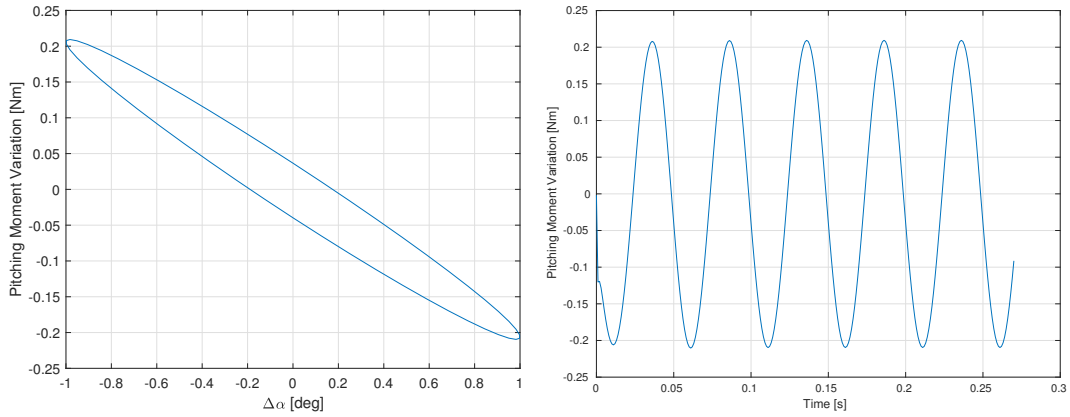


Figure 5.18: Hayabusa: pitching oscillation,  $AoA=10^\circ$ .

Also in this case, the oscillations of  $C_m$  have about a transitory period before to reach the limit cycle.

### 5.4.3 Post-Processing

In table 5.9 the aerodynamic derivatives extracted from the CFD++ results are presented.

AoA	Prove CFD				Data Sheet
$\alpha$	$C_{m\alpha}$	$C_{m\dot{\alpha}}$	$C_{mq}$	$C_{m\dot{q}}$	$C_{mq}$
10	0.0762	-0.0391	-0.0079	0.9602	-0.29

Table 5.9: Hayabusa: aerodynamic derivatives from CFD++ simulations.

The two figures 5.19 show the  $C_m$  reconstruction using the equation 3.7 and the calculated derivatives.

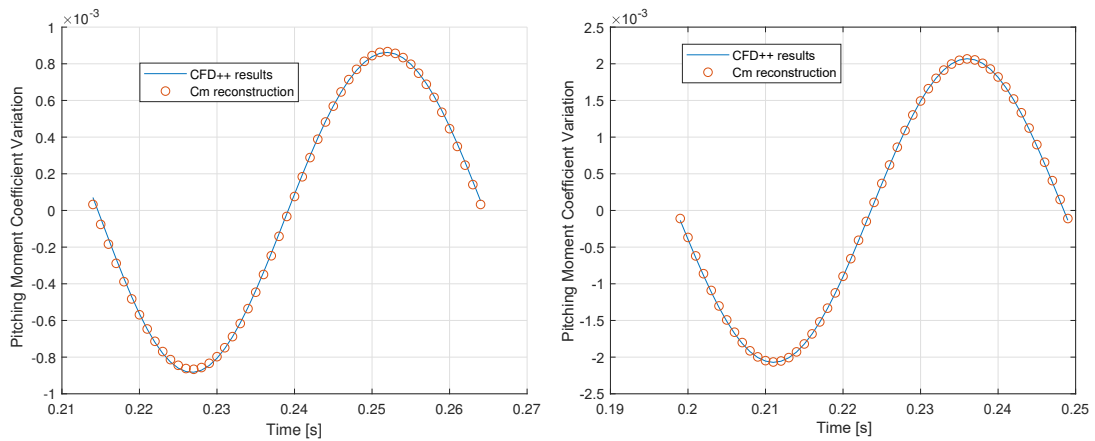


Figure 5.19: Hayabusa: oscillation reconstruction,  $AoA=10^\circ$ .

Once again the script proves to be able to extract the aerodynamic derivatives from the time history of the  $C_m$  but this one is subject to accuracy errors that go to influence the parameters calculated.

## 5.5 Comparison

For alpha equal to  $10^\circ$ , it is possible to compare the results obtained by two solvers. Since plunging motion in Fluent is a co-sinusoidal law while in CFD++ is a sinusoidal one, Fluent results have been translate over time of  $\pi/2$  to allow a direct comparison (figure 5.20). Regarding plunging motion a substantial difference can be seen between the amplitudes of the two curves. The amplitude of the  $C_m$  oscillations obtained from CFD++ is smaller than about two thirds of the curve obtained with Fluent. It is also noted that in CFD++ the time required for the solution to repeat itself is slightly greater. Conversely in the case of pitching oscillation the two solutions show only small differences in amplitude and period, but while the solution from CFD++ has reached the limit cycle in the first iterations, in Fluent it has required about a period of settling.

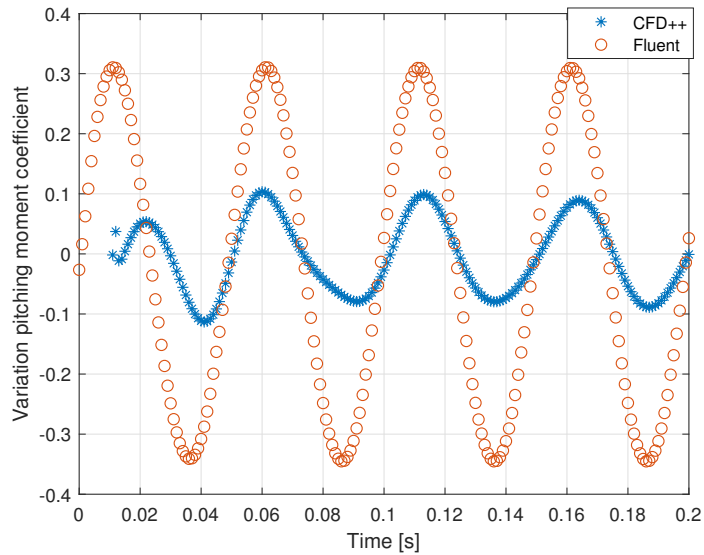


Figure 5.20: Hayabusa: CFD++ results compared with Fluent results for plunging oscillation,  $AoA=10^\circ$ .

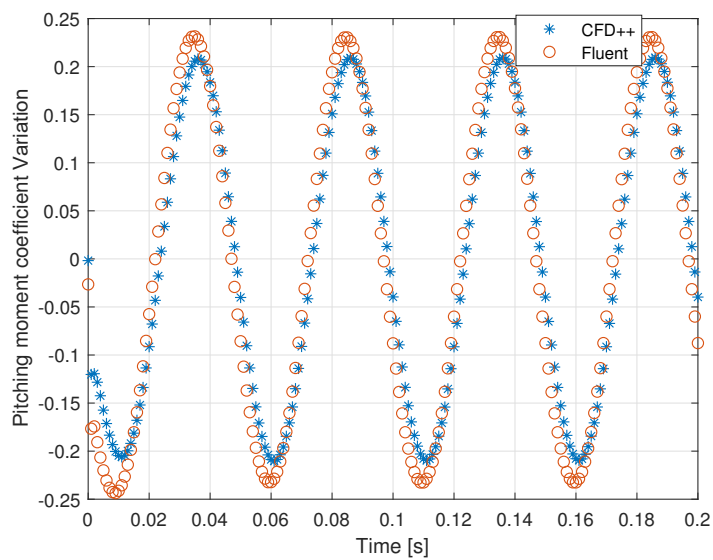


Figure 5.21: Hayabusa: CFD++ results compared with Fluent results for pitching oscillation,  $AoA=10^\circ$ .

Analysing the values of each derivative extracted from the two solvers, they show a convergence in signs but they are quite far from the value of the damping derivative present in the literature.

	$\alpha$ [deg]	$C_{m\alpha}$	$C_{m\dot{\alpha}}$	$C_{mq}$	$C_{m\dot{q}}$	Damping sum
CFD++	10	-0.0762	-0.0391	-0.0079	-0.9602	-0.0483
Fluent	10	-0.2871	-0.0923	-0.0118	-0.8253	-0.1042
Data Sheet	10	-	-	-0.2900	-	-

Table 5.10: Hayabusa: aerodynamic derivatives from CFD++ simulations.

## Chapter 6

# Space Rider: Numerical Simulations

In the previous chapter a rather simple case has been analysed to define the processes for extracting the aerodynamic derivatives from a CFD calculation. In this chapter, the study of a slightly complex geometry, Space Rider aero-shape, has been examined, comparing again the two solvers and collecting results that provide the definitive proof of the analysis method accuracy.

In the first part is shown mesh generation and numerical set-up that sets the foundation for the numerical code. Finally, the two solvers results are shown and a comparative is reported at the end. Since this chapter is an extension of the previous one, some aspects previously analysed are taken for granted while more attention is paid to analysis peculiar aspects.

### 6.1 Pre-processing

As explained, two codes require two different set-ups and so two different mesh for the specific type of analyse.

#### 6.1.1 Basic Assumption

Even here, before introducing procedures and final mesh it is useful to introduce some general assumptions which have guided this study:

- centre of gravity is fixed and the aerodynamic moment is calculated respect to it;
- the only pitching moment is measured, considering side-slip angle equals to  $0^\circ$ ;
- analyses have been conducted at the angles of attach of  $[65^\circ]$ .
- the free-stream conditions have been set in such a way as to be consistent with the tests carried out in the database: static pressure  $15570 Pa$  , temperature  $216.65 K$  and Mach number of 0.6.

- taking advantage of body XZ-symmetry plane only a half volume is taking account;
- flow regime is subsonic and fully turbulent;
- there is not heat-exchange between fluid and body wall;
- a Reynolds- number  $Re = 3.12 \cdot 10^6$  has been considered.

### 6.1.2 Mesh Generation

Fluent requires two meshes, one fixed and one mobile. The last one includes the body walls and in the calculation initialization it is superimposed on the first one using Chimera technique. About the mesh for CFD++, only the largest domain is taken into consideration and the resulting grid is quite similar to that prepared for Fluent (maximum dimensions, cell dimensions, etc...).

For Fluent the two fluid domains consist of two hemispheres of 300 *m* and 25 *m* in diameter. On the smaller one a subtract operation with Space Rider CAD model has been executed in order to defining the shuttle walls. The external diameter has been chosen in such a way to allow wake evolution and avoid the reflection of pressure waves. Meanwhile the inner diameter has been selected in order to prevent that large gradients fall into overlapping zone.

The origin axis is placed in correspondence of shuttle centre of gravity and the moments are calculated with respect to it.

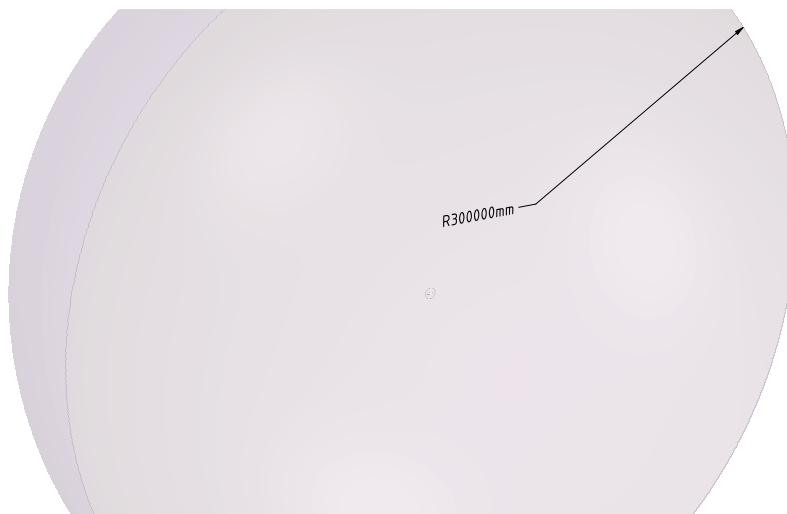


Figure 6.1: Size and shape of the fixed domain.

The generated mesh is composed by two element types: prisms and tetrahedrons. The first are used to compose prism layers generation, a discrete volume located around the body. This shape allow to capture boundary layer in efficient and accurate way. Following the same procedure executed for Hayabusa, the first cell height is  $5 \cdot 10^{-6} m$  so that capturing the viscous sublayer. The total height is limited to  $1.2 \cdot 10^{-2} m$  due to some quality constrains such as excessive aspect ratio of the last cell, skewness and mutual penetration in some

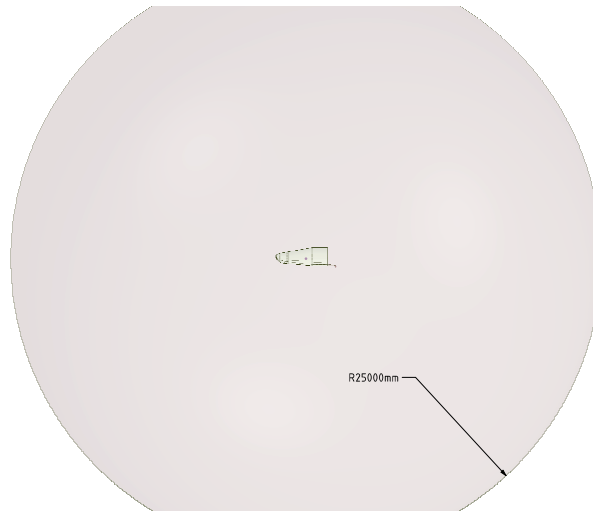


Figure 6.2: Size and shape of the moving domain.

points of the geometry. As it is possible to see in figure 6.3 the first height is set correctly since the  $y^+$  it does not exceed the value of one on the wall.

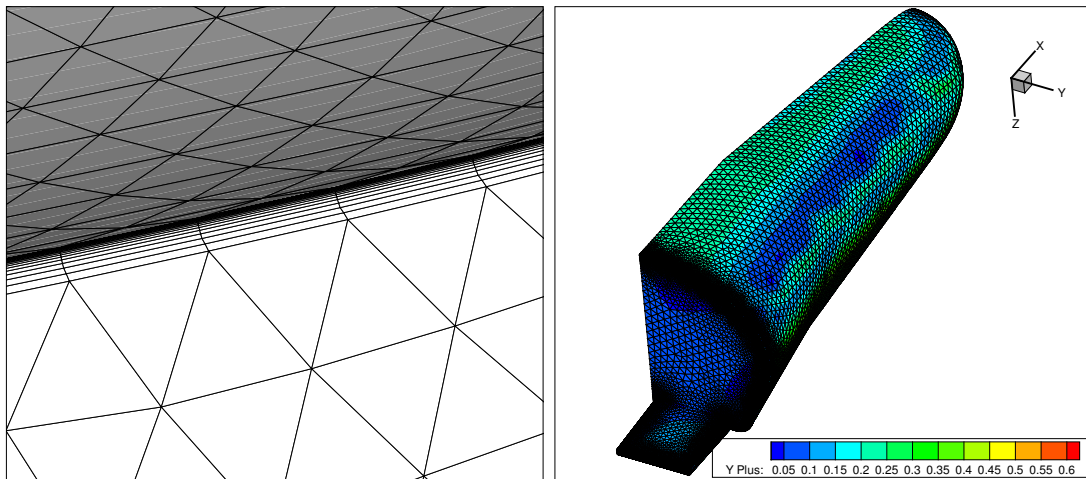


Figure 6.3: On the left an image of the prism layers at the wall and on the right the values of  $y^+$  on the capsule.

The tetrahedrons cells fill the discrete volume from prism elements up to external boundary. The minimum surface elements size is  $5\text{ mm}$  in correspondence of the joints and  $40\text{ mm}$  on the rest of the body in order to follow perfectly the surfaces curvature. About volume elements minimum size is  $110\text{ mm}$  in order to improve accuracy where the flow is strongly turbulent while the maximum size is limited to  $32\text{ m}$  in order to have not a too low resolution in zones away from body. Figure 6.4 shows the whole grid, where it is possible to notice the use of volume cells control to optimize the cells density around the body and in wake region.

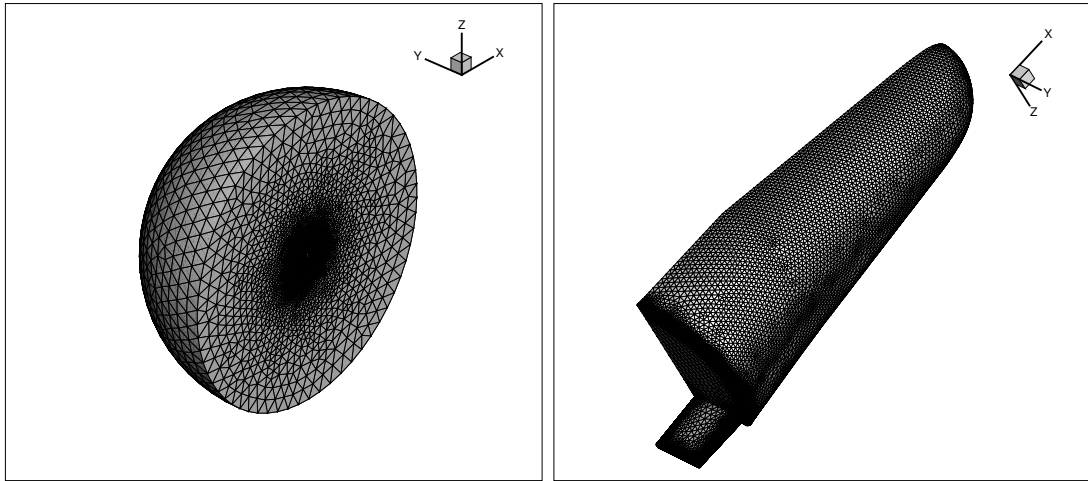


Figure 6.4: View of the domain and Space Rider mesh.

In figures 6.5 it is shown the zone in which the overset has been adopted. In the first figure notice the cells that come into play for the transmission of primitives through the two grids. In the second figure a contour scene of mass imbalance is represented. Due to Chimera technique a high value of residual is concentrated close up the overset boundary.

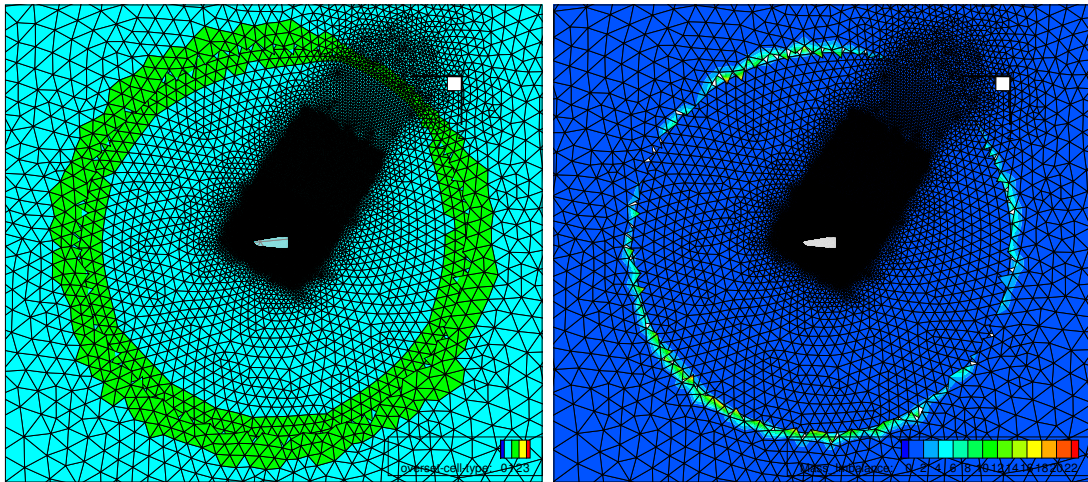


Figure 6.5: On the left the cells affected by the overset are highlighted, while on the right we can see the region where the continuity residual is high.

## 6.2 Numerical Set-Up

Three boundary conditions are utilized: symmetry, wall and pressure far-field conditions. As shown in figure 6.6 the walls of the domain have been divided and grouped into sub-groups on which the same boundary condition type is imposed. For each of sub-groups, a boundary

condition type and characteristic parameters are reported in table 6.1.

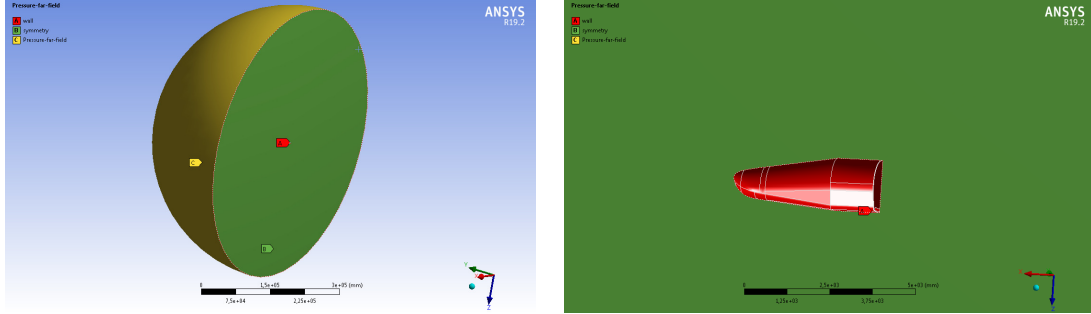


Figure 6.6: Boundary groups.

<b>Capsule’s Wall {Wall}</b>	
Wall Motion	Stationary Wall
Thermal Conditions	adiabatic
<b>Pressure far-field {Pressure far-field}</b>	
Static Pressure (Pa)	15570
Free-Stream Mach number	0.6
x-component of flow Direction	-0.4226
y-component of flow Direction	0
z-component of flow Direction	-0.9063
Temperature (K)	216.5
Turbulent Intensity (%)	5
Turbulent Viscosity Ratio	10
<b>Symmetry Plane {Symmetry}</b>	
-	-

Table 6.1: Parameters set for each boundary.

Finally in the table 6.2 models and numerical schemes used in the CFD simulations are reported.

### 6.3 Fluent Simulations

The results of the Fluent simulations for Space Rider are presented in this section. Only the  $65^\circ$  angle of attack has been tested and the all procedures seen for Hayabusa have been reproduced. Time-step of  $6 \cdot 10^{-3} s$  has been chosen; it has been obtained by the empirical formulation,  $\text{time-step} = T/256$ , that recent similar studies report (Marongiu et al. 2013). A second time-step of  $1 \cdot 10^{-3} s$  has been chosen in order to improve the solution accuracy.

<b>Numerical Set-Up For Fluent</b>	
Gas model	Compressible Ideal Gas
Viscous model	Sutherland Law
N-S equations	RANS
Turbulence Model	$k - \omega$ SST
Resolution Algorithm	Coupled Pressure-Based
Numerical Scheme	Upwind
- Pressure	2 <sup>nd</sup> Order
- Density	2 <sup>nd</sup> Order
- Momentum	2 <sup>nd</sup> Order
- Turbulent $k$	1 <sup>st</sup> Order
- Turbulent $\omega$	1 <sup>st</sup> Order
- Energy	2 <sup>nd</sup> Order
Transient Configuration	
Numerical Scheme	1 <sup>st</sup> Implicit Order
Inner iteration	50/100
<b>Numerical Set-Up for CFD++</b>	
Gas model	Compressible Ideal Gas
Viscous model	Sutherland Law
N-S equations	RANS
Turbulence Model	$k - \omega$ SST
Resolution Algorithm	Coupled Pressure-Based
Numerical Scheme	Upwind
- Pressure	2 <sup>nd</sup> Order
- Density	2 <sup>nd</sup> Order
- Momentum	2 <sup>nd</sup> Order
- Turbulent $k$	2 <sup>nd</sup> Order
- Turbulent $\omega$	2 <sup>nd</sup> Order
- Energy	2 <sup>nd</sup> Order
Transient Configuration	
Numerical Scheme	2 <sup>nd</sup> Implicit Order
Inner iteration	50

Table 6.2: Models and algorithms set.

### 6.3.1 Steady State Test

First a steady state solution has been performed. In table 6.3 it is possible to find the aerodynamic coefficients found from CFD data and aerodynamic coefficient from database. The nominal values are in bold while the other represent the uncertainty range.

Comparing the values, the normal force and pitching moment coefficient are perfectly within the uncertainty range, while for the axial force, the values is out of limits.

CFD Data				Database			
AoA [deg]	$C_A$	$C_N$	$C_m$	AoA [deg]	$C_A$	$C_N$	$C_m$
65	-0.0900	0.9414	0.0172	$3\sigma$	0.0115	1.1305	0.0409
				<b>65</b>	<b>0.0260</b>	<b>1.0255</b>	<b>0.0199</b>
				$3\sigma$	-0.0635	0.9205	-0.0011

Table 6.3: Fluent steady state tests results.

### 6.3.2 Transient Tests with Time-step of 6e-3 s

The first transient test has been performed with a time step of  $6 \cdot 10^{-3}$  s. Both the rotational and translational oscillations have a sinusoidal shape and table 6.4 contains all simulation parameters.

Plunging motion		Pitching motion	
Motion	$z = z_0 \sin(\omega t)$	Motion	$\Delta\alpha = \alpha_0 \sin(\omega t)$
Amplitude	1.63 m	Amplitude	$2^\circ$
Frequency	0.605 Hz	Frequency	0.605 Hz
Time Step	$6 \cdot 10^{-3}$ s	Time Step	$6 \cdot 10^{-3}$ s

Table 6.4: Motion and transient test parameters.

In figures 6.7 and 6.8 it is shown the variation of pitching moment in function of  $z/\Delta\alpha$  and time for the two motions. Both curves are very irregular and the solver shows difficulties especially near maximum amplitude of the sinusoid.

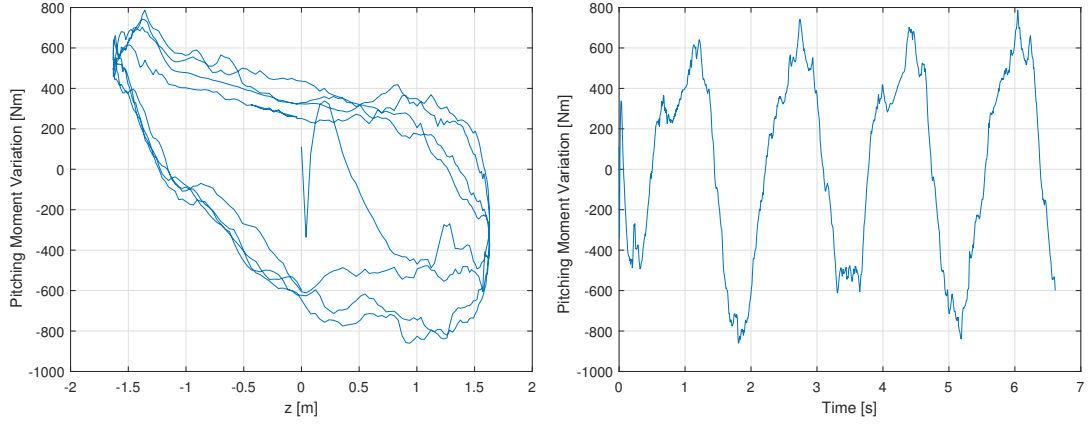


Figure 6.7: Space Rider: plunging oscillation,  $AoA=65^\circ$ .

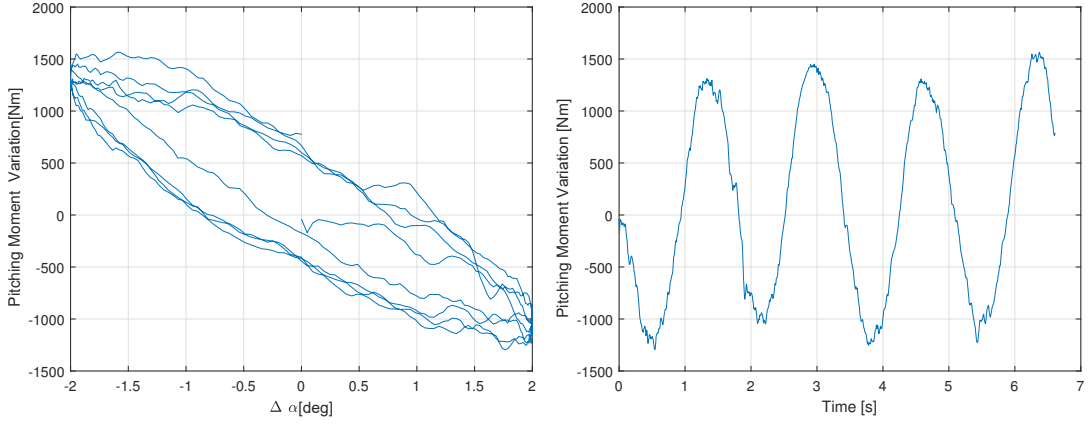


Figure 6.8: Space Rider: pitching oscillation,  $AoA=65^\circ$ .

### 6.3.3 Transient Tests with Time-step of $1e-3$ s

In the second transient test a time step of  $1 \cdot 10^{-3}$  s has been used in order to obtain a smoother solution. The other parameters remain unchanged.

Plunging motion		Pitching motion	
Motion	$z = z_0 \sin(\omega t)$	Motion	$\Delta\alpha = \alpha_0 \sin(\omega t)$
Amplitude	$1.63 \text{ m}$	Amplitude	$2^\circ$
Frequency	$0.605 \text{ Hz}$	Frequency	$0.605 \text{ Hz}$
Time Step	$1 \cdot 10^{-3} \text{ s}$	Time Step	$1 \cdot 10^{-3} \text{ s}$

Table 6.5: Motion and transient test parameters.

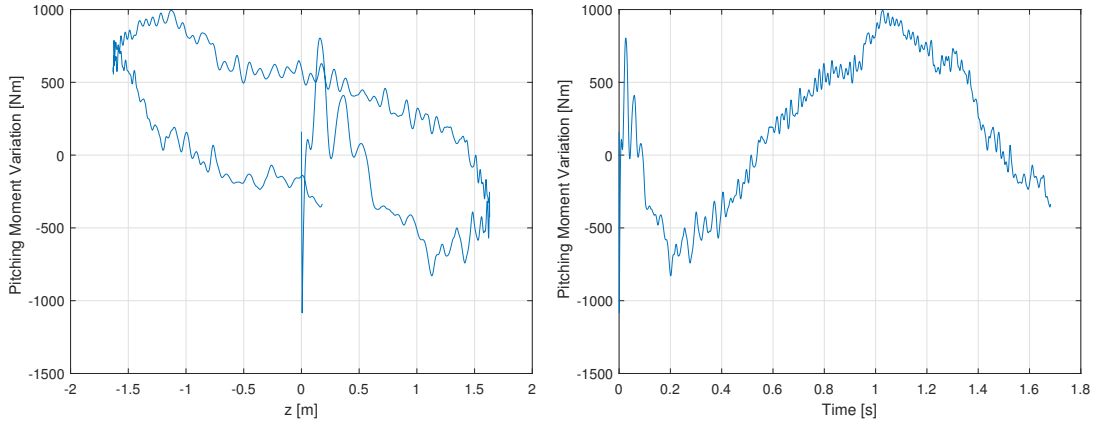


Figure 6.9: Space Rider: plunging oscillation, AoA=65°.

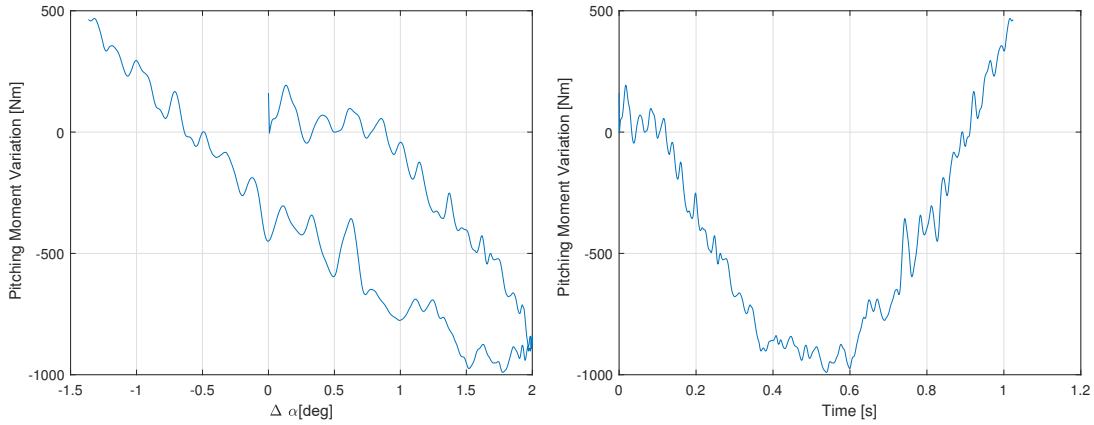


Figure 6.10: Space Rider: pitching oscillation, AoA=65°.

As it is possible to see in figures 6.9 and 6.10 the solution becomes very irregular so it was decided to stop prematurely the running.

### 6.3.4 Post-Processing

Since the second test was not completed an attempt to extract the derivatives is performed only on the first case.

AoA	Prove CFD				Data Sheet			
$\alpha$ [deg]	$C_{m\alpha}$	$C_{m\dot{\alpha}}$	$C_{mq}$	$C_{m\dot{q}}$	$C_{m\alpha}$	$C_{m\dot{\alpha}}$	$C_{mq}$	$C_{m\dot{q}}$
65	-0.1149	1.1414	0.0836	16.3993	-0.211	1.336	-0.06	-

Table 6.6: Space Rider: aerodynamic derivatives from Fluent simulations.

As expected by looking at the  $c_m$  trends in the two tests, the values of the derivatives show a substantial difference with respect to the values from the database.

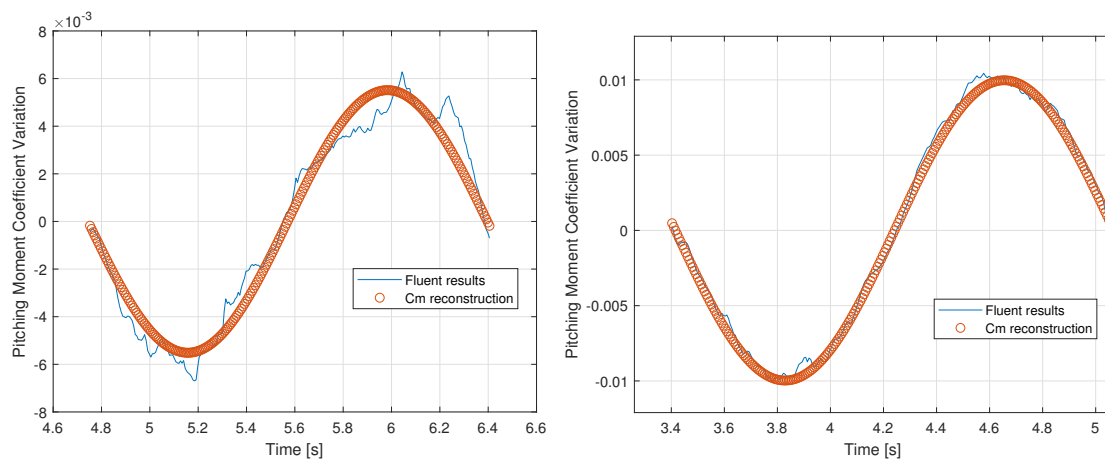


Figure 6.11: Space Rider: oscillation reconstruction,  $AoA=65^\circ$ .

## 6.4 CFD++ Simulations

The last campaign of test has been performed using CFD++ solver. The results for the Space Rider simulations are presented for an angle of attack of  $65^\circ$ .

### 6.4.1 Steady State Test

In the table 6.7 it is reported the aerodynamic coefficients calculated from CFD++ solutions and the corresponding values shown on database. The nominal values are in bold while the other represent the uncertainty range.

Again comparing axial force coefficient it is quite out of the uncertainty range, while pitching moment and normal force coefficient fall into range.

AoA [deg]	$C_A$	CFD Data	
		$C_N$	$C_m$
65	-0.1168	1.0621	0.0423
AoA [deg]	$C_A$	Database	
		$C_N$	$C_m$
$3\sigma$	0.0115	1.1305	0.0409
<b>65</b>	<b>0.0260</b>	<b>1.0255</b>	<b>0.0199</b>
$3\sigma$	-0.0635	0.9205	-0.0011

Table 6.7: CFD++ steady state test results.

## 6.4.2 Transient Tests

In matter of transient testing campaign, only a time step of  $6 \cdot 10^{-3} s$  has been performed. Plunging and pitching oscillation parameters are reported in table 6.8.

Plunging motion		Pitching motion	
Motion	$z = z_o \sin(\omega t)$	Motion	$\Delta\alpha = \alpha_o \sin(\omega t)$
Amplitude	1.63 m	Amplitude	$2^\circ$
Frequency	0.605 Hz	Frequency	0.605 Hz
Time Step	$6 \cdot 10^{-3} s$	Time Step	$6 \cdot 10^{-3} s$

Table 6.8: Motion and transient test parameters.

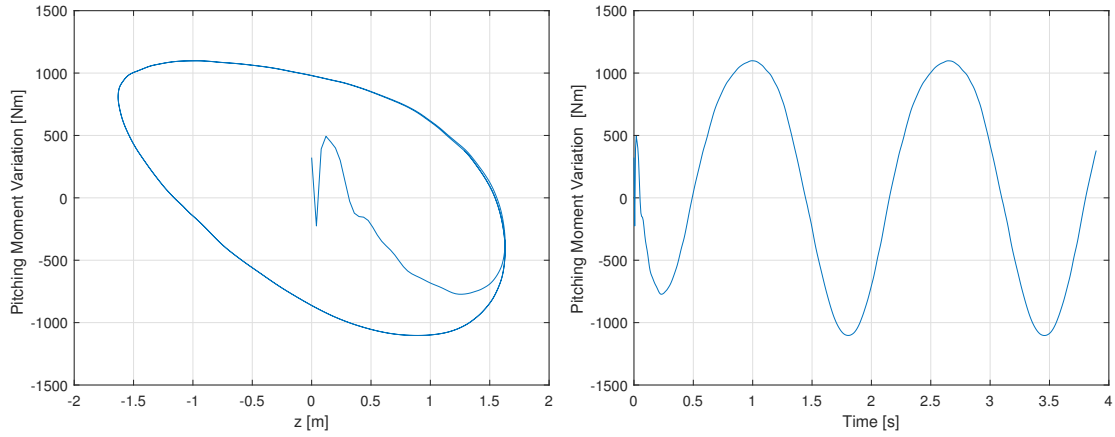


Figure 6.12: Space Rider: plunging oscillation, AoA=65°.

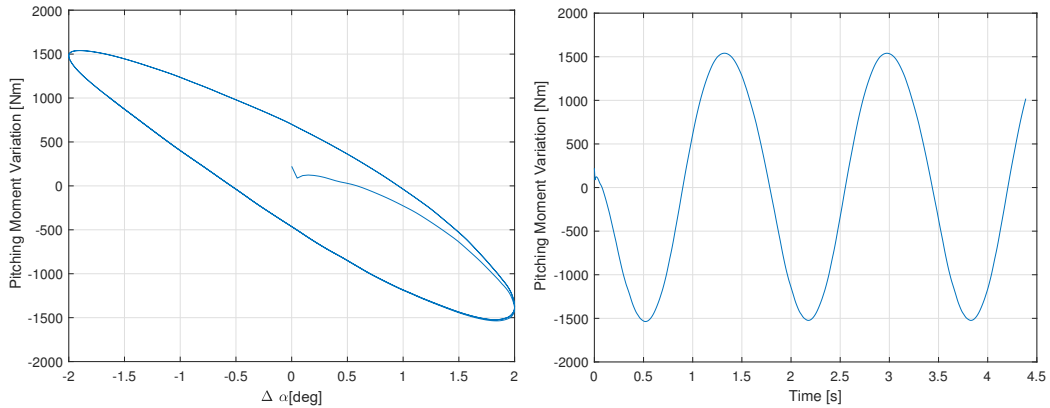


Figure 6.13: Space Rider: pitching oscillation, AoA=65°.

In figures 6.12, 6.13, the variation of pitching moment in function of  $z/\Delta\alpha$  and time is displayed. The curves are very smooth and the limit cycle is reached correctly.

### 6.4.3 Post-Processing

Utilizing the Matlab script  $C_{m\alpha}$ ,  $C_{m\dot{\alpha}}$ ,  $C_{mq}$ ,  $C_{m\dot{q}}$  have been extracted and reported in 6.9. Results very close to those from databases have been achieved, but it is necessary to notice a displacement that occurs between the curve obtained from CFD and the reconstructed one for plunging motion. It is practically zero in the peaks of the curve while it increases in the two descending and ascending branches. This error may be caused by the fact that the  $C_m$  curve is not perfectly sinusoidal and reconstructed one is not able to completely overlap it because the higher order terms of Taylor's series have been truncated.

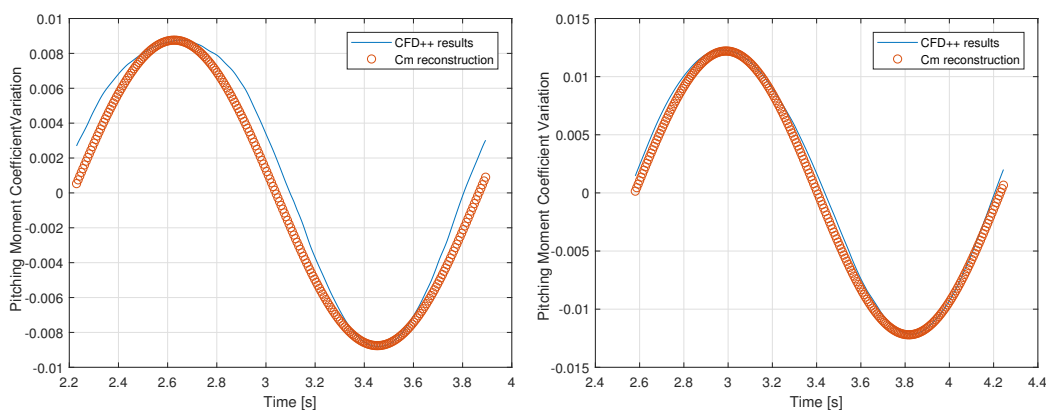


Figure 6.14: Space Rider: oscillation reconstruction, AoA=65°.

AoA	Prove CFD				Data Sheet			
$\alpha$ [deg]	$C_{m\alpha}$	$C_{m\dot{\alpha}}$	$C_{mq}$	$C_{m\dot{q}}$	$C_{m\alpha}$	$C_{m\dot{\alpha}}$	$C_{mq}$	$C_{m\dot{q}}$
65	-0.212	1.4077	-0.0617	12.7352	-0.211	1.336	-0.06	-

Table 6.9: Space Rider: aerodynamic derivatives from CFD++ simulations.

## 6.5 Comparison

Now it is possible to compare all the results obtained by the two solvers concerning Space Rider with each other and with those on database.

Concerning Fluent results with time step of 6 s, in pitching oscillation seem to overlap enough with the results present in the database. However it is very unstable, in fact in the lower peaks the code fails to provide a very clean and accurate solution, and in the last period, there is a slight overshoot in correspondence with the upper peak. In plunging case results worsen and both in positive and negative peaks the solution loses accuracy.

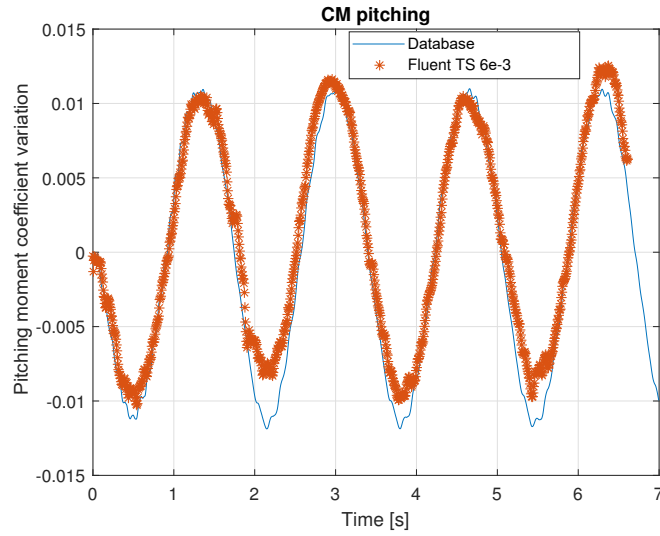


Figure 6.15: Space Rider: Fluent results with time step= $6 \cdot 10^{-3} s$  compared with database results.

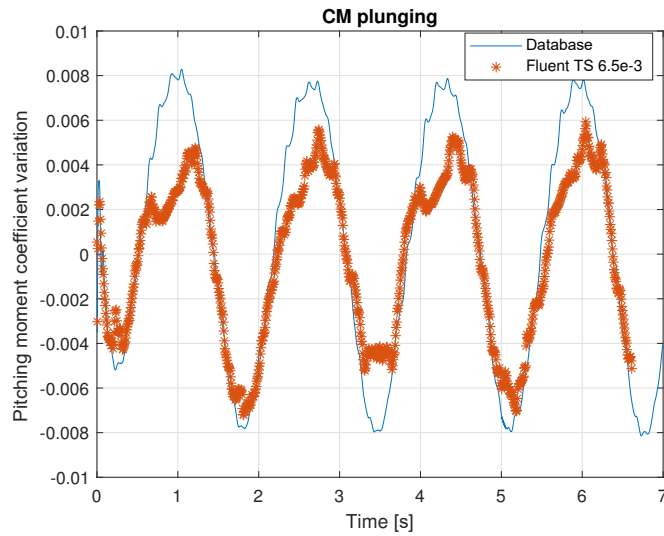


Figure 6.16: Space Rider: Fluent results with time step= $6 \cdot 10^{-3} s$  compared with database results.

Shifting to the shorter time step, curves become much more irregular as is shown in figures 6.18 a-b. Although the average trend of the solution seems to be slightly better in positive and negative peaks in plunging motion compared to solution calculated at time step of  $6 \cdot 10^{-3} s$ ; it shows a deterioration in the case of pitching with the presence of an overshoot in the positive peak 6.18 c-d.

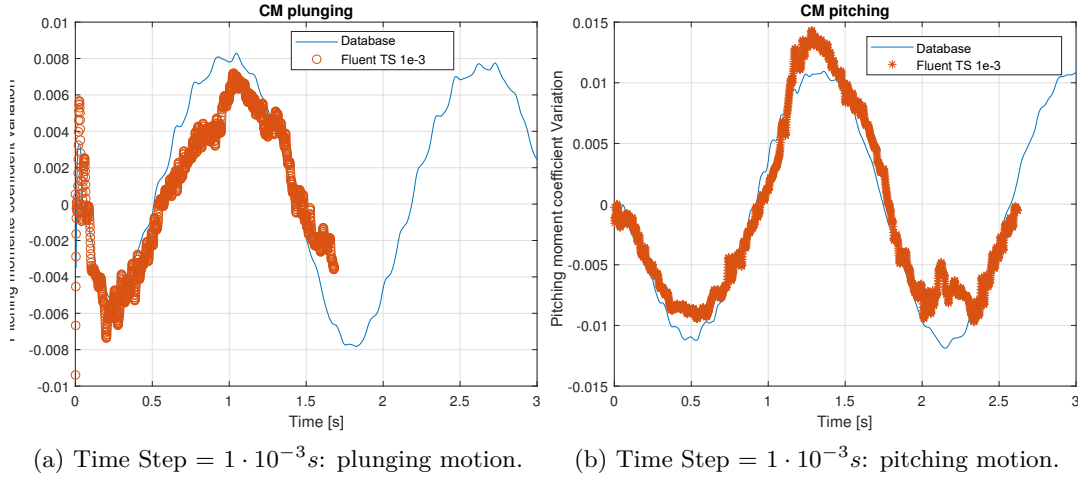


Figure 6.17: Space Rider: Fluent results with time step= $1 \cdot 10^{-3} s$  compared with database curve.

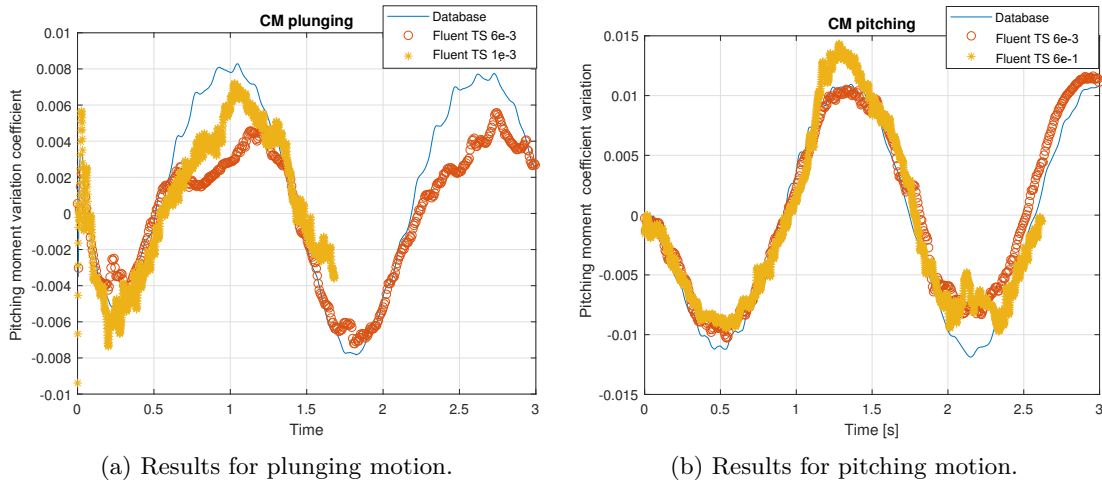


Figure 6.18: Space Rider: Fluent results with time step= $1 \cdot 10^{-3} s$  and time step= $6 \cdot 10^{-3} s$ .

As demonstrated by the results of aerodynamic derivatives very close to the values from the database, the  $C_m$ , calculated by CFD++ solution, overlaps the database curve below and it is very smooth and clean (figure 6.19 and figure 6.20). In addition it seems to go even better than the original solution in correspondence with the peaks, addressing what seems to be the natural evolution.

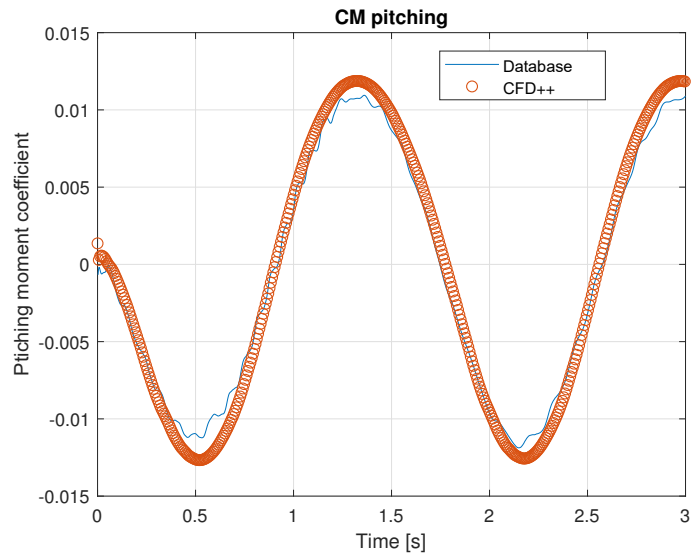


Figure 6.19: Space Rider: CFD++ results with Time Step= $6 \cdot 10^{-3}s$  compared with database.

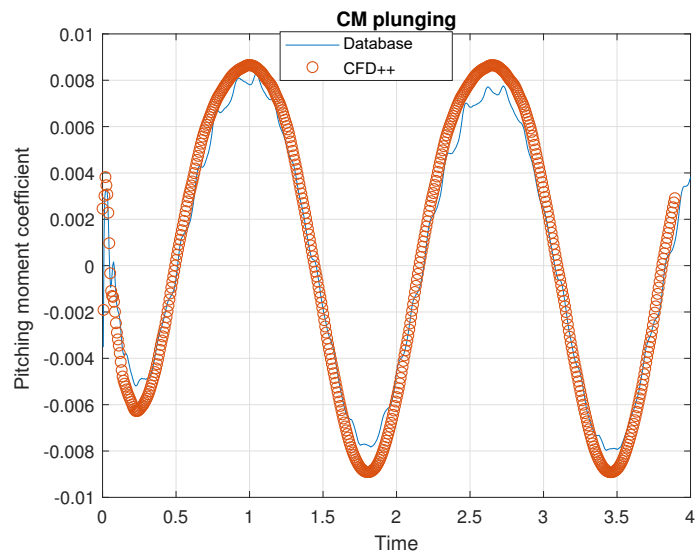


Figure 6.20: Space Rider: CFD++ results with Time Step= $6 \cdot 10^{-3}s$  compared with database.



# Chapter 7

## Conclusions

The purpose of this work was to validate a numerical procedure for the calculation of aerodynamic derivatives using two types of re-entry vehicles: the Hayabusa capsule and the lifting-body Space Rider. The study was conducted implementing the forced oscillation method in two commercial computational fluid dynamics codes, Ansys Fluent and Metacomp CFD++.

Results achieved show that the target has been fully accomplished. In particular, results relating to the Space Rider study, attained using the CFD++ solver and shown in section 4.3, are fairly coincident with the values present in the aerodynamic database. The presence of a very small deviation is due to multiple factors, first of all the error induced by using a different calculation grid.

Concerning the error between the reconstructed curve and the original moment coefficient curve for plunging oscillation, (figure 6.19), it could be associated with the need of further running the simulation over time to reach a complete convergence; this is corroborated observing that none of the previous elaborations show a similar deviation.

Results obtained on Space Rider with Fluent solver are not very satisfactory. The momentum coefficient curves are really irregular and not accurate, especially in correspondence with the oscillation peaks. The identification of the cause will require further analysis; starting from the set-up differences between the solvers a possible cause could be identified in the use of a first order time discretization, or the use of the chimera technique. An investigation of the solution sensitivity to turbulence model could be also conducted.

Capsule simulations are not completely accurate. Although they provided some positive indications about the approach implemented, results are very far from the database values. It was not possible to identify where errors occurred due to the lack of a complete and accurate database for the flow regime used. Moreover, it is important to underline that in literature there are many different capsule geometries with the name of Hayabusa, which makes difficult to identify a correct reference documentation.

In conclusion, this work allowed to validate a numerical procedure able to calculate the aerodynamic derivatives of a vehicle during re-entry phase. At the same time it opens the way to future investigations, e.g. continuing the work on Space Rider using other angles of attack, studying how the solution could vary with respect to changes in amplitude and frequency of oscillation. Afterwards, a further step should be to analyse cases in transonic and supersonic flow regime.



# Appendix A

## CFD Figures

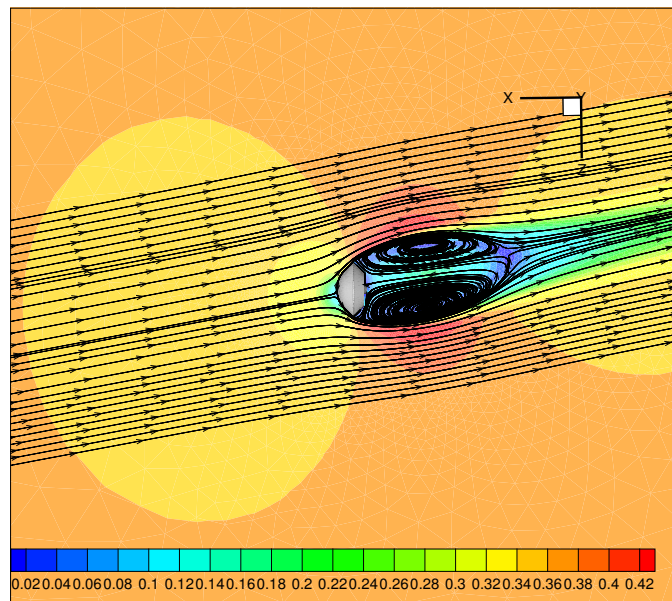


Figure A.1: Hayabusa: steady state result at  $10^\circ$  of AoA. Stream-lines and Mach number contour.

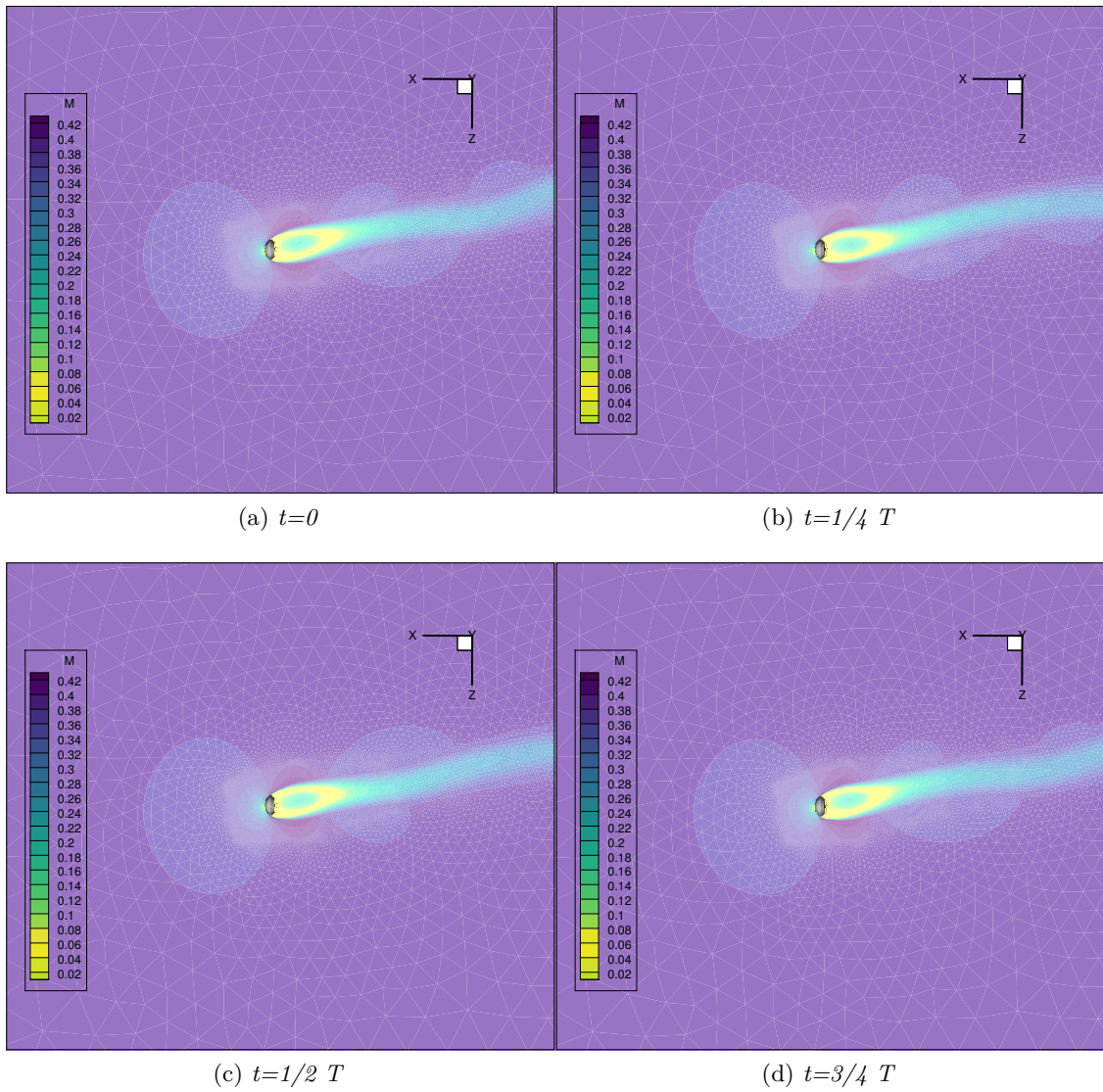


Figure A.2: Hayabusa: Mach number distribution in symmetry plane for 4 times-times over one period (Plunging motion)

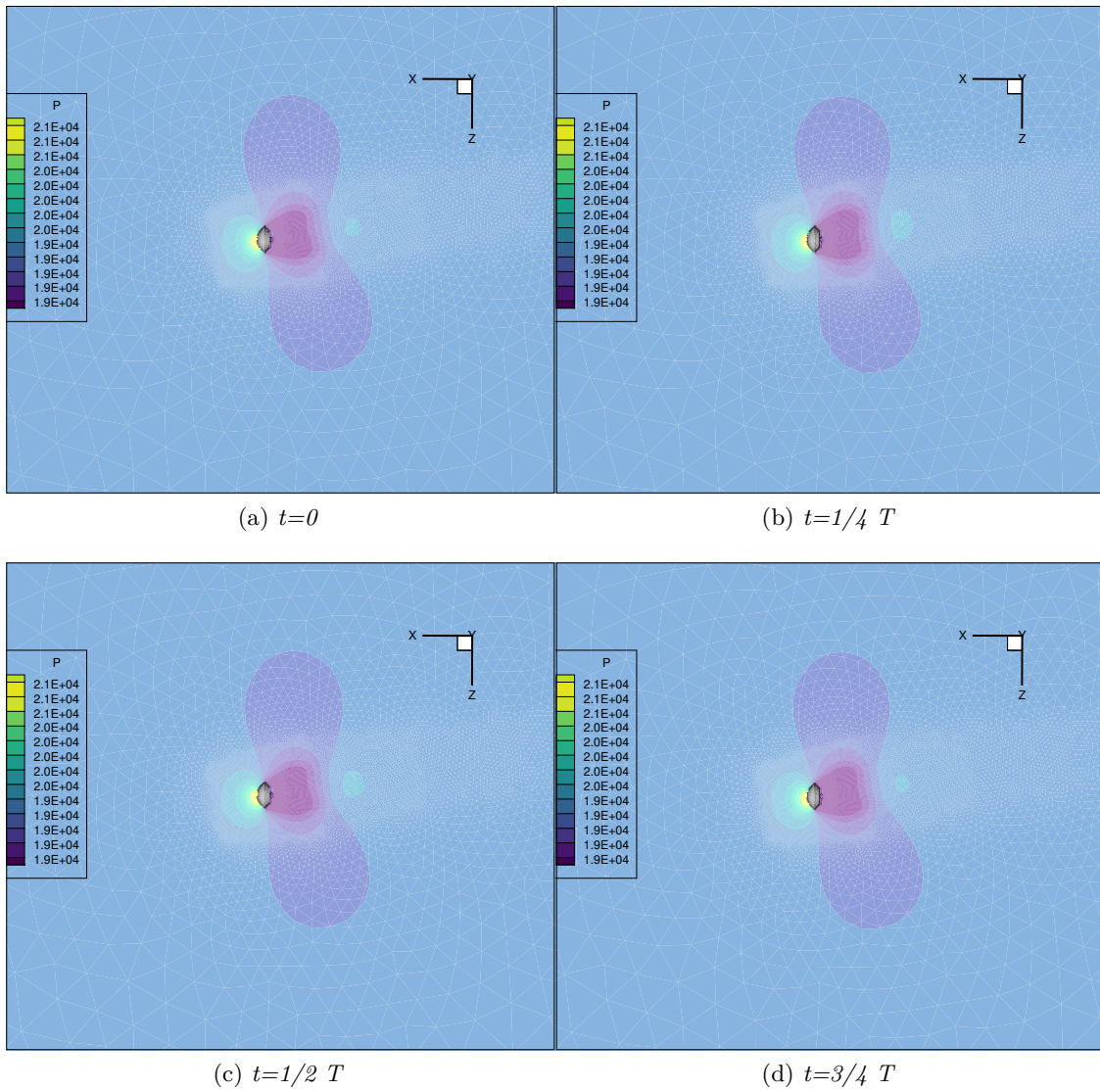


Figure A.3: Hayabusa: pressure distribution in symmetry plane for 4 times-times over one period (Plunging motion)

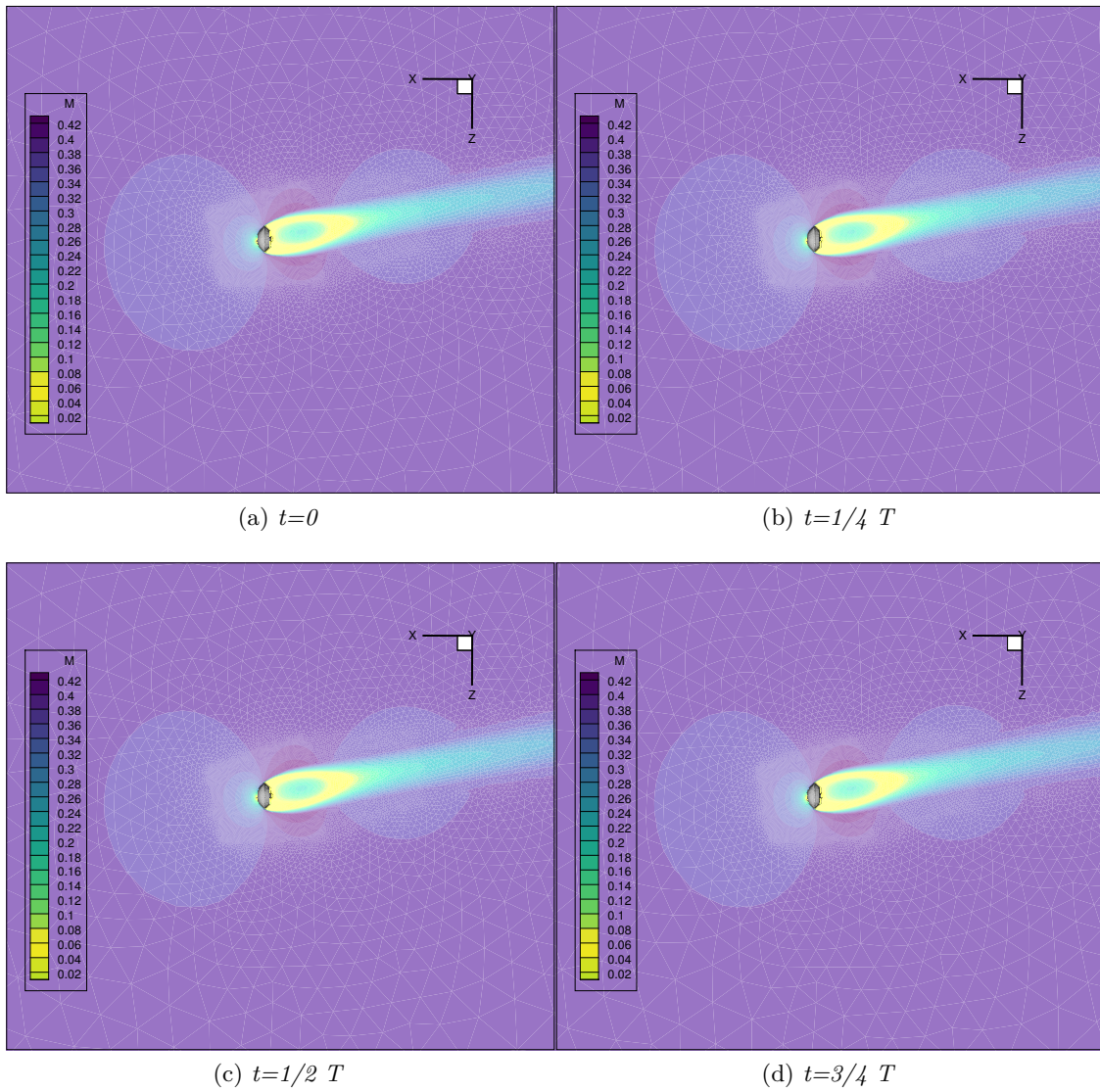


Figure A.4: Hayabusa: Mach number distribution in symmetry plane for 4 times-times over one period (Pitching motion).

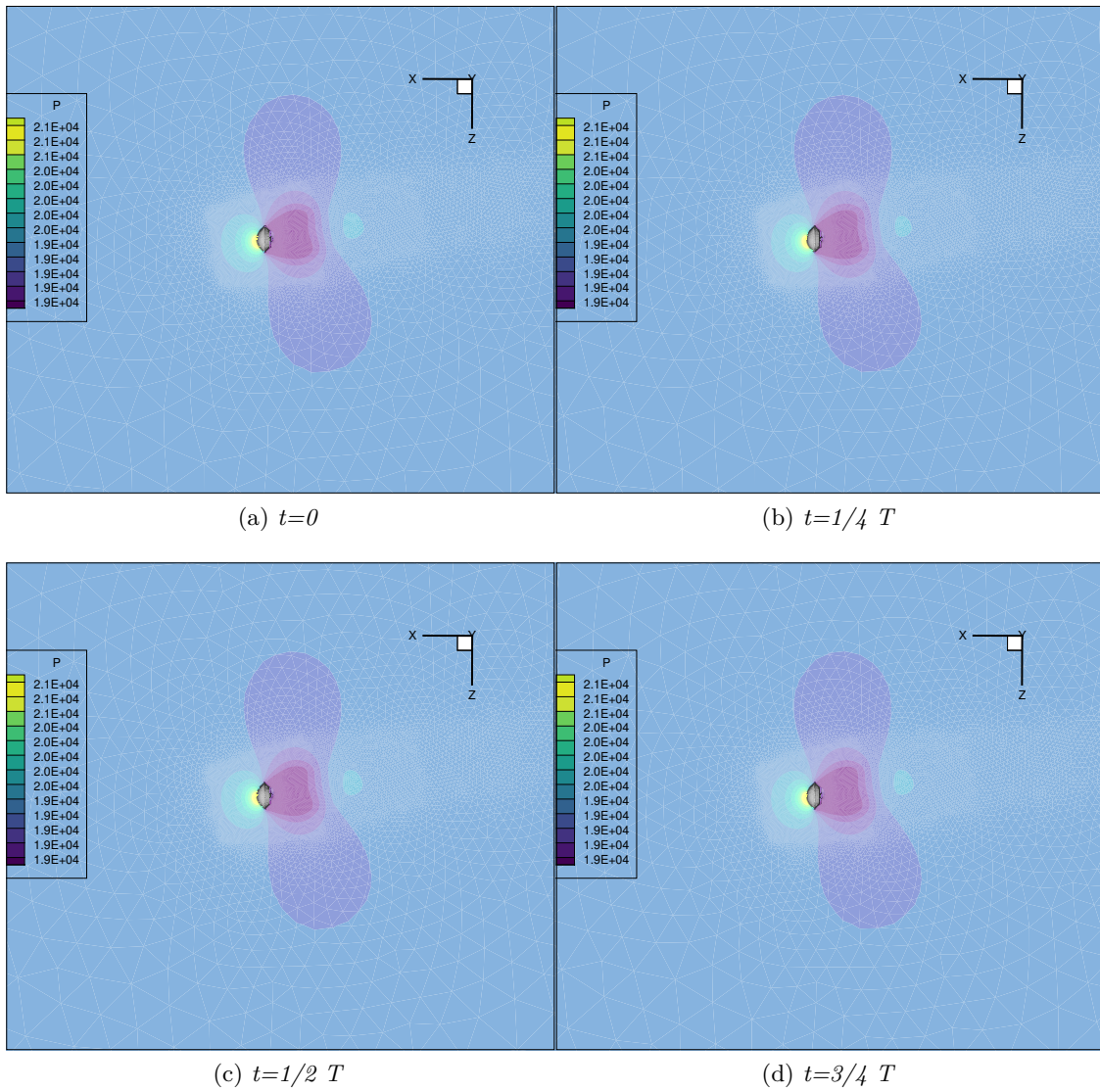


Figure A.5: Hayabusa: pressure distribution in symmetry plane for 4 times-times over one period (Pitching motion)

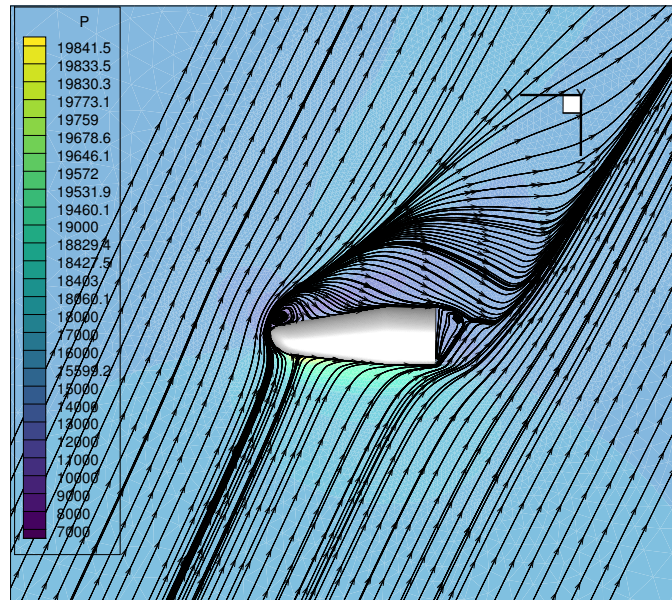


Figure A.6: Space Rider: steady state result at 10° of AoA. Stream-lines and Mach number contour.

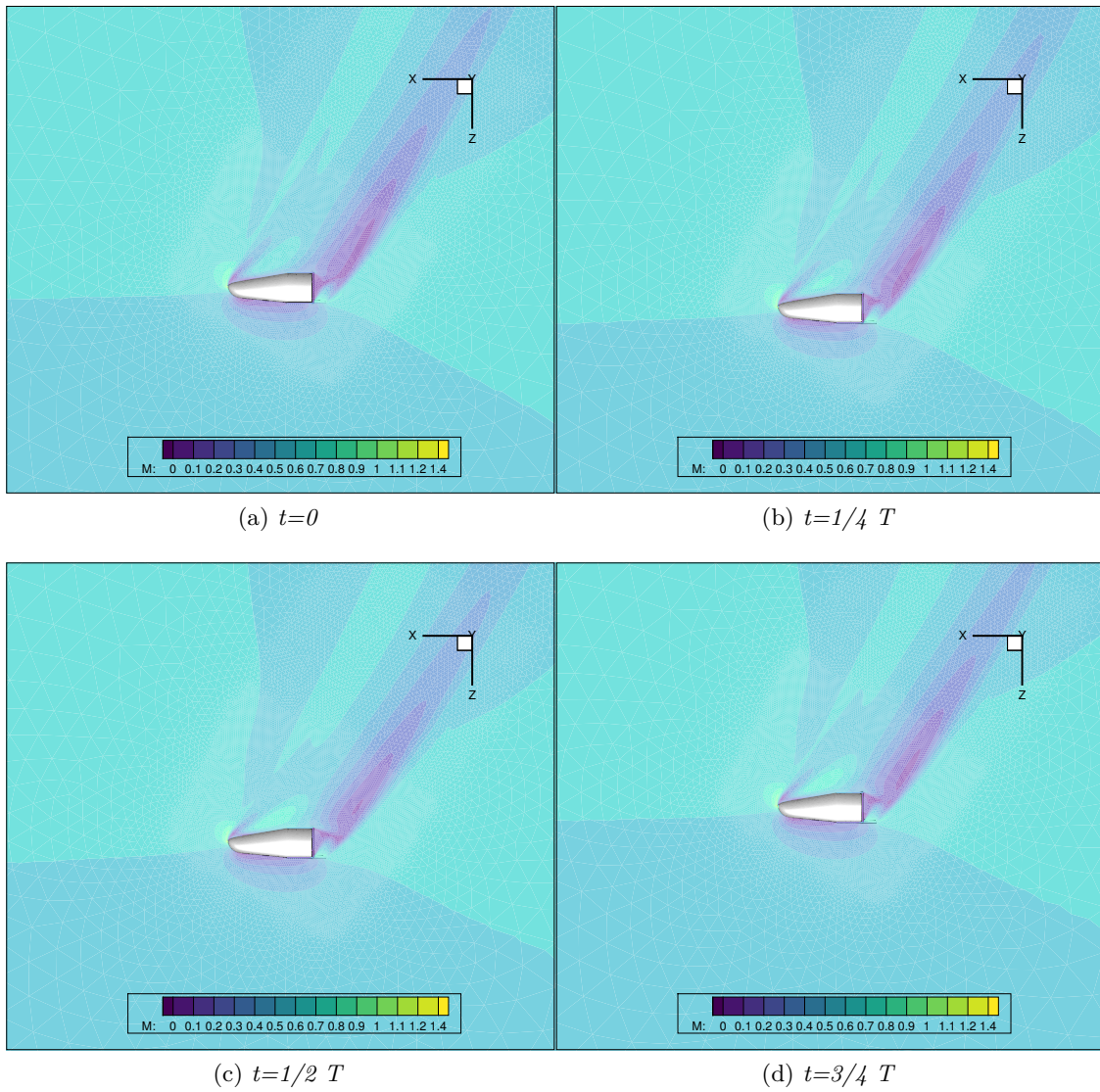


Figure A.7: Space Rider: Mach number distribution in symmetry plane for 4 times-times over one period (Plunging motion)

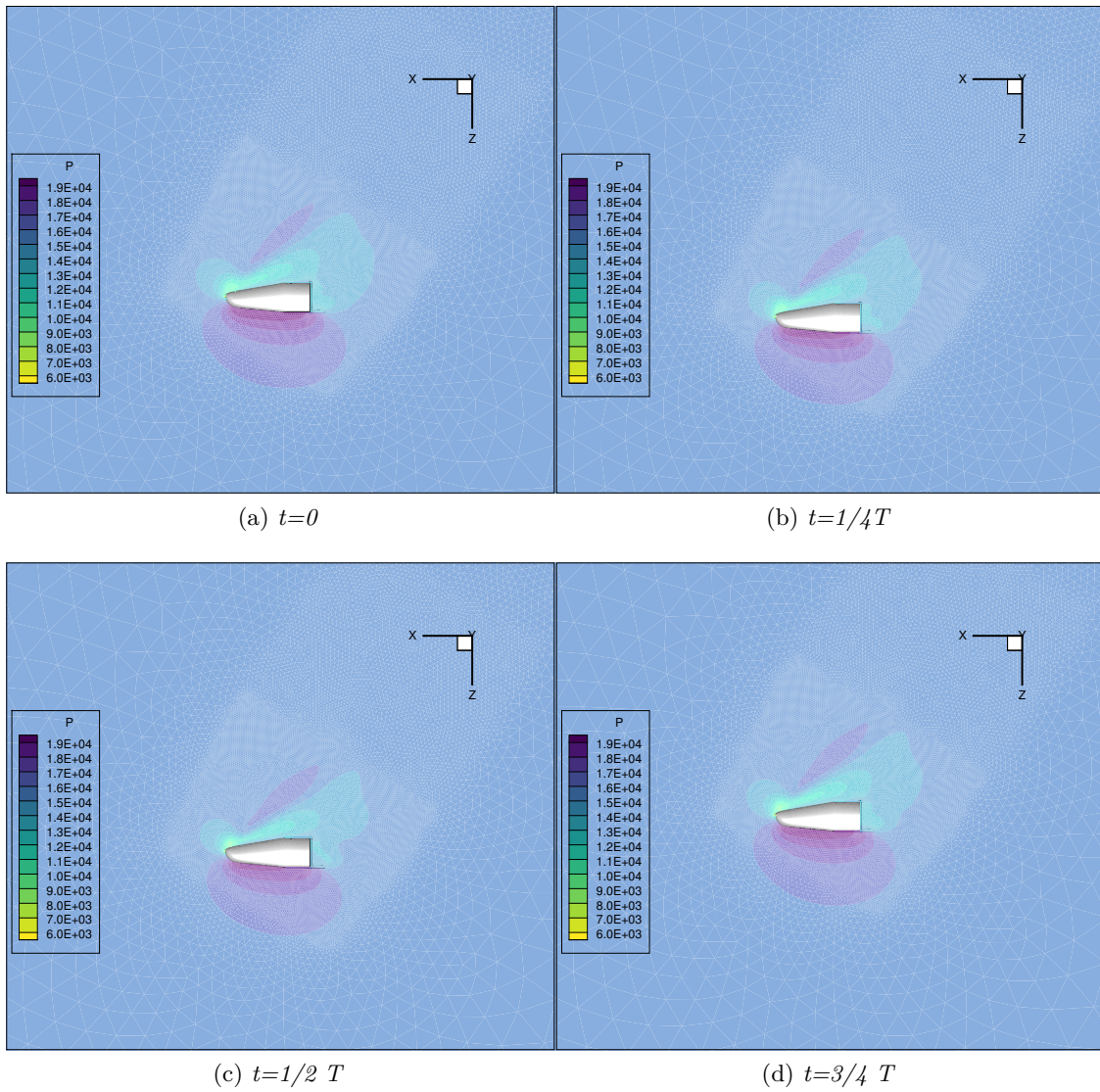


Figure A.8: Space Rider: pressure distribution in symmetry plane for 4 times-times over one period (Plunging motion)

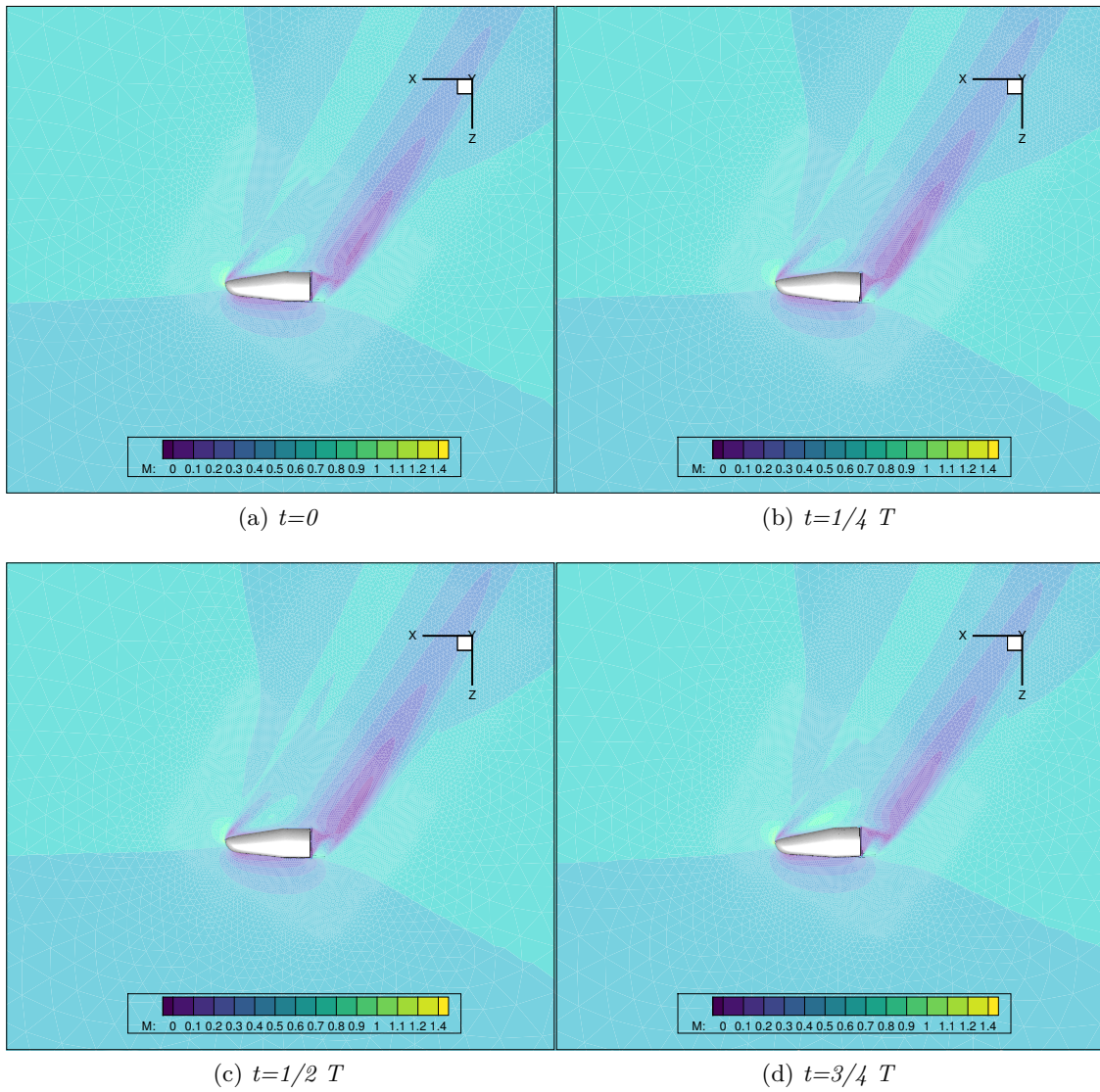


Figure A.9: Space Rider: Mach number distribution in symmetry plane for 4 times-times over one period (Pitching motion)

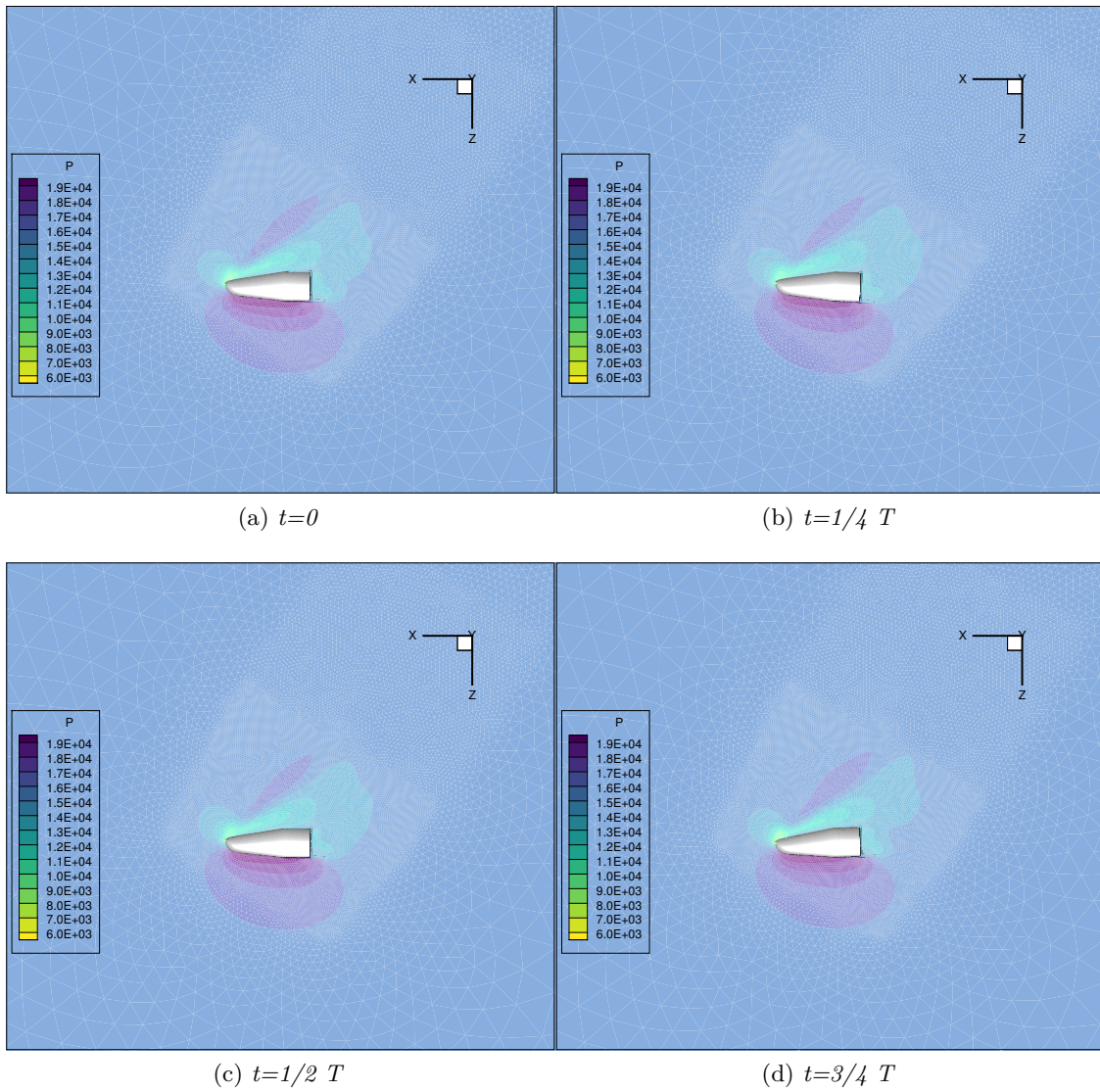


Figure A.10: Space Rider:pressure distribution in symmetry plane for 4 times-times over one period (Pitching motion)

# Bibliography

- Allen, Julian H (1957). *Motion of a ballistic missile angularly misaligned with the flight path upon entering the atmosphere and its effect upon aerodynamic heating, aerodynamic loads, and miss distance*.
- Ansys Fluent User and Theory's Guide* (2018).
- Asteroid Explorer Hayabusa* (2005). URL: [http://global.jaxa.jp/projects/sat/muses\\_c/files/presskit\\_hayabusa\\_e.pdf](http://global.jaxa.jp/projects/sat/muses_c/files/presskit_hayabusa_e.pdf).
- Baillion, M (1997). "Blunt bodies dynamic derivatives". In: *Special Course on "Capsule Aerodynamics"*, published in *AGARD Report 808*.
- Balossino, Alessandro et al. (2017). "Conceptual Design of the Descent Subsystem for the Safe Atmospheric Re-Entry Flight of Space Rider". In: *7<sup>T</sup> H EUROPEAN CONFERENCE FOR AERONAUTICS AND SPACE SCIENCES (EUCASS)*.
- Benek, JA et al. (1986). *Chimera. A grid-embedding technique*. Tech. rep. ARNOLD ENGINEERING DEVELOPMENT CENTER ARNOLD AFB TN.
- Bird, John D and David E Reese Jr (1958). *Stability of ballistic reentry bodies*.
- Bryan, George Hartley (1911). *Stability in aviation: an introduction to dynamical stability as applied to the motions of aeroplanes*. Macmillan and Co., limited.
- Da Ronch, A. et al. (2012). "Evaluation of dynamic derivatives using computational fluid dynamics". In: *AIAA journal* 50.2, pp. 470–484.
- Donea, Jean et al. (2004). "Arbitrary Lagrangian-Eulerian Methods". In: *Encyclopedia of computational mechanics*.
- Ericsson, Lars E and J Peter Reding (1971). "Re-Entry Camule Dynamics". In: *Journal of Spacecraft and Rockets* 8.6, pp. 579–586.
- Fletcher, HS (1959). "Damping in Pitch and Static Stability of a Group of Blunt Bodies from  $M=0.6$  to  $0.95$ ". In: *NASA TM X-194*.
- Franklyn, J. Kelecy (2008). "Coupling Momentum and Continuity Increases CFD Robustness". In: *ANSYS Advantage • Volume II, Issue 2*.
- Germano, M. (2010). "APPUNTI DI GASDINAMICA - CAPITOLO 3 - EQUAZIONI MEDIANE PER I FLUSSI TURBOLENTI".
- Hayabusa: A technology Demonstrator* (2005). URL: [http://global.jaxa.jp/projects/sat/muses\\_c/files/hayabusa\\_return.pdf](http://global.jaxa.jp/projects/sat/muses_c/files/hayabusa_return.pdf).
- Hiraki K., Inatani Y. et al. (1998). *Dynamic Stability of Muses-C Capsule*.
- Hirt, Cyril W, Anthony A Amsden, and JL Cook (1974). "An arbitrary Lagrangian-Eulerian computing method for all flow speeds". In: *Journal of computational physics* 14.3, pp. 227–253.

- Houzeaux, Guillaume et al. (2014). “A Chimera method for the incompressible Navier–Stokes equations”. In: *International Journal for Numerical Methods in Fluids* 75.3, pp. 155–183.
- Ishii, Nobuaki and Koju Hiraki (2003). “Attitude motion and aerodynamic characteristics of muses-c reentry capsule”. In: *The Institute of Space and Astronautical Science report. SP 17*, pp. 379–388.
- Kazemba, Cole et al. (2012). “Survey of blunt body dynamic stability in supersonic flow”. In: *AIAA Atmospheric Flight Mechanics Conference*, p. 4509.
- Korfanty, M and J Longo (2008). “CFD based dynamic analysis of atmospheric re-entry vehicles”. In: *2nd International ARA days, Arcachon*.
- Marini, M. et al. (2017). “Aeroshape Trade-Off and Aerodynamic Analysis of the Space-Rider Vehicle”. In: *7 TH EUROPEAN CONFERENCE FOR AERONAUTICS AND SPACE SCIENCES (EUCASS)*.
- Marongiu, C et al. (2013). “Dynamic Derivative Computation of a Sub-orbital Vehicle”. In: *31st AIAA Applied Aerodynamics Conference*, p. 3027.
- Orlik-Rückemann, KJ (1981). “Review of techniques for determination of dynamic stability parameters in wind tunnels”. In: *AGARD LS-114*.
- Ravera, Chiara and Domenic D’Ambrosio (2018). “Numerical Investigation on Aerodynamic Stability Derivatives of Earth Re-entry Caspules”. type. Politecnico di Torino.
- Schoenenberger, Mark, Prasad Kutty, et al. (2014). “The aerodynamics of axisymmetric blunt bodies flying at angle of attack”. In: *Aerospace Conference, 2014 IEEE*. IEEE, pp. 1–12.
- Schoenenberger, Mark and Eric M Queen (2008). “Limit cycle analysis applied to the oscillations of decelerating blunt-body entry vehicles”. In:
- Short, Barbara J and Simon C Sommer (1959). “Some measurements of the dynamic and static stability of two blunt-nosed, lowfineness-ratio bodies of revolution in free flight at  $M=4$ ”. In: *NASA TM X 20*.
- Space Rider Esa Multimedia* (2018). URL: [https://esamultimedia.esa.int/docs/space\\_transportation/Space\\_Rider\\_factsheet\\_HiRes\\_ok.pdf](https://esamultimedia.esa.int/docs/space_transportation/Space_Rider_factsheet_HiRes_ok.pdf).
- Space Rider homepage* (2017). URL: [https://www.esa.int/Our\\_Activities/Space\\_Transportation/Space\\_Rider](https://www.esa.int/Our_Activities/Space_Transportation/Space_Rider).
- Space Rider PRIDE* (2017). URL: <https://www.cira.it/en/space/accesso-allo-spazio-satelliti-ed-esplorazione/pride/Space%20Rider%20PRIDE>.
- Tang, HS, S Casey Jones, and Fotis Sotiropoulos (2003). “An overset-grid method for 3D unsteady incompressible flows”. In: *Journal of Computational Physics* 191.2, pp. 567–600.
- Teramoto, Susumu, Kouju Hiraki, and Kozo Fujii (2001). “Numerical analysis of dynamic stability of a reentry capsule at transonic speeds”. In: *AIAA journal* 39.4, pp. 646–653.
- Thompson, Joseph, Neal Frink, and Patrick Murphy (2010). “Guidelines for Computing Longitudinal Dynamic Stability Characteristics on Subsonic Transport”. In: *28th AIAA Applied Aerodynamics Conference*, p. 4819.
- Tobak, Murray and H Julian Allen (1958). *Dynamic stability of vehicles traversing ascending or descending paths through the atmosphere*.
- Viviani, Antonio and Giuseppe Pezzella (2015). *Aerodynamic and aerothermodynamic analysis of space mission vehicles*. Springer.